

DEVELOPMENT OF HIGH-RESOLUTION OPTICAL TOMOGRAPHY WITH  
LARGER-SIZE PROJECTION ACQUISITION

---

A Thesis presented to  
the Faculty of the Graduate School  
at the University of Missouri-Columbia

---

In Partial Fulfillment  
of the Requirements for the Degree

Master of Science

---

by

HSUAN-MING HUANG

Dr. Mark A. Haidekker, Thesis Supervisor

DECEMBER 2007

The undersigned, appointed by the Dean of the Graduate School,  
have examined the thesis entitled

DEVELOPMENT OF HIGH-RESOLUTION OPTICAL TOMOGRAPHY WITH  
LARGER-SIZE PROJECTION ACQUISITION

presented by Hsuan-Ming Huang,  
a candidate for the degree of Master of Science,  
and hereby certify that, in their opinion, it is worthy of acceptance.

---

Dr. Mark A. Haidekker, Department of Biological Engineering

---

Dr. John A. Viator, Department of Biological Engineering

---

Dr. Jimmy Lattimer, Department of Veterinary Medicine and Surgery

## ACKNOWLEDGEMENTS

I would like to thank my thesis advisor, Dr. Haidekker. I not only learned basic knowledge from him, but also studied research. He always devoted his time to guiding me and, is full of enthusiasm and patience. Furthermore, he built research devices and offered many tools to help my research. Without his contributions, it would not have been possible to finish my master degree. Doing research with him is very flexible and comfortable. I really enjoy working with him.

In addition, I like to express my thanks to my committee members, Dr. Yao, Dr. Lattimer, Dr. Viator and laboratory members, Jeff LaCroix, Ali Shuaib, Sasson Haviv and Matthew Nipper. They taught me how to operate many instruments and gave me very important suggestions and comments for my research. Through discussion with them, I obtained invaluable experiences and fundamental knowledge. Without their help, I would not have finished my research as smoothly. I want to thank all my friends and teachers who encouraged me and enriched my life: Dr. Ing-Tsung Hsiao, he was my undergraduate advisor. Without his direction and training, I would not have studied abroad.

## TABLE OF CONTENTS

ACKNOWLEDGEMENTS.....	ii
LIST OF ILLUSTRATIONS.....	v
LIST OF TABLES.....	xi
ABSTRACT.....	xii

### Chapter

1. BACKGROUND.....	1
1.1 Vascular Graft Tissue Engineering.....	1
1.2 Common Imaging Techniques for Tissue Engineered Blood Vessel.....	4
1.3 Special Imaging Techniques, Optical Tomography, for Blood Vessel.....	6
2. DESIGN OF THE NEW OPTICAL TRANSILLUMINATION TOMOGRAPHY SYSTEM.....	12
2.1 Basic Idea of the New OT System.....	12
2.2 Design of the Modified OT System.....	14
3. OPTICAL TRANSILLUMINATION TOMOGRAPHY THEORY.....	17
3.1 Principle of Optical Transillumination Tomography.....	17
3.2 Analytical Algorithms: Filtered Backprojection (FBP).....	20
3.3 Iterative Algorithms: Simultaneous Algebraic Reconstruction Techniques (SART).....	26
3.4 Construction of the System Matrix.....	32
4. EXPERIMENTS AND RESULTS.....	37
4.1 Basis for the First Phantom Study.....	37
4.2 Pre-processing before Image Reconstruction.....	40
4.3 Results of the First Phantom Study.....	46
4.4 Basis for the Second Phantom Study.....	52

4.5 Results of the Second Phantom Study.....	55
4.6 Comparison: the Reconstruction Time of Reconstruction Algorithms...	58
4.7 Comparison: the Number of Projections.....	61
4.8 Comparison: FBP Algorithm and OS-type SART Algorithm.....	63
5. DISCUSSION.....	70
5.1 System Design: Spatial Filter.....	70
5.2 Refractive Index.....	73
5.3 Comparison of Reconstruction Algorithms.....	74
5.4 Artifacts in Reconstruction Images.....	77
5.5 Conclusion.....	81
APPENDIX	
A. PROGRAMMING.....	83
BIBLIOGRAPHY.....	
	117

## LIST OF ILLUSTRATIONS

Figure	Page
1: The idea of the new optical transillumination scanner.....	10
2: Schematic diagram of the optical transillumination tomography.....	12
3: The spectrum of absorption for a vascular graft.....	13
4: The projection of Teflon tube using a laser as light source.....	14
5: The projection of Teflon tube using a LED as light source.....	15
6: Schematic diagram of modified optical transillumination tomography.....	16
7: Basic scheme of optical transillumination tomography.....	17
8: The two-dimensional digital phantom comprises a graft tissue fixed in the mandrel.....	18
9: The projection of attenuated intensity for Figure 6 at the first angle.....	18
10: The sinogram of attenuated intensity for Figure 6.....	19
11: The sinogram of attenuated intensity for Figure 6.....	19
12: The Fourier transform.....	20
13: Graphical representation of the Fourier slice theorem.....	22
14: The FBP reconstruction using Hamming filter with cut-off frequency 0.2.....	24
15: The FBP reconstruction using Hamming filter with cut-off frequency 0.4.....	24
16: The FBP reconstruction using Hamming filter with cut-off frequency 0.6.....	24
17: The FBP reconstruction using Hamming filter with cut-off frequency 0.8.....	24
18: The FBP reconstruction with 400 angular samples over 360 degrees.....	25
19: The FBP reconstruction with 200 angular samples over 360 degrees.....	25

20: The FBP reconstruction with 100 angular samples over 360 degrees.....	26
21: The FBP reconstruction with 50 angular samples over 360 degrees.....	26
22: The OS-SMART reconstruction using 8 subsets with 1 iterations.....	30
23: The OS-SMART reconstruction using 8 subsets with 2 iterations.....	30
24: The OS-SMART reconstruction using 8 subsets with 4 iterations.....	30
25: The OS-SMART reconstruction using 8 subsets with 8 iterations.....	30
26: The OS-SMART reconstruction using 8 subsets with 12 iterations.....	31
27: The OS-SMART reconstruction using 8 subsets with 16 iterations.....	31
28: The geometry of calculating qualities in Siddon's method.....	32
29: The two-dimensional digital phantom.....	35
30: The reconstruction image using the traditional method.....	35
31: The reconstruction image using the rotation-based method.....	35
32: The horizontal image profile of Figure 29, 30 and 31 along the central row.....	35
33: The configuration of the first phantom.....	37
34: The projection of the PTFE tube with 100mL water and 0 g (right) and 1 g (left) sucrose.....	38
35: The projection of the PTFE tube with 100mL water and 2 g (right) and 3 g (left) sucrose.....	38
36: The projection of the PTFE tube with 100mL water and 3.4 g (right) and 3.6 g (left) sucrose.....	39
37: The projection of the PTFE tube with 100mL water and 3.8 g (right) and 4 g (left) sucrose.....	39
38: The projection of the PTFE tube with 100mL water and 4.2 g (right) and 4.4 g (left) sucrose.....	39
39: The profile of the projection at the first angle. The solution inside and outside the PTFE tube is 3.8% sucrose.....	41
40: The profile of the projection at the first angle. The solution inside the PTFE tube is 3.8% sucrose with ink. The solution outside the PTFE tube is 3.8% sucrose.....	41

41: The profile of the projection data ( $g_\theta$ ) at the first angle.....	42
42: The sinogram, which is composed of the projection data ( $g_\theta$ ) angle by angle.....	42
43: The sinogram without the correction of registration.....	43
44: The sinogram with the correction of registration.....	43
45: The image reconstruction using FBP algorithm without the correction of registration.....	44
46: The image reconstruction using FBP algorithm with the correction of registration.....	44
47: The image reconstruction using FBP algorithm without the correction of COR.....	45
48: The image reconstruction using FBP algorithm with the correction of COR.....	45
49: The image reconstruction (ink1) using OS-type SART algorithm with 20 subsets and 20 iterations.....	46
50: The image reconstruction (ink2) using OS-type SART algorithm with 20 subsets and 20 iterations.....	46
51: The image reconstruction (ink3) using OS-type SART algorithm with 20 subsets and 20 iterations.....	47
52: The image reconstruction (ink4) using OS-type SART algorithm with 20 subsets and 20 iterations.....	47
53: The image reconstruction (ink5) using OS-type SART algorithm with 20 subsets and 20 iterations.....	47
54: The image reconstruction (ink6) using OS-type SART algorithm with 20 subsets and 20 iterations.....	47
55: The sinogram of Figure 43.....	48
56: The sinogram of Figure 44.....	48
57: The sinogram of Figure 45.....	48
58: The sinogram of Figure 46.....	48
59: The sinogram of Figure 47.....	48
60: The sinogram of Figure 48.....	48
61: The relation of attenuation coefficients between our OT system and spectrophotometer.....	50

62: The configuration of the second phantom.....	52
63: The projection of the PTFE tube with 100 mL water and 3.8 g (left) and 4.0 g sucrose (right).....	53
64: The projection of the PTFE tube with 100 mL water and 4.2 g (left) and 4.4 g sucrose (right).....	53
65: The projection of the PTFE tube with 100 mL water and 4.6 g (left) and 4.8 g sucrose (right).....	54
66: The projection of the PTFE tube with 100 mL water and 5.0 g (left) and 5.2 g sucrose (right).....	54
67: The sinogram of 270 <sup>th</sup> slice without corrections of registration and COR.....	55
68: The sinogram of 270 <sup>th</sup> slice with corrections of registration and COR.....	55
69: The projection of the second phantom without ink between two PTFE tubes at 100 <sup>th</sup> angles.....	55
70: The projection of the second phantom with ink between two PTFE tubes at 100 <sup>th</sup> angles.....	55
71: The image reconstruction of Figure 67 using OS-type SART algorithm with 20 subsets and 20 iterations.....	57
72: The reconstruction image of Figure 68 using OS-type SART algorithm with 20 subsets and 20 iterations.....	57
73: The reconstruction image of 150 <sup>th</sup> slice using OS-type SART algorithm with 20 subsets and 20 iterations.....	57
74: The surface rendering is a part of the second phantom.....	57
75: The reconstruction image of 270 <sup>th</sup> slice using OS-type SART algorithm with 1 subset and 100 iterations.....	60
76: The reconstruction image of 270 <sup>th</sup> slice using OS-type SART algorithm with 5 subset and 20 iterations.....	60
77: The reconstruction image of 270 <sup>th</sup> slice using OS-type SART algorithm with 10 subset and 10 iterations.....	60
78: The reconstruction image of 270 <sup>th</sup> slice using OS-type SART algorithm with 20 subset and 5 iterations.....	60

79: The reconstruction image of ink6's 270 <sup>th</sup> slice using OS-type SART algorithm with 400 projections.....	62
80: The reconstruction image of ink6's 270 <sup>th</sup> slice using OS-type SART algorithm with 200 projections.....	62
81: The reconstruction image of ink6's 270 <sup>th</sup> slice using OS-type SART algorithm with 100 projections.....	62
82: The reconstruction image of ink6's 270 <sup>th</sup> slice using OS-type SART algorithm with 50 projections.....	62
83: The reconstruction image of ink6's 270 <sup>th</sup> slice using the FBP algorithm (Hamming filer and 0.8 cut-off frequency) with 400 projections.....	66
84: The reconstruction image of ink6's 270 <sup>th</sup> slice using the OS-type SART algorithm (5 subsets and 20 iterations) with 400 projections.....	66
85: The reconstruction image of ink6's 270 <sup>th</sup> slice using the OS-type SART algorithm (10 subsets and 10 iterations) with 400 projections.....	66
86: The reconstruction image of ink6's 270 <sup>th</sup> slice using the OS-type SART algorithm (20 subsets and 5 iterations) with 400 projections.....	66
87: The reconstruction image of ink6's 270 <sup>th</sup> slice using the FBP algorithm (Hamming filer and 0.8 cut-off frequency) with 200 projections.....	67
88: The reconstruction image of ink6's 270 <sup>th</sup> slice using the OS-type SART algorithm (5 subsets and 20 iterations) with 200 projections.....	67
89: The reconstruction image of ink6's 270 <sup>th</sup> slice using the OS-type SART algorithm (10 subsets and 10 iterations) with 200 projections.....	67
90: The reconstruction image of ink6's 270 <sup>th</sup> slice using the OS-type SART algorithm (20 subsets and 5 iterations) with 200 projections.....	67
91: The reconstruction image of ink6's 270 <sup>th</sup> slice using the FBP algorithm (Hamming filer and 0.8 cut-off frequency) with 100 projections.....	68
92: The reconstruction image of ink6's 270 <sup>th</sup> slice using the OS-type SART algorithm (5 subsets and 20 iterations) with 100 projections.....	68
93: The reconstruction image of ink6's 270 <sup>th</sup> slice using the OS-type SART algorithm (10 subsets and 10 iterations) with 100 projections.....	68
94: The reconstruction image of ink6's 270 <sup>th</sup> slice using the OS-type SART algorithm (20 subsets and 5 iterations) with 100 projections.....	68

95: The reconstruction image of ink6's 270 <sup>th</sup> slice using the FBP algorithm (Hamming filter and 0.8 cut-off frequency) with 50 projections.....	69
96: The reconstruction image of ink6's 270 <sup>th</sup> slice using the OS-type SART algorithm (5 subsets and 20 iterations) with 50 projections.....	69
97: The reconstruction image of ink6's 270 <sup>th</sup> slice using the OS-type SART algorithm (10 subsets and 10 iterations) with 50 projections.....	69
98: The reconstruction image of ink6's 270 <sup>th</sup> slice using the OS-type SART algorithm (20 subsets and 5 iterations) with 50 projections.....	69
99: The diagram of the spatial filter.....	70
100: The image reconstruction of Figure 64 using OS-type SART algorithm with 20 subsets and 20 iterations.....	79
101: The profile of the projection (450 <sup>th</sup> slice) at 250 angles.....	79

## LIST OF TABLES

Table	Page
1: The attenuation coefficient measured from our OT system and spectrophotometer in different ink's concentrations.....	49
2: The accuracy of measured radius in different ink's concentration.....	51
3: The reconstruction time of each reconstruction algorithm.....	59
4: The reconstruction time and SNR of OS-type SART algorithm with different angles over 360 degrees.....	61
5: The SNR of the OS-type SART algorithm and the FBP algorithm with different angles over 360 degrees.....	63

# DEVELOPMENT OF HIGH-RESOLUTION OPTICAL TOMOGRAPHY WITH LARGER-SIZE PROJECTION ACQUISITION

Hsuan-Ming Huang

Dr. Mark Haidekker, Thesis Supervisor

## ABSTRACT

In the industrial countries, the mortality from arteriosclerosis and cardiovascular diseases has been decreased, but they remain the most common circulatory disease. Recently, new tissue engineering technologies such as tissue-engineered blood vessels (TEBV), produced from a patient's own cells, are becoming available to treat these diseases. In order to monitor the quality of TEBV and assess biomechanical properties, a nondestructive and minimally invasive method is necessary. Optical Tomography (OT) is a proper imaging method because it satisfies the above requirements. Besides, the benefits of OT include: low cost, simple design and ultra fast acquisition.

The purpose of this project was to develop an ultra-fast 3D OT scanner by using a beam expander and larger-size CCD cameras instead of pencil beam and smaller-size detectors. The new device is capable of imaging an axial section of about 4mm height in one single revolution. The new OT scanner will primarily be used to obtain the biomechanical properties, the geometry and defects of TEBV. The new device was evaluated by using phantom studies and then tested its performance for the thin tissue layer of TEBV, obtained from Cytograft Tissue Engineering. The results show that the new system has the potential to be a low cost, high tissue contrast, rapid and simple scanner.

# CHAPTER 1

## BACKGROUND

### 1.1 Vascular Graft Tissue Engineering

During the past decade, the requirement of transplanting organs and tissues has been increased undoubtedly. However, the rate of donating organs and tissues is relatively low and there are issues with rejection and lifelong medication. Fortunately, the progress of tissue engineering has allowed for the production of artificial organs and replacement tissues such as skin substitutes [Auger et al., 2004], heart valves [Neuenschwander et al., 2004], corneas [Griffith et al., 2002] and bone [Suh et al., 2001] within the last decade. The idea also has been applied to the field of blood vessels affected by cardiovascular diseases. A common cardiovascular disease in the modern world is arteriosclerosis. One common treatment is to graft replacement blood vessels.

The definition of arteriosclerosis is the formation of plaques of cholesterol, platelets, fibrin, and other substances on the arterial walls. It leads to progressive degrees of blockage of the arterial circulation. The known cause includes smoking, high cholesterol levels, high blood pressure, hereditary susceptibility and diabetes. The common site is the

artery of the legs and its block causes an aching muscle pain in the early stages due to insufficient blood [Internet Health Library, 2006]. When the problem becomes severe, the limb becomes cold, pale and discolored. In addition to limbs, obstruction of coronary arteries induces chest pain and the obstruction of arteries in the brain results in a stroke. Typical medical treatment includes light exercise (for early stages), drug therapy and surgery.

With the development of interventional techniques such as angioplasty and stenting, the need of bypass surgery for many patients has been reduced. However, the primary therapeutic method to relieve the obstruction is still bypass surgery. For small diameter vessels (<6 mm), the best vascular grafts are obtained from patient's own vessels [Bergan et al., 1982; Charlesworth et al., 1985; Sapsford et al., 1981; Yeager et al., 1982]. For example, one feasible approach is to graft a healthy vessel from the leg to the affected region. This is called revascularization. Unfortunately, the supply of autologous vessels becomes insufficient with multiple revascularization surgeries. An alternative method is to use artificial grafts. Although such grafts have been very successful for larger blood vessel replacement [Mannick et al., 1986], the small diameter synthetic vascular grafts currently available have been shown poor patency rates [Bushberg et al., 2002; Van de

Pavoordt et al., 1986; Yeager et al., 1982]. Problems of synthetic materials, especially in small diameter vessels, include inflammation [Anderson and Ziats, 1991; Greisler 1990; Parsson et al., 1993] and infection [Bergamini et al., 1988; Mertens et al., 1995] that increase mortality. The use of vessels from animal or cadaver vessels is possible, but these vessels suffer from tissue degradation, dilation and aneurysm formation [Allaire et al., 1994; Dardik et al., 1988; Guidoin et al., 1980; Allaire et al., 1994; Roberts and Hopkinson, 1977].

Within the last decade, significant progress in the field of tissue engineering has allowed production of artificial vascular grafts that can be applied to clinical cases. In 1986, researchers presented the first tissue-engineered blood vessel (TEBV) [Weinberg and Bell, 1986] that consisted of collagen and cultured cells. Later, a different research group reproduced the blood vessel following the model, but both studies resulted in poor biomechanical strength [L'Heureux et al., 1993]. Recently, a new method to produce TEBV from a patient's own cells was introduced [L'Heureux et al., 1998; 2001]. This approach was the first human completely biological living TEBV that satisfied the three expected properties [L'Heureux et al., 1998; 2001]: mechanical strength, blood compatibility and suturability. This technology also promised the availability of small

diameter TEBV from patient's own cells.

Unfortunately, the TEBV produced from a patient's own cell is expensive. Therefore, quality control of the TEBV is required. Since the TEBV is produced using a patient's own cell in small individual batches, statistical testing is not feasible and inconvenient. Under the requirement of a fast, convenient and minimum invasive quality control, imaging techniques provide a potential approach. An appropriate imaging modality would have the ability to obtain useful properties about TEBV such as homogeneity, shape and thickness. In addition, the detection of potential artifacts such as inhomogeneities, delamination, air bubbles and enclosed fluid bubbles is necessary.

## **1.2 Common Imaging Techniques for Tissue Engineered Blood Vessel**

Within the last 20 years, popular imaging modalities such as computed tomography (CT), ultrasound and magnetic resonance imaging (MRI) have been used widely in many fields, especially in medicine. However, existent studies that attempt to provide desired information of the blood vessel are very few. In order to assess the feasibility of these modalities, preliminary experiments were performed in earlier projects. Based on preliminary studies, we will summarize these modalities in the next paragraph.

The first CT scan for the blood vessel was performed on an ImTek MicroCAT II scanner with a nominal in-plane resolution of  $34 \mu m$  with Feldkamp cone-geometry back-projection. In summary, the imaging acquisition using CT is conventional and fast. Furthermore, the spatial resolution, signal-to-noise ratio (SNR) and tissue-air contrast of the CT image are excellent provided that the vessel is imaged in the air. However, the vessel must be immersed in its protective fluid. When the vessel is imaged with fluid, the tissue-fluid contrast is insufficient. Since removing a blood vessel from its protective fluid is unacceptable, CT cannot be considered a feasible modality (unpublished data).

MRI was a modality that provided excellent tissue-fluid contrast with  $T_1$ -weighted spin-echo and inversion recovery sequences. Other sequences such as  $T_2$ -weighted and proton density weighted did not show any noticeable tissue-fluid contrast. Unfortunately, using clinical scanners is unfeasible due to low spatial resolution, poor SNR and time-consuming acquisition. Although specialized instruments such as microMRI have the potential providing good resolution and SNR, they are extremely expensive and are not within the budget of small tissue-engineering companies. A more recent imaging experiment using the new 7T Varian magnet and the small-animal scanning system provided surprising poor results as well (unpublished data). It appears that MRI, like CT,

would require the use of contrast agents to achieve acceptable image quality. However, contrast agents cannot be used due to FDA restrictions.

Like MRI, ultrasound imaging needs specialized instruments. Clinical scanners with signals up to 15MHz to scan blood vessel result in low resolution, poor SNR and a broad double-echo between the interface of mandrel-tissue and tissue-fluid, which leads to inaccurate spatial measurements. Furthermore, positioning of the both blood vessel accurately over the ultrasound probe is necessary. Therefore, only using clinical scanners is a difficult job. Potentially, the new 40 MHz scanners might provide better spatial resolution, but lack of availability precluded their use.

### **1.3 Special Imaging Techniques, Optical Tomography, for Blood Vessel**

Experiments that apply visible light to study the optical properties of soft tissues date back as far as 1929 [Cutler et al., 1929], but several studies [Bartrum and Crow, 1984; Drexler et al., 1985; Marshall et al., 1984] showed low sensitivity and specificity for example in the diagnosis of breast cancer. The primary problems using light to penetrate biological tissue are the tissue's high attenuation and scattering of light. With the development of novel techniques such as sensitive CCD cameras, new light sources

(lasers) and new mathematical models of light propagation in diffusive tissues [Colak et al., 1997], significant progress was made. One of the main modalities that has found with applicability today is OCT [Huang et al., 1991]. The typical OCT comprises a short coherent laser and a Michelson interferometer. Light is split into reference and sample beam and then recombined before hitting the detector. The length of reference arm is variable, corresponding to the depth of the coherent section in the sample. By measuring scattered light from that section, we can obtain scattering intensity as a function of depth. This is very similar to the A-mode scan of ultrasound. Commercially available OCT could turn out to be superior to CT, ultrasound and MRI, since optical properties of the blood vessel are quite different from the surrounding fluid. Therefore, good tissue-fluid contrast is feasible. OCT can provide a resolution of 13 $\mu$ m per pixel and achieve accurate thickness measurements in thin tissue sections. In addition, SNR for normal graft tissue samples is acceptable, and the detection of defects such as fluid bubbles is possible. However, OCT with a full image acquisition (360 degree over the full length of the graft) would take typically several hours. For example, we assume the voxel size of the detector equals 5  $\mu$ m. For a 5 mm diameter vessel (circumference= 12.5mm), the number of A-mode scans is about 2,500,000  $((12.5/0.005) \times (5/0.005))$ . Generally, the full length

of a vessel is approximate 50 mm, which needs 25,000,000 scans ( $2,500,000 \times 10$ ). Today, commercial OCT devices (rapid Fourier domain scanners) can provide up to 8000 scans per second. This leads to 3125 seconds or 52 minutes, which is fairly slow, but acceptable. However, the scan time becomes an issue if higher resolution is required. Under this situation, the development of a faster scanner that OCT is necessary.

One completely different method is optical transillumination (OT) tomography. The basic idea of OT is to use ballistic photons (non-scattered light). Through detecting ballistic photons before and after penetrating tissue, the attenuation coefficient of biological tissues can be reconstructed. Since the fundamental concept of OT is very similar to CT, common image reconstruction methods used in CT such as filtered back-projection (FBP) can be applied to OT directly. The primary problem in OT is the influence of multiply scattered photons. This can be suppressed by gating- multiply scattered photons arrive later than non-scattered photons [Chen et al., 2000], or polarizing- photons experience a complete randomization of their initial polarization state after multiple scatter events [Hebden et al., 1997]. Since these techniques reduce the effect of multiply scattered photons on image quality, the number of practical applications in OT has been increased recently. One of early applications was the detection of human

breast cancer [Bartrum and Crow 1984]. One study [Gayen et al., 1998] showed that better contrast and higher resolution were obtained when the object was imaged through normal human breast tissue than through a cancerous breast tissue under the use of a Fourier space gate and a polarization gate. In addition, one popular application in medical physics is the reconstruction of three-dimensional (3D) dose distribution from gel dosimeters, although the quantification of artifacts due to reflection, refraction and scattering was limited [Doran et al., 2001; Gore et al., 1996; Islam et al., 2003; Kelly et al., 1998; Maryanski et al., 1996; Oldham et al., 2001, 2003; Wolodzko et al., 1999]. Fortunately, the effect of geometric distortion and the underestimation of attenuation coefficients have been found to be negligible [Oldham and Kim, 2004] if a good scatter rejection collimator is used and the difference of refractive index is small. Thus, the accurate prediction of dose distribution in clinical complex external beam radiation treatments would be possible. Recently, the preliminary application of optical computed tomography (optical-CT) and optical emission tomography (optical-ET) showed that the new imaging technique has the potential to image the 3D distribution of tumor microvasculature and viable tumor distribution with excellent spatial resolution and contrast [Oldham et al., 2006]. In addition, the feasibility of early diagnosis for

rheumatoid arthritis was demonstrated [Yuasa et al., 2001] in vivo imaging. The other useful application was the development of a laser-optical CT scanner [Bellemann et al., 2002] for the use by students as part of their curriculum in biomedical engineering. This device could demonstrate the principle of CT imaging without any ionizing radiation.

To image TEBV, an OT scanner based on the first-generation CT scanner (a pencil beam with a single detector) was introduced recently [Gladish et al., 2005]. It was relatively inexpensive as compared to OCT, and it is easy to reconstruct images due to its

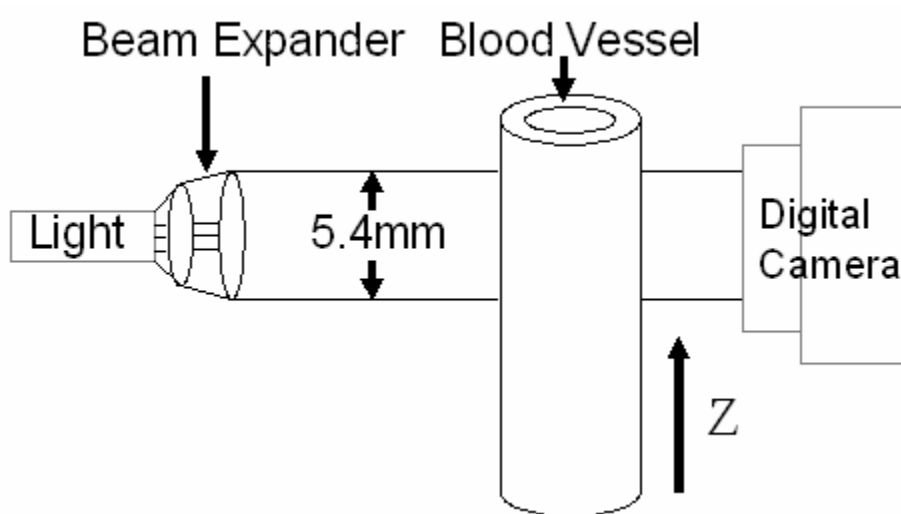


**Figure 1:** The idea of the new optical transillumination scanner. The light is expanded by a beam expander and the two-dimensional light through the blood vessel is collected by a larger-size detector.

mathematical simplicity. The scan time per slice was found to be less than 3 minutes.

However, the scan time for the full length of the graft would still take several hours. For

example, if the number of slices is 200, the scan time would be 600 minutes ( $= 3 \times 200$ )

or 10 hours, which is unacceptable, and the number of slice for a blood vessel is more

than 200. Apart from the speed, OT promises to be an attractive modality for imaging TEBV. It is the goal of this study to develop the second-generation OT scanner by using an expanded beam and a large-size detector in order to achieve faster scan. Figure 1 is the illustration of the new OT scanner. The thin light is expanded by a beam expander and the two-dimensional light through the blood vessel is collected by a large-size detector. In the first-generation OT scanner (a pencil beam with a single detector), one acquisition ( $360^{\circ}$  angles) only acquires one slice. This would take much time if the number of slice is large. By using a beam expander and a large-size detector, the new OT scanner can acquire many slices in one acquisition. For example, the length we scanned in one acquisition is 5.4mm ( $5/1000 \times 1080$ ) if the pixel size is  $5 \mu m$  and the number of pixel (slice) along the z direction of the detector is 1080. This can reduce the scan time largely. In the project, we built the new OT scanner using a beam expander and a large-size CCD camera at first. Then, we focused on evaluating the performance of the second-generation OT system using phantoms.

## CHAPTER 2

# Design of the New Optical Transillumination Tomography System

### 2.1 Basic Idea of the New OT System

The first generation CT scanner is based on a pencil beam and a single detector [Gladish et al., 2005]. This first-generation scanner was developed to the point of providing full 3D volumetric images. In practice, the first OT scanner was very inefficient because the scan time for the full length of a graft took several hours. In order to reduce the scan time, we used a beam expander (BE) and a large-size detector instead

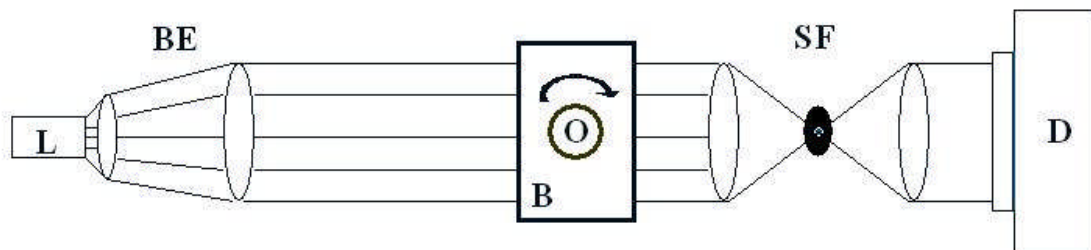


**Figure 2:** Schematic diagram of the optical transillumination (OT) scanner. A laser (L) produces red light which is expanded by beam expander (BE) and then the light penetrates object (O). The object is immersed in a sample bath (B) filled with a refraction index matching liquid. The object can be positioned to the angle to obtain necessary projections. The light after penetrating the sample is filtered by spatial filter (SF). The spatial filter allows only ballistic photons (parallel to original light direction) to pass which it rejects off-axis (scattered) photons. Finally, ballistic photons are collected with the detector (D).

of a pencil beam and single detector. The BE can translate a pencil beam into a three

dimensional (3D) collimated beam. This allows us to acquire multiple slices in one scan.

Figure 2 is the schematic diagram of the new OT scanner. A laser (L) provides red light, which is expanded by BE. Then the light is directed onto the sample. The sample is immersed in the bath (B) and it is fixed on a mandrel used for rotating the sample. In addition, we used two translation stages (not shown in the diagram) to adjust the position of the sample bath: One is used for adjusting the center of rotation. The other is used for moving the sample along vertical (axial) direction (slice). Then, the light passing the sample is filtered by a spatial filter (SF). The spatial filter that is composed of two lenses

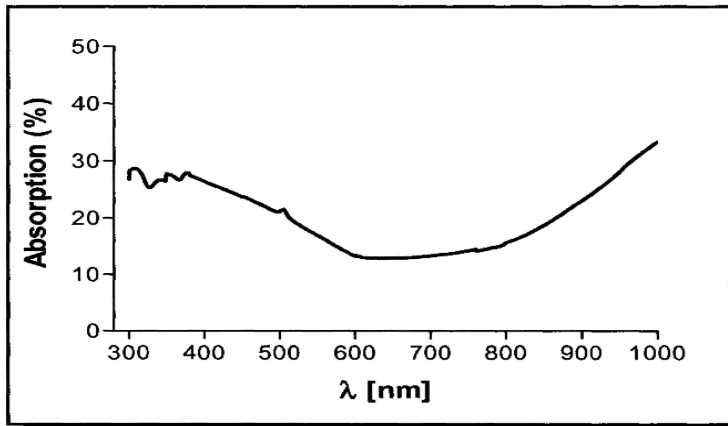


**Figure 3:** The typical absorption spectrum of a vascular graft. The absorption is minimum in the red light range (600-700nm).

refracted into high frequency components (far away from the center). Conversely, photons refracted by scattering media would be blocked by the pinhole, and the rejection angle is determined by the size of pinhole. The first lens is used to focus the parallel

and a pinhole and allows only ballistic photons (parallel to the original light direction) to pass. The screen around the pinhole blocks scattered photons since they are

beam into a point and the divergent beam after passing the pinhole is restored to parallel beam by the second lens. The pinhole must be in the focal plane (lenses' focal length). If the pinhole is not in the focal plane, the elimination of scattered photons is dependent on the refracted angle of scattered photons. Finally, ballistic photons are collected with a large-size detector (D). Here, we use a Silicon Imaging 12 bpp CCD camera which provides a resolution of  $1920 \times 1024$  pixels on a  $9.6 \times 5.4$  mm chip.

## 2.2 Design of the Modified OT System

First, we used a laser that produced red light sine the absorption of a vascular graft in minimum in the range (600-700nm) as shown in Figure 3. Unfortunately, the laser we

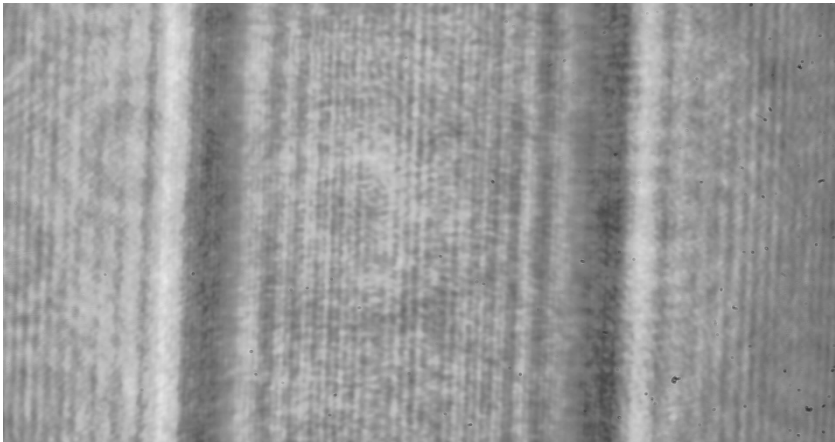


**Figure 4:** The projection of a Teflon tube using a laser as light source. The interference effect, a dark band followed by a bright band, is quite apparent.

used here resulted in an interference effect.

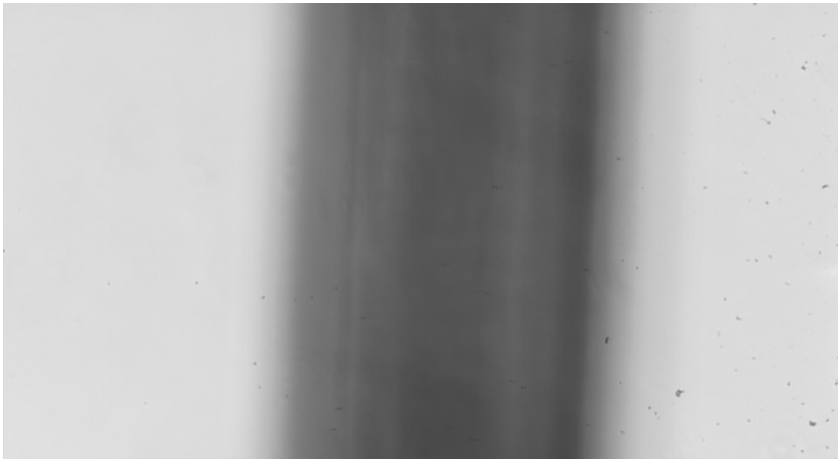
When the laser light passes through a small hole such as the

pinhole, a new wave

pattern will be produced because of the superposition of two or more waves. This is

called interference. It also means the interaction of waves, which are coherent with each other. The interference effect will produce a series of bright bands and dark bands.

Because the wavelength of the laser is narrow and the laser beam after passing BE is a



three-dimensional parallel beam, the interference effect was quite apparent.

Figure 4 shows the

**Figure 5:** The projection of a Teflon tube using a LED as light source. The interference is reduced.

projection of a Teflon

tube immersed in the sample bath. We can observe numerous bright and dark bands in the projection data. The broad dark region at the edge of the Teflon tube is called refraction region, where refracted photons are dominant. This indicates that the detected signal in this region is close to zero since most scattered photons are rejected by the SF.

One possible solution to avoid this artifact is to use high a power light emitting diode (LED), which is a semiconductor device that can emit incoherent and narrow light. In a modified design, we used a 625nm LED (Luxeon III star) with 20nm full width half maximum (FWHM) as light source. Figure 5 shows the projection of a Teflon tube using

the LED as light source. Compared to Figure 4, we observe that there is no interference effect. However, it is relatively difficult to collimate the light of LED. In order to produce

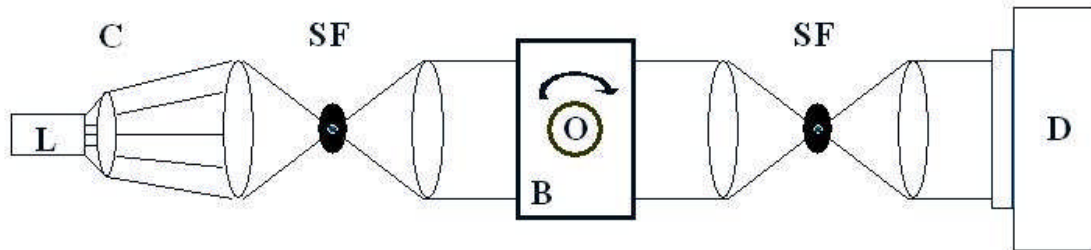


**Figure 6:** Schematic diagram of modified optical transillumination tomography device. Most components are the same as in Figure 1, except light source and beam expander. We use an LED (L) to reduce the interference effect and then collimate the LED's divergent light using a collimating lens (C). By using a spatial filter, an almost parallel beam can be obtained. Furthermore, using a spatial filter can improve the quality of beam.

a two-dimensional parallel beam, we use a collimating lens that completely covers the LED. Then, the divergent beam can be translated into a parallel beam using another spatial filter. This is shown in Figures 4 and 5. The projection using LED as light source is smoother than that using laser as light source. Figure 6 is the schematic diagram of the modified OT system. Basically, most components are the same as in Figure 2, except the light source and beam expander. The three-dimensional parallel beam can be obtained using a collimated lens (C) and a spatial filter (SF).

# CHAPTER 3

## OPTICAL TRANSILLUMINATION TOMOGRAPHY

### THEORY

#### 3.1 Principle of Optical Transillumination Tomography

In the new OT system, only ballistic photons are used for image formation. Since these photons propagate in a straight line, the light intensity at detector  $i$  can be calculated from Lambert-Beer's law:

$$I(i) = I_0(i) e^{-\int \mu_t(j) dj} \quad (1)$$

where  $I_0(i)$  is the incident light intensity at detector  $i$ ,  $\mu_t(j)$  is the total attenuation

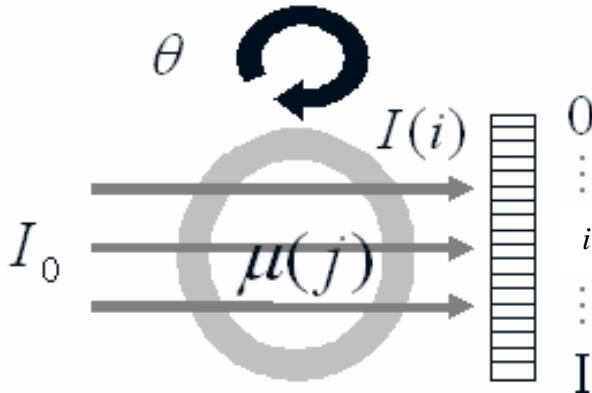


**Figure 7:** Basic scheme of optical transillumination tomography.  $I_0(i)$  is the incident light intensity at detector  $i$ ,  $\mu_t(j)$  is the attenuation coefficient along a straight path  $j$ .  $I(i)$  is the transmitted light at detector  $i$

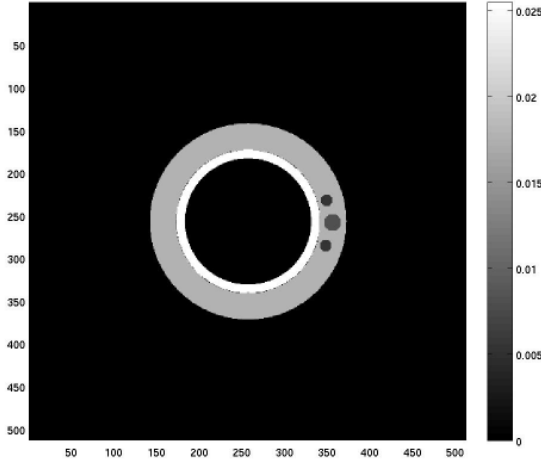
coefficient along a straight path  $j$ .

Figure 7 is the scheme of the OT system. Generally,  $\mu_t$  is the sum of absorption coefficient  $\mu_a$  and scattering coefficient  $\mu_s$  of the sample. According to Equation 1, the projection data  $g(i)$  at detector  $i$

can be represented by

$$g_{\theta}(i) = \ln\left(\frac{I_0(i)}{I(i)}\right) = \int \mu_t(j) dj \quad (2)$$

For example, a two-dimensional digital phantom (512×512) was presented [Haidekker, 2005] as shown in Figure 8. The inner layer represents the mandrel and the outer layer corresponds to graft tissue with idealized air bubbles. Figure 9 is the attenuated intensity



**Figure 8:** A two-dimensional digital phantom composed of a mandrel (inner layer) and a graft tissue (outer layer) with three air bubbles.

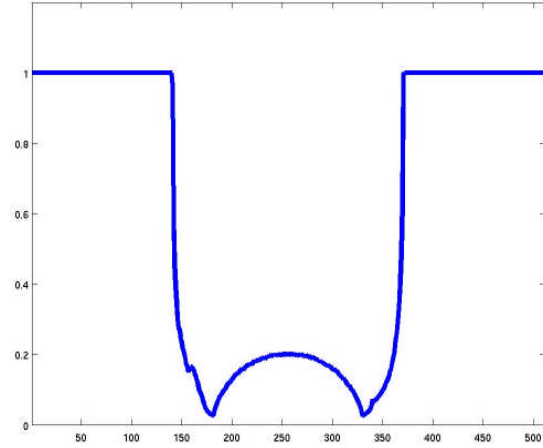


**Figure 9:** The attenuated intensity ( $I(i)$ ) Figure 6 at the first angle.

( $I(i)$ ) of Figure 8 at the first angle. The horizontal axis is detector index  $i$ , and the vertical axis is the intensity  $I$ . We assume that there is no noise, scattered photons or refractive index mismatch. The incident intensity ( $I_0$ ) is assumed to be unity and the number of detectors ( $i$ ) is 512. After collecting the attenuated intensity ( $I$ ) for each projection angle over a full  $360^\circ$  revolution, we obtain the projection image, which is

referred to as sinogram. Figure 10 is the sinogram of the attenuated intensity ( $I$ ) with 400 angles over 360 degrees (0.9 degree per angle). The horizontal axis is the detector index and the vertical axis is the angle index. In order to obtain the reconstruction image of attenuation coefficients, we need to translate the attenuated intensity ( $I$ ) into projection data ( $g_{\theta}(t)$ ) through Equation 2 as shown in Figure 11.

Usually, CT image reconstructions can be separated into two groups: analytical and iterative algorithms. The most common analytical algorithm used in CT is the filtered backprojection (FBP) algorithm since the FBP algorithm is very fast and is very easy to

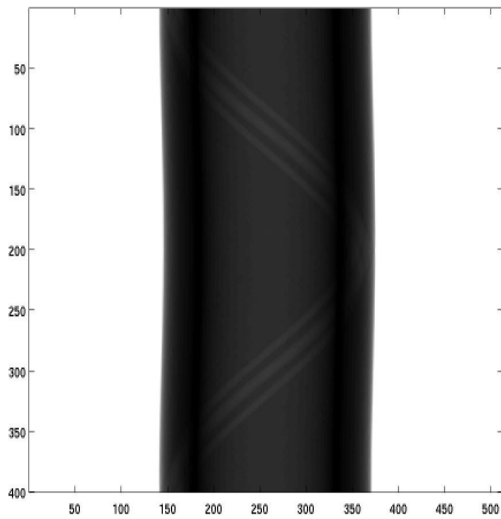


**Figure 10:** The sinogram of attenuated intensity ( $I$ ). The horizontal axis is the number of detector and the vertical axis is the number of angle.

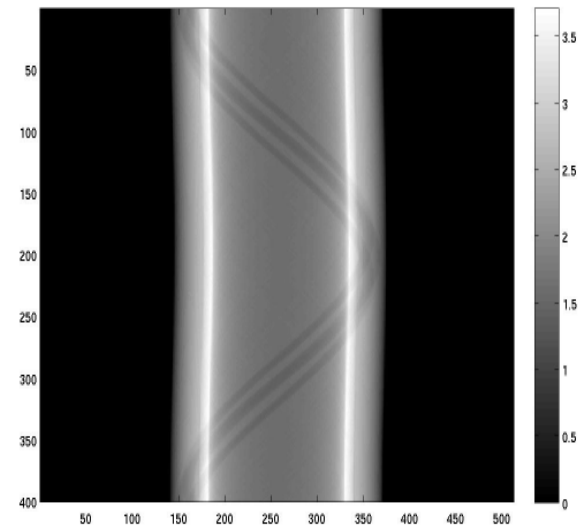


**Figure 11:** The sinogram of attenuated intensity ( $g$ ), which is obtained through Equation 2.

implement. However, the image reconstruction using FBP leads to higher errors as compared to iterative algorithms. Unlike analytical algorithms, iterative algorithms have

good performance in resolution and lower errors. However, its computational efficiency is relatively poor. Fortunately, there are many strategies used for reducing reconstruction time with iterative algorithms. The fundamental concept of both algorithms will be summarized in the next paragraph. Furthermore, we will introduce several strategies for increasing the efficiency of iterative algorithms.

### 3.2 Analytical Algorithms: Filtered Backprojection (FBP)

Generally, the tomographic projection process can be simplified as the Radon transform, which is the integral of a two-dimensional (2D) object  $\mu(i, j)$  along a straight line. The integral is called projection. In Figure 12, the intensity of projection data  $g_\theta(t)$  at detector  $t$  with an angle  $\theta$  from  $i$  axis can be represented by the

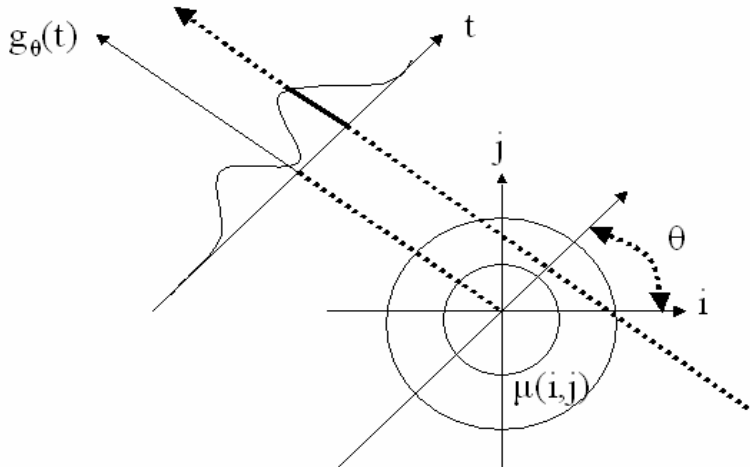


**Figure 12:** The Radon transform (line integral  $g_\theta(t)$  of the object  $\mu(i, j)$ ).

following equation:

$$g_{\theta}(t) = \int_{-\infty}^{\infty} \int_{-\infty}^{\infty} \mu(i, j) \delta(i \cos \theta + j \sin \theta - t) di dj \quad (3)$$

The Radon transform of  $\mu(i, j)$  [Oppenheim and Schaffer, 1989], indicates the sum of the 2D object along the projection line. Based on the Fourier slice theorem [Oppenheim and Schaffer, 1989], the relation between the one-dimensional (1D) Fourier transform of projection data  $g_{\theta}(t)$  and the 2D Fourier transform of  $\mu(i, j)$  can be derived. First, we define  $U(u, v)$  as the 2D Fourier transform of object  $\mu(i, j)$  and  $G_{\theta}(\omega)$  is the 1-D Fourier transform of projection data ( $g_{\theta}(t)$ ), which is defined as:

$$G_{\theta}(\omega) = \int_{-\infty}^{\infty} g_{\theta}(t) \exp(-j2\pi\omega t) dt \quad (4)$$

By substituting with Equation 3, Equation 4 can be rewritten as:

$$\begin{aligned} G_{\theta}(\omega) &= \int_{-\infty}^{\infty} \left\{ \int_{-\infty}^{\infty} \int_{-\infty}^{\infty} \mu(i, j) \delta(i \cos \theta + j \sin \theta - t) di dj \right\} \exp(-2j\pi\omega t) dt \\ &= \int_{-\infty}^{\infty} \int_{-\infty}^{\infty} \mu(i, j) \exp[-2j\pi\omega(i \cos \theta + j \sin \theta)] di dj \\ &= U(u, v) \text{ for } u = \omega \cos \theta, \quad v = \omega \sin \theta \\ &= U(\omega, \theta) \end{aligned} \quad (5)$$

Figure 13 describes the transformation from Equation 4 to Equation 5. It means that the 1D Fourier transform of projection data  $g_{\theta}(t)$ ,  $G_{\theta}(\omega)$ , is found in  $U(\omega, \theta)$  along a straight line with the angle  $\theta$  in the frequency transform  $U(u, v)$  of the data  $\mu(i, j)$ .

The resulting algorithm would demand the collection of sufficient projection data to fill

the 2D Fourier transform of the (unknown) reconstruction image  $U(u, v)$  with the 1D Fourier transforms of the projection data,  $G_\theta(\omega)$ . A subsequent inverse Fourier transform of the filled reconstruction space would now yield the reconstructed

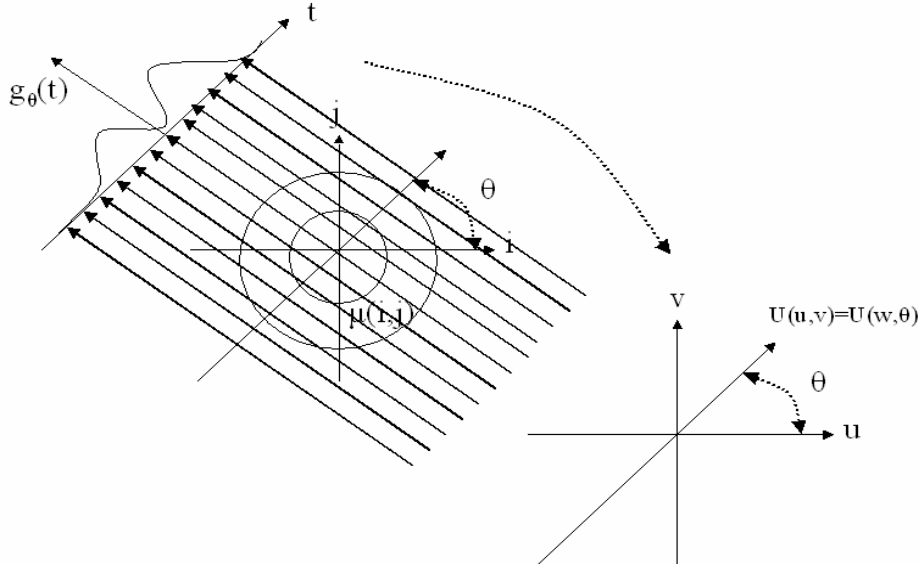


**Figure 13:** Graphical representation of the Fourier slice theorem. The Fourier transform of projection data  $g_\theta(t)$  at angle  $\theta$  equals to  $U(u, v)$ , a line at angle  $\theta$  in the  $uv$  plane.

cross-section  $u(i, j)$ . The process is represented by Equation 6:

$$\mu(i, j) = \int_{-\infty}^{\infty} \int_{-\infty}^{\infty} U(u, v) e^{j2\pi(ui+vj)} dudv \quad (6)$$

By converting the Cartesian coordinates  $(u, v)$  to polar coordinates  $(\omega, \theta)$  in the frequency domain, Equation 6 can be expressed as

$$\begin{aligned} \mu(i, j) &= \int_0^{2\pi} \int_0^{\infty} U(\omega, \theta) \exp[j2\omega(i \cos \theta + j \sin \theta)] \omega d\omega d\theta \\ &= \int_0^{\pi} \int_{-\infty}^{\infty} U(\omega, \theta) |\omega| \exp(j2\pi\omega t) d\omega d\theta \\ &= \int_0^{\pi} \int_{-\infty}^{\infty} G_\theta(\omega) |\omega| \exp(j2\pi\omega t) d\omega d\theta \end{aligned} \quad (7)$$

where  $U(\omega, \theta) = G_\theta(\omega)$  and  $t = i \sin \theta + j \cos \theta$ . The result in Equation 7 can be simplified as

$$\mu(i, j) = \int_0^\pi q_\theta(t) d\theta \quad (8)$$

$$\text{where } q_\theta(t) = \int_{-\infty}^{\infty} H(\omega) G_\theta(\omega) \exp(j2\pi\omega t) d\omega \quad (9)$$

In Equation 9, the filtered projection data,  $q_\theta(t)$ , is the inverse Fourier transform of projection data ( $G_\theta(\omega)$ ) associated with a ramp filter  $H(\omega) = |\omega|$ . Equation 8 describes the reconstruction process exclusively in the spatial domain. This process requires a filtering step (Equation 9), which can be performed either in the frequency domain or as a convolution operated in the spatial domain. This reconstruction process is therefore referred to as filtered backprojection (FBP). However, noise in high frequency domain data would be amplified because ramp filter is to amplify signal with the increase of frequency. A side effect is the amplification of noise. In order to reduce the amplification of noise at high frequencies, one alternative is to combine the ramp filter with other filters such as Hanning or Hamming filters [Cho et al., 1993; Rosenfeld and Kak, 1982].

This section provides an example of image reconstruction using simulated projection data with the FBP algorithm. We assumed there was no noise, scattered photons or refractive index mismatch in this example. In the following section, we will use the

digital phantom in Figure 8 to produce a simulated sinogram with 200 angles over 360 degrees (1.8 degree per angle) and then perform FBP reconstruction with Hamming filter ( $0.54 + 0.46 \times \cos(\omega / \omega_c)$ , where  $\omega$  is the spatial frequency and  $\omega_c$  is the cut-off frequency). The cut-off frequency determines the image quality and ranges between 0 and 1. For example, signals with normalized frequencies from 0.2 to 1 would be attenuated if the cut-off frequency is 0.2. To observe the performance of FBP reconstruction, we use

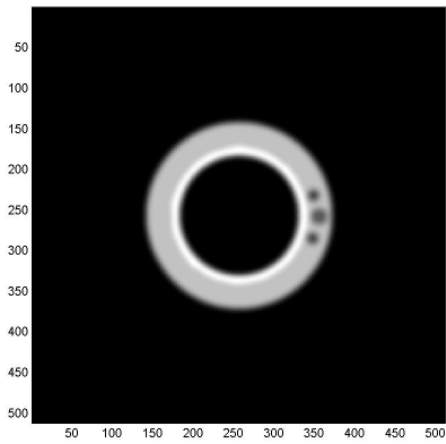


**Figure 14:** The FBP reconstruction using Hamming filter with cut-off frequency 0.2.

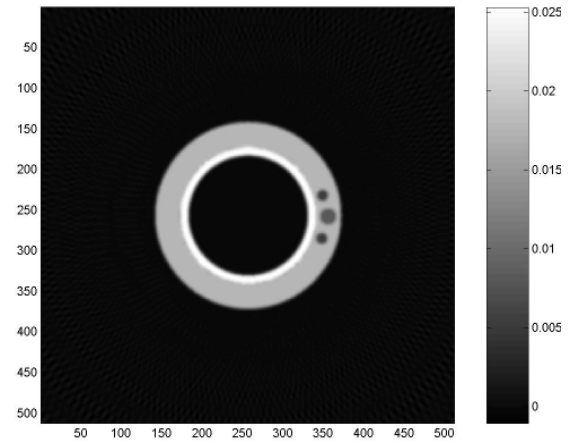


**Figure 15:** The FBP reconstruction using Hamming filter with cut-off frequency 0.4.

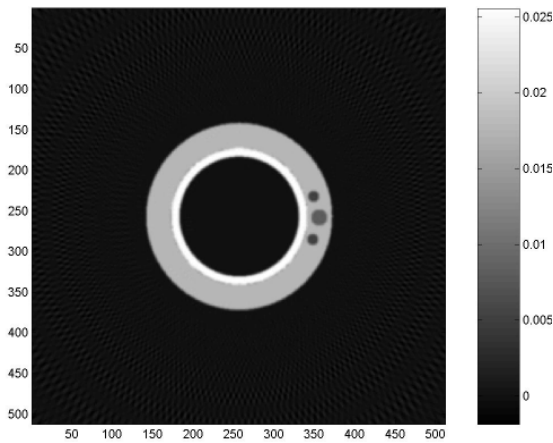


**Figure 16:** The FBP reconstruction using Hamming filter with cut-off frequency 0.6.

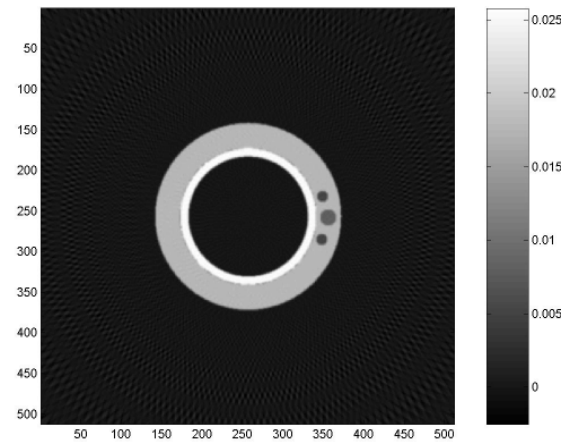


**Figure 17:** The FBP reconstruction using Hamming filter with cut-off frequency 0.8.

different cut-off frequencies including 0.2, 0.4, 0.6 and 0.8. From Figure 14 to Figure 17, the decrease of the cut-off frequency leads to a loss of image detail. Usually, signals in high frequencies represent the detail of the image such as the edges or boundaries. Small cut-off frequencies would attenuate the signal at high frequencies. As a result, this causes the degradation of spatial resolution (blurring). As can be seen in Figure 14-17, increasing the cut-off frequency clearly reduces blurring and leads to a sharper image.

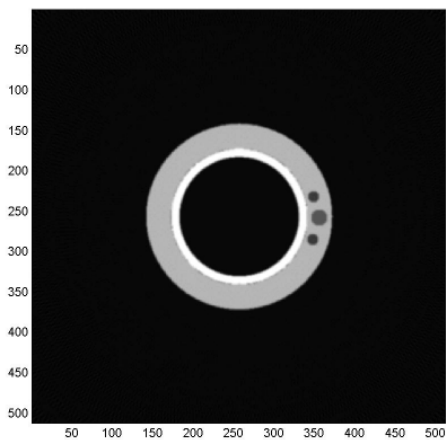


**Figure 18:** The FBP reconstruction with 400 angular samples over 360 degrees.

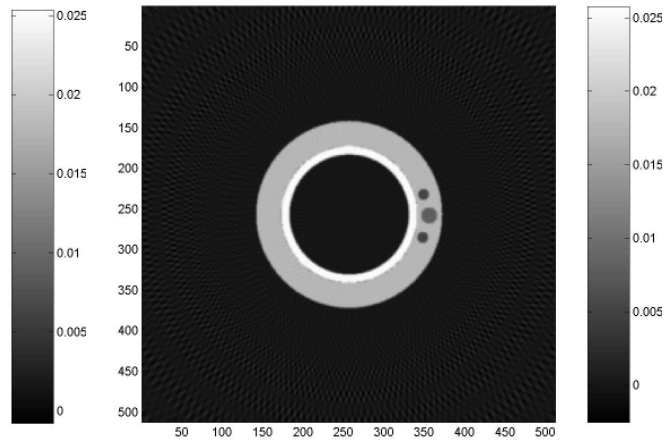


**Figure 19:** The FBP reconstruction with 200 angular samples over 360 degrees.

Since the simulation data contains no noise, however, the effect of noise suppression cannot be seen. In real data, the determination of the cut-off frequency is primarily related to the degree of noise. Generally, high noise component requires a smaller cut-off frequency for noise reduction, but this would also result in a loss of image detail. Thus, the choice of a cut-off frequency involves a tradeoff between spatial resolution and noise.

The other factor affecting the image quality is the number of angular projections. For

example, we use the phantom in Figure 8 to produce a sinogram with 400, 200, 100 and

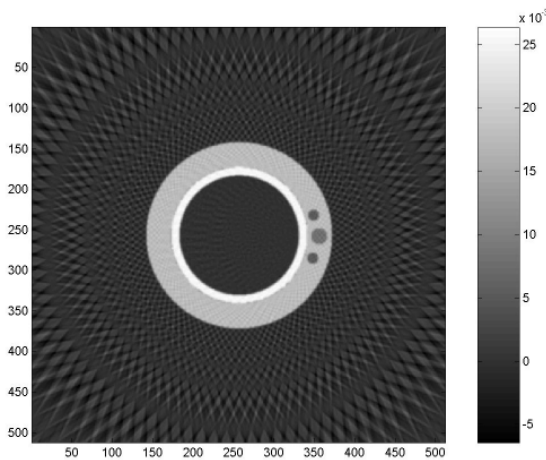


**Figure 20:** The FBP reconstruction with 100 angular samples over 360 degrees.

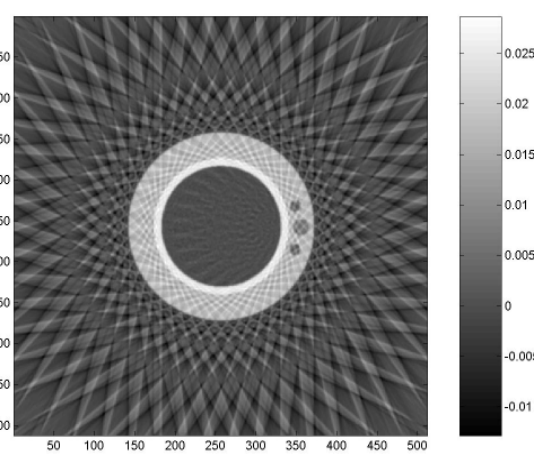


**Figure 21:** The FBP reconstruction with 50 angular samples over 360 degrees.

50 angles over 360 degrees and then perform FBP reconstruction with Hamming filter (cut-off frequency =0.8). From Figure 18 to Figure 21, spoke-like streak artifacts are evident with the decrease of the number of angular samples. Therefore, choosing an adequate number of projections is very important. The tradeoff is both scan time and reconstruction time.

### **3.3 Iterative Algorithms: Simultaneous Algebraic Reconstruction**

#### **Technique (SART)**

One popular iterative algorithm applied to solve linear systems is the algebraic reconstruction technique (ART) [Gordon et al., 1970], which was in fact the first

algorithm applied in CT. For this method, a projection (Equation 2) can be written as

$$g_i = \sum_{j=1}^{n^2} H_{ij} \mu_j \quad (10)$$

where  $H_{ij}$  is the system matrix that represents the contribution of pixel  $j$  to detector  $i$  and  $n^2$  is the number of pixel in the image  $n$  by  $n$ . Unlike most image-processing conventions, the pixels of the (square) system matrix are continuously numbered.

Therefore, Equation 10 contains only a single summation, albeit over all  $n^2$  pixels.

Equation 10 indicates that any ray passing through pixel  $j$  is attenuated by the average attenuation coefficient  $\mu_j$  in pixel  $j$  and is then measured by detector  $i$ . Unknown attenuation coefficients ( $\mu_j$ ) can be calculated from known projection values ( $g_i$ ) through the iterative application of Equation 11.

$$\mu_j^{k+1} = \mu_j^k + H_{ij} \left[ \frac{g_i - \sum_{j'=1}^{n^2} H_{ij'} \mu_{j'}^k}{\left( \sum_{j'=1}^{n^2} H_{ij'} \right)^2} \right] \quad (11)$$

Iterative algorithms outperform analytic algorithms in terms of reconstructed image quality, but they have not been used clinically due to the high computational demands and slow reconstruction time. The main reason for the slow computational speed lies in the necessity to compute the coefficients of the system matrix. These are purely determined by the geometry, but for  $i$  detectors and  $n^2$  pixels,  $n^2 i$  coefficients must

be computed for each iteration. In the example of  $n=512$  and  $i=512$ , more than 134 million coefficients need to be computed, and storing them after advance computation is impractical as this would require about 1/2 gigabyte of memory space. This is the primary reason why few studies use ART. To improve reconstruction speed, a modification of ART, called simultaneous ART (SART), was proposed in 1984 [Anderson and Kak, 1984]. The primary difference between ART and SART is that SART uses all sinogram data per backprojection. So, we can directly rewrite Equation 11 as

$$\mu_j^{k+1} = \mu_j^k + \frac{\lambda}{\sum_i H_{ij}} \sum_i H_{ij} \left[ \frac{(g_i - \sum_{j'}^{n^2} H_{ij'} \mu_{j'}^k)}{\sum_j H_{ij}} \right] \quad 12)$$

$\lambda$  is an underrelaxation factor, which can improve the reconstruction quality at the expense of convergence speed. However, SART still remains impractical if the image size or the full length of the object is large. To further reduce reconstruction time, one possible method is the well-known ordered subset (OS) method [Hudson and Larkin, 1994]. This method partitions the sinogram data into disjoint subsets and then uses the data in a single subset per backprojection. Wang and Jiang (2004) extended SART to OS-SART by applying ordered-subset projection at each sub-iteration. Therefore, Equation 12 can be rewritten as

$$\mu_j^{k,l+1} = \mu_j^{k,l} + \frac{\lambda}{\sum_{i \in l} H_{ij}} \sum_{i \in l} H_{ij} \left[ \frac{(g_i - \sum_{j'}^{n^2} H_{ij'} \mu_{j'}^{k,l})}{\sum_j H_{ij}} \right] \quad (13)$$

where  $l$  is the number of a subset. OS-type algorithms are popular because of an order-of-magnitude acceleration over simultaneous methods and simple implementation through a slight modification of the existing SART algorithm. Since OS-SART is one of the fastest iterative reconstruction techniques available, this method will be used in this study as the primary reconstruction algorithm and compared to FBP as the most established non-iterative reconstruction method.

In the following section, we will use a simple simulation to illustrate the performance of the OS-SART algorithm. Again, we use the digital phantom in the Figure 8 to produce a sinogram with 200 angles over 360 degrees (1.8 degree per angle) and then perform the ordered subset SART algorithm using 8 subsets with 1, 2, 4, 8, 12 and 16 iterations. From Figure 22 to Figure 27, we can observe that image resolution gradually improves with an increasing numbers of iterations. However, the choice of the number of iteration is still a challenging problem since it depends on several complex factors. One possible approach is to measure the difference between images from one iteration to the next. If the difference falls belows the predetermined value, we stop the updating equations.

Another problem is to choose the number of subsets. Generally, the number of subsets is approximately proportional to the degree of acceleration. However, the reconstruction image with a large number of subsets would be relatively noisy. Besides, SART combined with the OS method is not convergent and it may lead to a limited cycle. One possible approach for making OS-type algorithms convergent is relaxation, ie., using

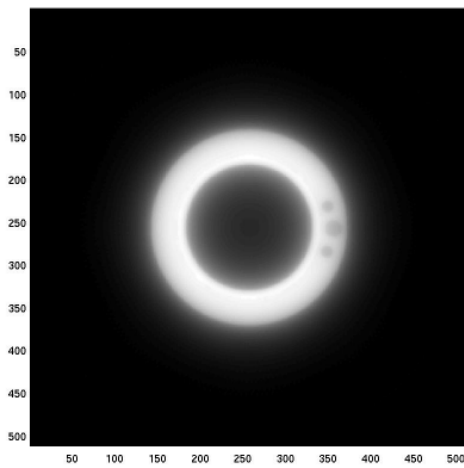


**Figure 22:** The OS-SART reconstruction using 8 subsets with 1 iteration.

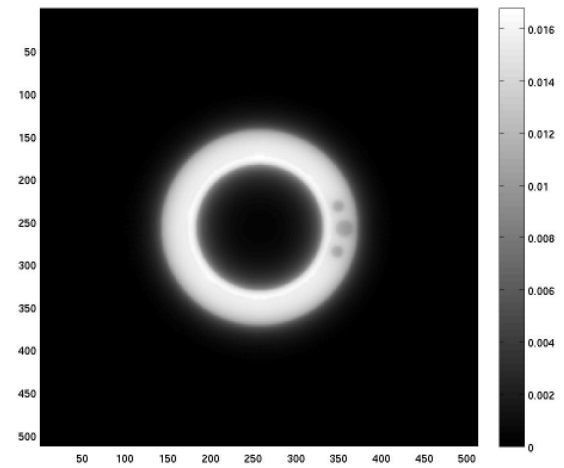


**Figure 23:** The OS-SART reconstruction using 8 subsets with 2 iterations.

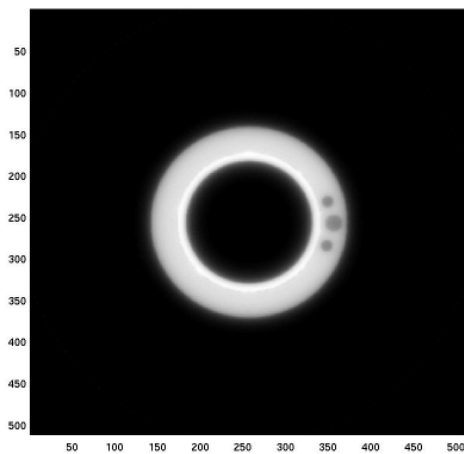


**Figure 24:** The OS-SART reconstruction using 8 subsets with 4 iterations.

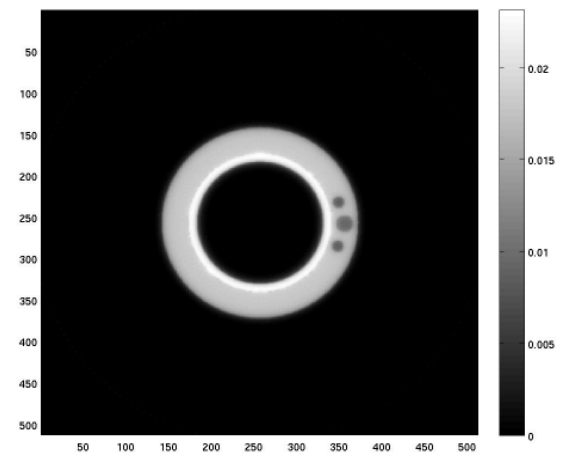


**Figure 25:** The OS-SART reconstruction using 8 subsets with 8 iterations.

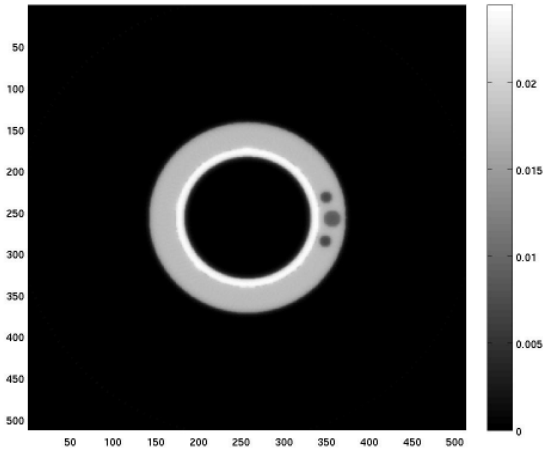


**Figure 26:** The OS-SART reconstruction using 8 subsets with 12 iterations.

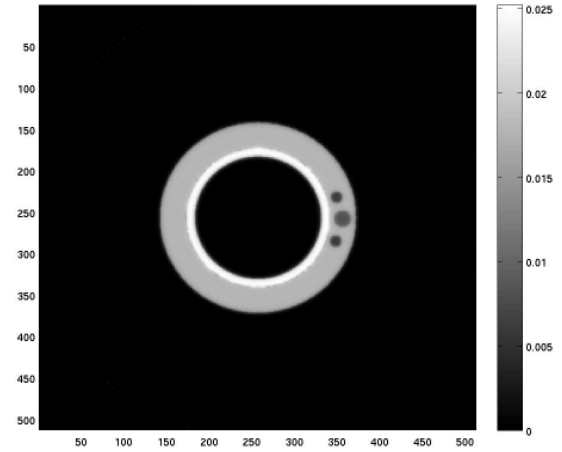


**Figure 27:** The OS-SART reconstruction using 8 subsets with 16 iterations.

diminishing stepsizes [Ahn et al., 2003]. The other well-known approach without a use-determined relaxation parameter is to use a notation of a complete data as well as ordered subsets. These algorithms are described in [Hsiao et al., 2002]. The other important factor affecting the reconstruction time is the construction of the system matrix ( $H_{ij}$ ) because it affects the computational time of forward and backward projections. In the next paragraph, we will introduce the basic idea of building a system matrix ( $H_{ij}$ ) much more efficiently. Besides, we will modify a powerful simulation tool [Lee, 1996], which is originally used in emission computed tomography and transmission computed tomography for reducing further reconstruction time in this thesis.

### 3.4 Construction of the System Matrix

As we mentioned before, we extend the simulation tool [Lee, 1996] to our OT system and reduce further the computation time needed to build a system matrix. The system matrix of this simulation tool is based on a method proposed by Siddon (1985). Siddon's method inputs values of the angle ( $\theta$ ) and the detector ( $t$ ) and then returns the position of all pixels ( $i, j$ ) along the ray ( $t, \theta$ ) and the chord length of the ray through the pixel ( $i, j$ ). The geometry of calculating these indexes can be described in Figure 28. At

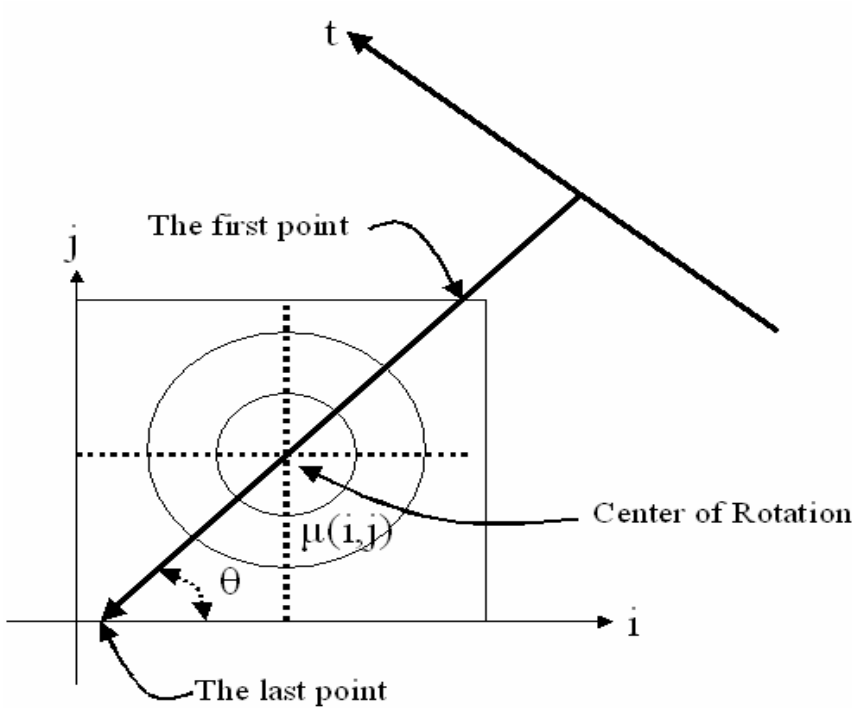


**Figure 28:** The geometry of calculating chord lengths per pixel in Siddon's method.

first, we can calculate the first point entering the image and the last point leaving the image for each angle ( $\theta$ ) and detector ( $t$ ). Then, we can record each

subsequent pixel ( $i, j$ ) along the ray and calculate its chord length using Siddon's method

up to the last point. However, this method is still inefficient if this procedure is repeated at each iteration. One feasible approach to avoid this problem is to build a look-up table. Each ray used for forward or backward projection is represented by its angle ( $\theta$ ) and detector ( $t$ ), and is the line perpendicular to the detector array and emitted from the detector array ( $t$ ). Once the look-up table is built up, the pixel ( $i, j$ ), which is passed by a ray ( $t, \theta$ ), and its chord lengths can be obtained from this table without the need for recalculation at each iteration. Unfortunately, it is a time-consuming process to calculate the precomputed system matrix if there are many detectors ( $t$ ) and angles ( $\theta$ ). As mentioned before, the memory requirement for the precomputed system matrix is quite enormous. One workable method is to use the after-mentioned rotation-based projection. Originally, a detector array is rotated (the object is fixed) and then we calculate the system matrix at the angle. Conversely, we can rotate the object with a fixed detector array. This indicates that we only store the system matrix at the first angle. Thus, the process for the forward projection is to rotate the object with angle ( $\theta$ ) and then perform forward projection. Conversely, the process for the backward projection is to perform backward projection and then rotate the object with negative angle ( $-\theta$ ). Although image rotation takes some time, this computational time is very small compared to the

original method. Therefore, we need only use the system matrix of the first angle to perform forward and backward projections. This method can largely reduce the computational time and the memory usage for storing the system matrix.

One potential drawback of using rotation-based projection may result in a slight loss of resolution. This artifact relates to rotation methods. Generally, there are three common rotation methods: the nearest neighbor, bilinear interpolation and bicubic interpolation. Based on our preliminary studies, the nearest neighbor method is the fastest, but the accuracy is insufficient. The bilinear interpolation and bicubic interpolation both can provide better image resolution than the nearest neighbor, but the computational time using bicubic interpolation is longer than that using bilinear interpolation. Under the consideration of speed and accuracy, we will use bilinear interpolation in the reconstruction process.

To evaluate the accuracy of the rotation-based method, we created a two-dimensional phantom ( $128 \times 128$ ) shown in Figure 29 and used a simulation tool [Lee, 1996] to generate a noiseless sinogram (the number of bins: 128 and the number of angles over  $360^\circ$  angle: 200). Then we compared the reconstruction image of using the traditional method (non-rotated method) with that of using rotation-based method. Figure

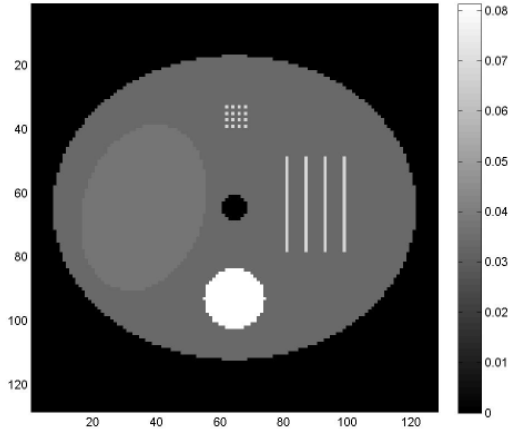


**Figure 29:** The two-dimensional digital phantom (true image).

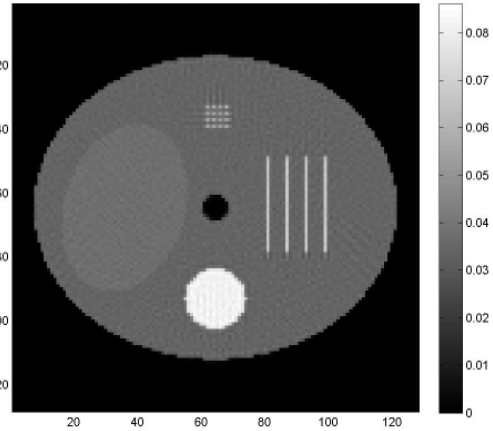


**Figure 30:** The reconstruction image uses the traditional method (non-rotated method).

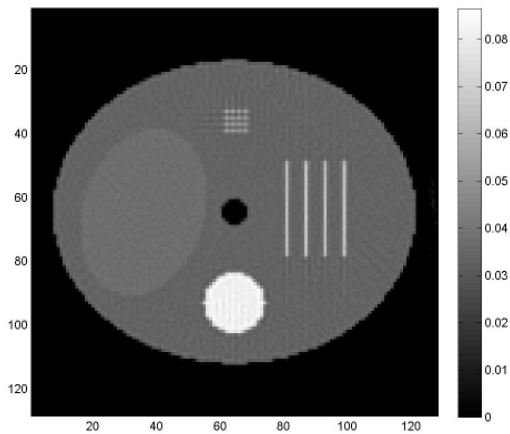


**Figure 31:** The reconstruction image uses the rotation-based method.

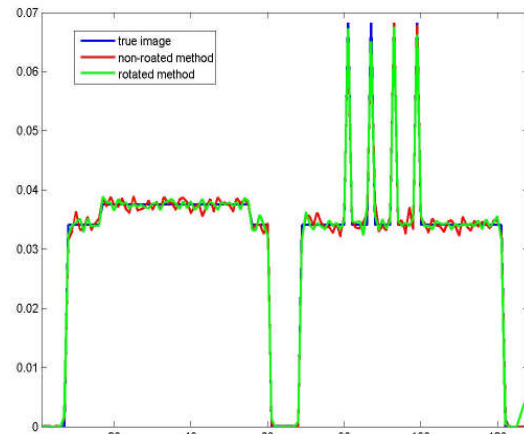


**Figure 32:** The horizontal image profile of Figure 29 (blue line), 30 (red line) and 31 (green line) along the central row.

30 is the reconstruction image using the traditional method and Figure 31 is the reconstruction image using the rotation-based method. The reconstruction algorithm is OS-SART with 10 subsets and 40 iterations. Visually, we can find the difference of the reconstruction image between the traditional method and the rotation-based method is almost indistinguishable. Figure 32 is the horizontal profile of Figure 29 (blue line), 30

(red line) and 31 (green line) along the central row. Since the difference of the intensity between two methods is also small, we can use the rotation-based method to reduce the memory of storing the system matrix and the reconstruction time. A detail comparison can be found in [Di Bella, 1996].

## CHAPTER 4

### EXPERIMENTS AND RESULTS

#### 4.1 Basis for the First Phantom Study

Before actually testing real tissue samples, the system with its new reconstruction methods was to be tested using different phantom objects that somewhat resemble the

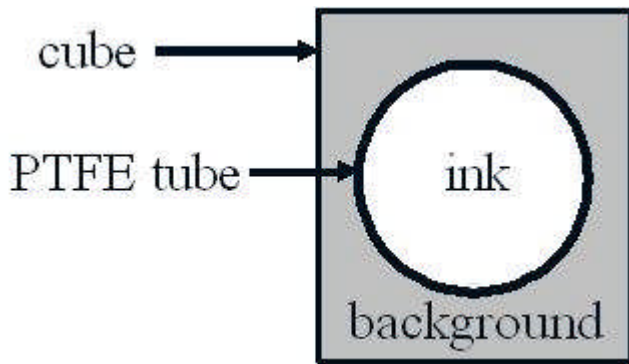


**Figure 33:** The configuration of the first phantom. The PTFE tube is immersed in a transparent sample bath. The solution inside the tube is ink with water. The solution outside the tube is water (background).

TEBV. In this thesis, we used two phantoms to study the performance of our OT system. The two phantoms were primarily designed to evaluate the accuracy of total attenuation coefficients and the shape of

phantoms. Figure 33 shows the configuration of the first phantom. The PTFE (Teflon) tube, which was kindly provided by Zeus Industrial Products, Inc., was immersed in a transparent cube. The inner diameter of the PTFE tube was 3.38 mm and the thickness of the PTFE tube was 0.20 mm. The solution inside the PTFE tube was black ink diluted with water and the solution outside the PTFE tube was water (background). One end of

the PTFE tube was sealed by glue. The other was inserted into a metal shaft, which was responsible for rotating the PTFE tube. Six different ink concentrations were tested in this experiment, and the attenuation coefficients obtained from our OT system were compared with those obtained from a spectrophotometer. However, the mismatch of refractive index between the PTFE tube and water is large. This mismatch will result in many refracted photons, particularly those refracted at the edges of the phantom. Since the spatial filter blocks most off-axis photons, the intensity of the projection in these regions is close to zero. The missing data will cause inaccurate attenuation coefficients. One feasible way to avoid this artifact is to reduce the mismatch of refractive index.

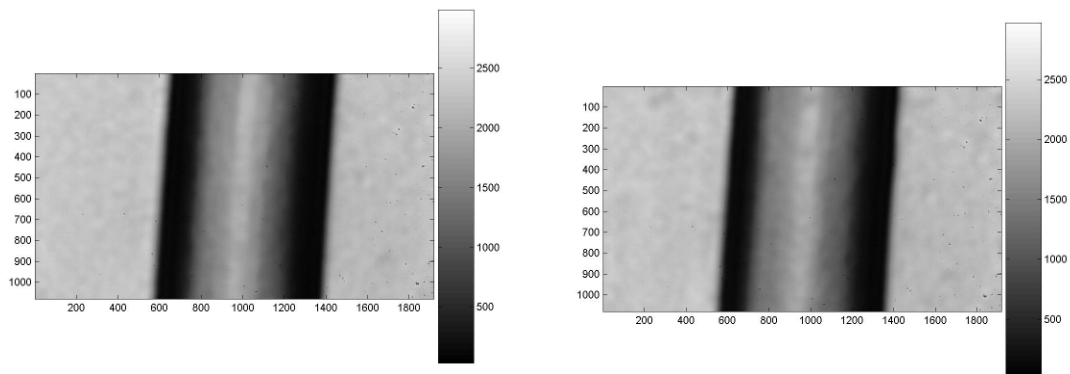


**Figure 34:** The projection of the PTFE tube with 100 mL water and 0 g (left) and 1 g sucrose (right).

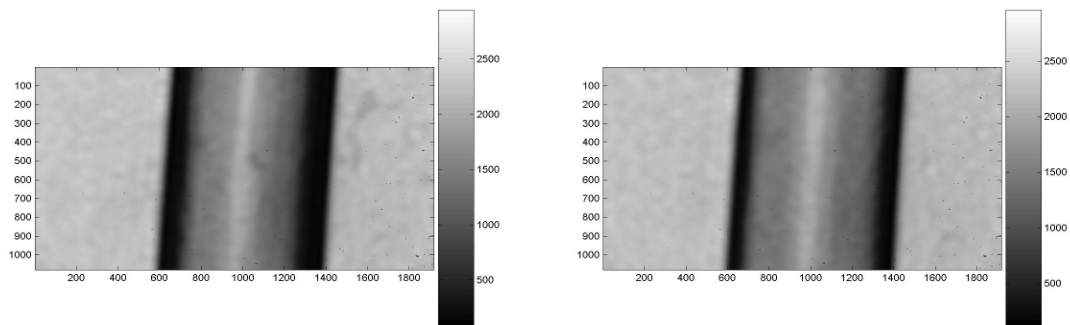


**Figure 35:** The projection of the PTFE tube with 100 mL water and 2 g (left) and 3 g sucrose (right)

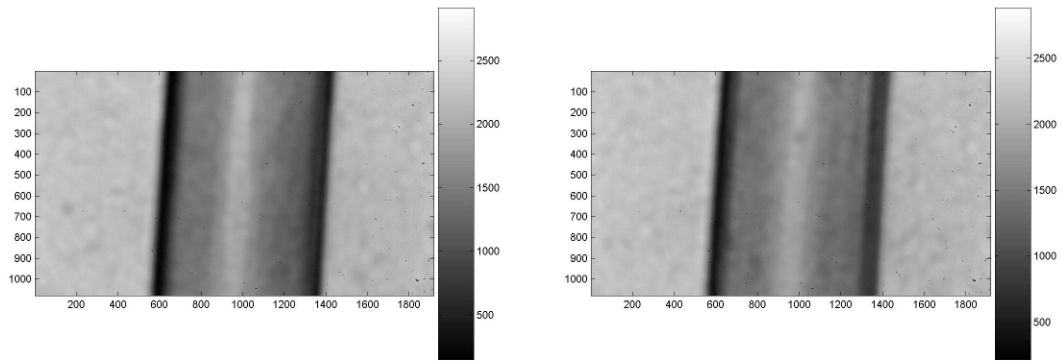


**Figure 36:** The projection of the PTFE tube with 100 mL water and 3.4 g (left) and 3.6 g sucrose (right)

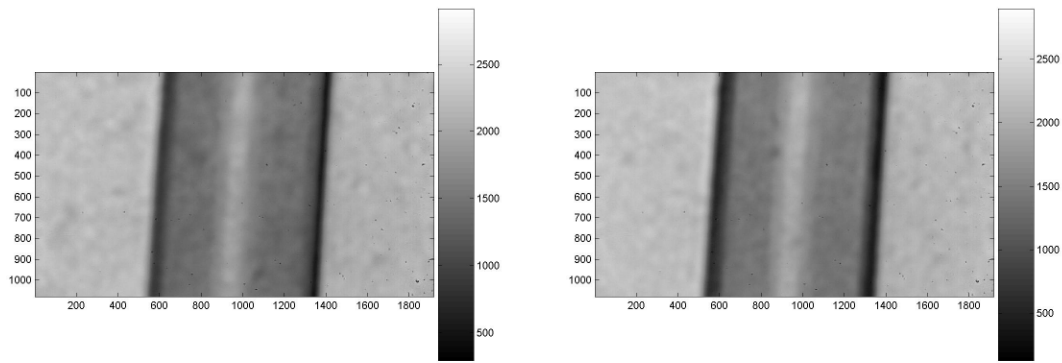


**Figure 37:** The projection of the PTFE tube with 100 mL water and 3.8 g (left) and 4 g sucrose (right)

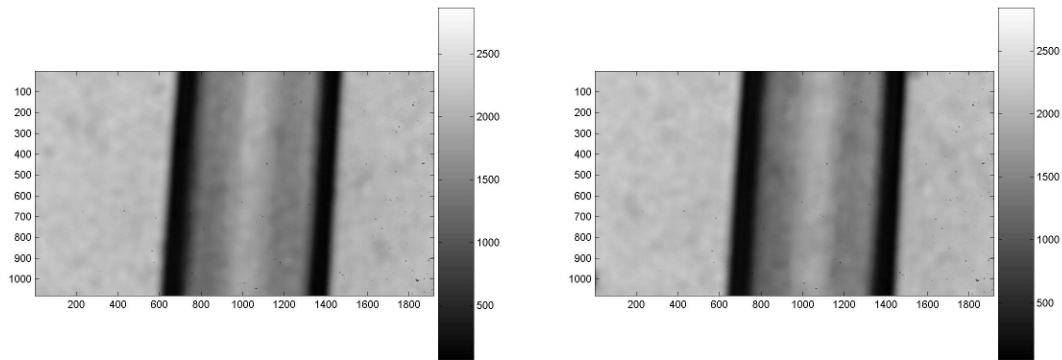


**Figure 38:** The projection of the PTFE tube with 100 mL water and 4.2 g (left) and 4.4 g sucrose (right)

In this thesis, we used sucrose to increase the refractive index of the solution to match the PTFE phantom. By scanning the PTFE tube with different concentrations, we were

able to find the concentration where the mismatch of refractive index was minimized.

The solution inside and outside the PTFE tube is 100 mL water and different concentrations of sucrose. Figure 34 (left) is the projection at the first angle. The horizontal axis is the number of the detector and the vertical axis is the number of the slice in z (axial) direction. At 0% sucrose (Figure 34, left), the refractive region is more than 20% of the total width. From Figure 34 to Figure 35, we can find that the refractive region is decreased with the increase of sucrose concentration. This indicates that the mismatch of refractive index between background and the PTFE tube is reduced. As becomes evident from Figure 36 to Figure 38, the smallest region affected by strong refraction can be achieved if we use 3.8% sucrose. Therefore, we use 3.8% sucrose as background in this experiment, and the solution inside the PTFE tube will 3.8% sucrose with ink in all subsequent experiments. Since ink concentration is low, we assume that the influence of the ink on refractive index can be neglected.

## **4.2 Pre-processing before Image Reconstruction**

Figure 39 shows the profile of projection at the first angle. There was no ink inside the PTFE tube. The solution inside and outside the PTFE tube was 3.8% sucrose. Near the edge of the PTFE tube, most scattered photons were blocked by the spatial filter due

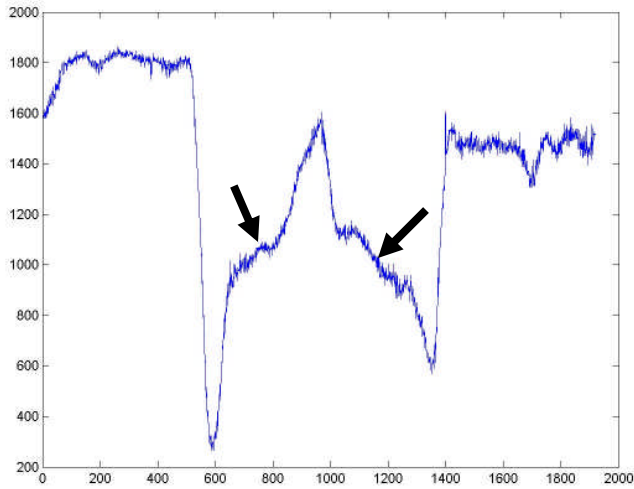


**Figure 39:** The profile of the projection at the first angle. The solution inside and outside the PTFE tube is 3.8% sucrose.

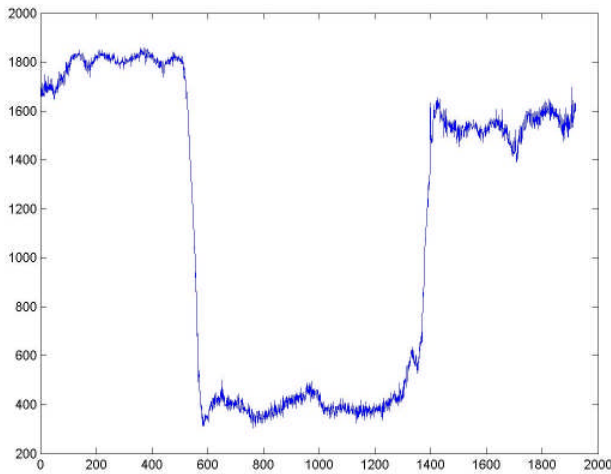


**Figure 40:** The profile of the projection at the first angle. The solution inside the PTFE tube is 3.8% sucrose with ink. The solution outside the PTFE tube is 3.8% sucrose.

accurate adjustment is very difficult. Another possible explanation for the sharp peak in the center of the projection is a double reflection between the sample bath and the object

to large refractive angles. As a result, the intensity in these regions was lower than warranted by the tube's attenuation. For the region between center and edge (arrow), the intensity was therefore underestimated. This phenomenon indicates that photons near the edge are rejected by the spatial filter. Theoretically, the intensity in this region should be the same as that in the center if the spatial filter is in the focal plane. One possible reason is that the spatial filter is not in the focal plane. However,

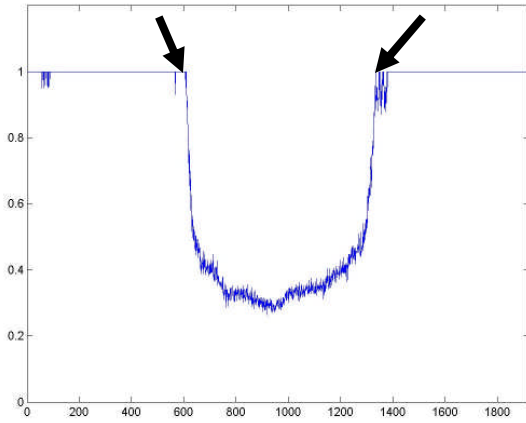


**Figure 41:** The profile of the projection data ( $g_{\theta}$ ) at the first angle.

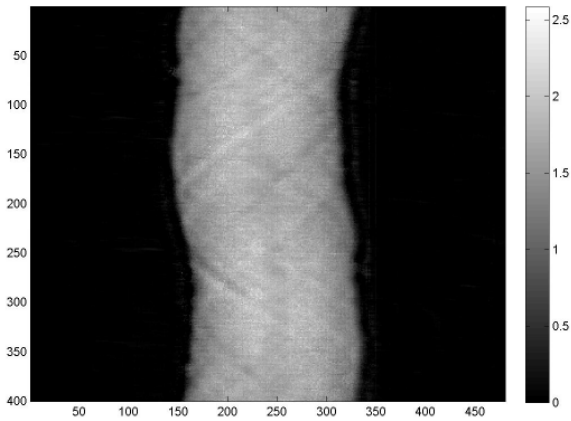


**Figure 42:** The sinogram, which is composed of the projection data ( $g_{\theta}$ ) angle by angle.

when it is parallel to the both side. If we used the scan without the PTFE tube as blank scan ( $I_0$ ), the intensity of the projection between center and edge was underestimated.

One simple method to avoid this problem is to use Figure 39 as a blank scan ( $I_0$ ). Figure 40 shows the profile of the projection at the first angle. The solution inside the PTFE tube was 3.8 % sucrose with a very high ink concentration. The solution outside the PTFE tube was 3.8%

sucrose. The only difference between Figure 39 and Figure 40 is the attenuation

of the ink. It means that the attenuation due to the PTFE tube would be removed and the underestimated intensity between center and edge is unaffected. It is likely that the ink concentration is high enough to absorb the double-reflection, so that central peak no long

appears in Figure 40. According to Equation 2, the projection data ( $g_\theta$ ) can be calculated from Figure 39 and Figure 40. Figure 41 is the projection data ( $g_\theta$ ) at the first angle ( $\theta=0$ ). However, some pixel values at the edge (arrow) are larger than 1. It means that attenuated intensity ( $I$ ) is larger than unattenuated intensity ( $I_0$ ). This is theoretically impossible. The possible reason is the interference of noise. In order to reduce the effect of noise, any pixel value that is larger than 0.96 was set to 1. At the edge of the tube, most light rays were blocked by the spatial filter due to large refractive angles. Thus, the ratio of Figures 39 and 40 in the region is almost 1. This indicates that the signal in the region is still unknown, and the missing data will lead to inaccurate attenuation coefficients.

If we use Figure 39 as a blank scan ( $I_0$ ), two scans: the PTFE tube without ( $I_0$ : pre-scan) and with ink ( $I$ : post-scan) per acquisition are necessary for image reconstruction. One serious problem is the shift of position between pre-scan and

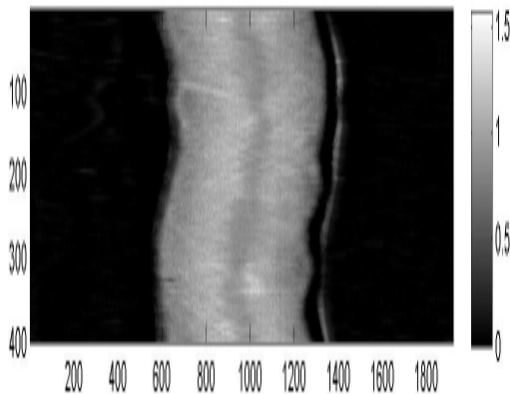


**Figure 43:** The sinogram without the correction of registration.

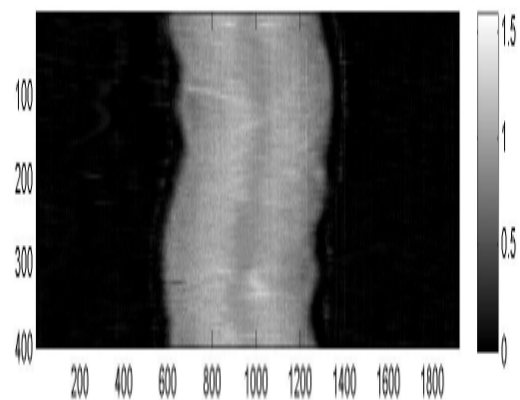


**Figure 44:** The sinogram with the correction of registration.

post-scan. For example, Figures 43 and 44 show the sinograms without and with the correction of registration. We can find that Figure 43 has an artifact (arrow) in the edge of the sinogram as compared to Figure 44.

Figure 45 is the reconstruction image of Figure 43 and Figure 46 is the reconstruction image of Figure 44. To reduce the image reconstruction time, we reduced the number of bin from 1920 to 480 by using bilinear interpolation. The reconstruction was performed

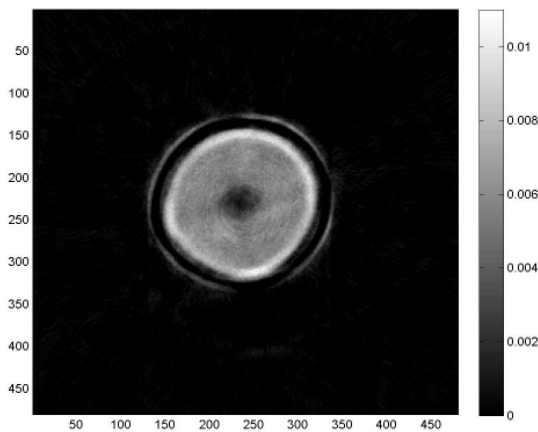


**Figure 45:** The image reconstruction using FBP algorithm without the correction of registration.

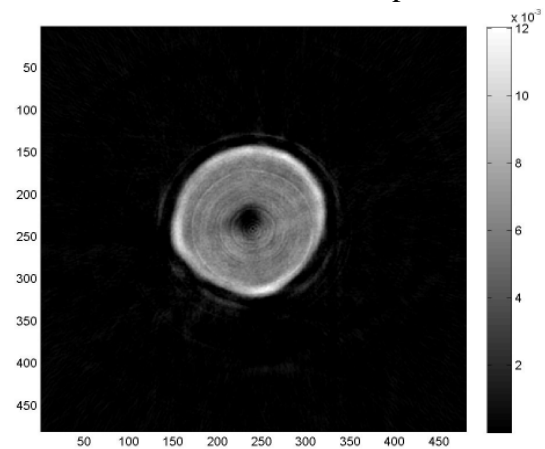


**Figure 46:** The image reconstruction using FBP algorithm with the correction of registration

using the FBP algorithm with Hamming filter and 0.9 cut-off frequency. As opposed to Figure 46, Figure 45 has an obvious ring (arrow) outside the object. Clearly, incorrect registration will result in ring artifacts. In Figure 46, we observe that there are additional rings inside the object. The primary reason is the interference of dust in the surface of the detector. If there was no correction for registration between two scans, the effect of dust

would be cancelled. This is because the interference of dust is still in the same location.

Conversely, the effect of dust can not be cancelled if we perform registration. In fact, we can find several vertical lines in Figure 44 after performing the registration of two scans.

In the new OT system, the center of rotation (COR) should be the same as the center of the detector array. If there is slight mismatch between the two centers, the reconstruction image would be distorted. One simple method is to shift the sinogram pixel by pixel until the distortion disappears. For example, Figure 47 is the reconstruction image without the correction of COR. It is easy to observe a blurring effect along the boundary of the object. Figure 48 is the reconstruction image after the correction of COR. Compared with Figure 47, the blurring effect in Figure 48 evidently improved. The other

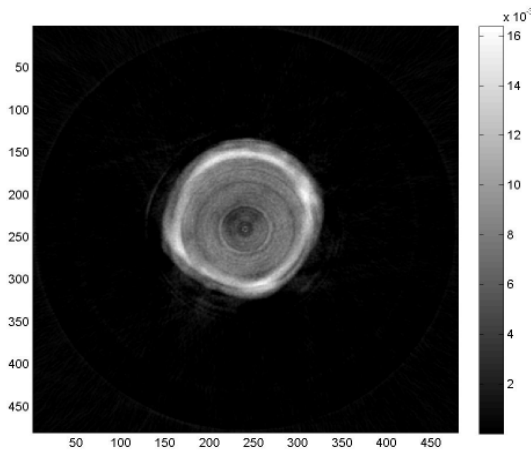


**Figure 47:** The reconstruction image using the FBP algorithm without the correction of COR.

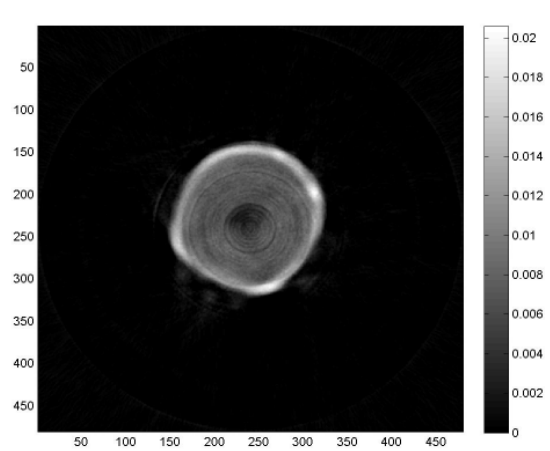


**Figure 48:** The reconstruction image using FBP the algorithm with the correction of COR.

method is to adjust the position of the COR with the translation stage if we know the

difference between the position of the COR and the position of the detector.

### 4.3 Results of the First Phantom Study

As mentioned before, six different concentrations were tested in this experiment and then attenuation coefficients obtained from the new OT system with those obtained from the spectrophotometer were compared. The projection data in this experiment is 1920 bins with 400 angles over  $360^{\circ}$  ( $0.9^{\circ}$  per angular step). To reduce the reconstruction time, we reduced the number of bins from 1920 to 480 by using bilinear interpolation. The reconstruction process used the OS-type SART algorithm with 20 subsets and 20 iterations. For visual comparison, the reconstruction images (270<sup>th</sup> slice) were post-smoothed with a Gaussian filter (FWHM = 3 pixel and  $5 \times 5$  matrix). The

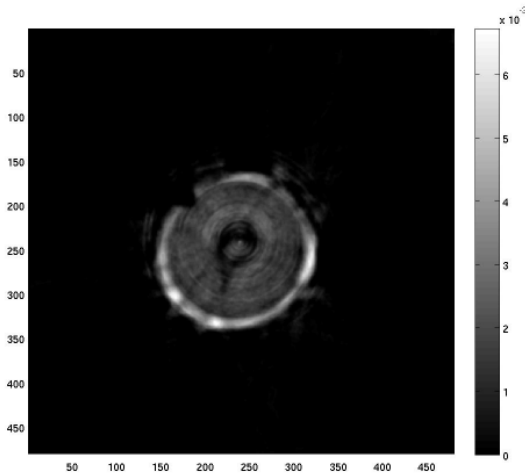


**Figure 49:** The reconstruction image (ink1) using the OS-type SART algorithm with 20 subsets and 20 iterations.

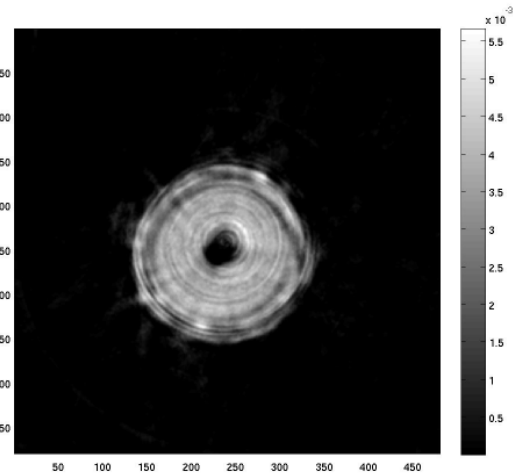


**Figure 50:** The reconstruction image (ink2) using the OS-type SART algorithm with 20 subsets and 20 iterations.

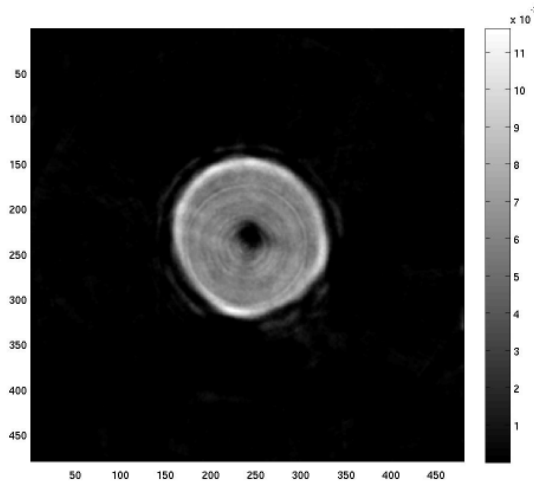


**Figure 51:** The reconstruction image (ink3) using the OS-type SART algorithm with 20 subsets and 20 iterations.

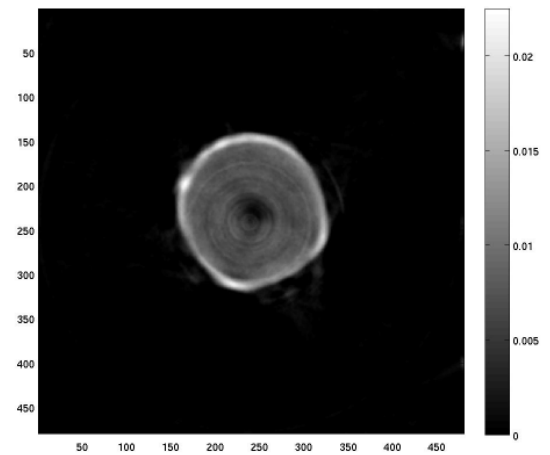


**Figure 52:** The reconstruction image (ink4) using the OS-type SART algorithm with 20 subsets and 20 iterations.

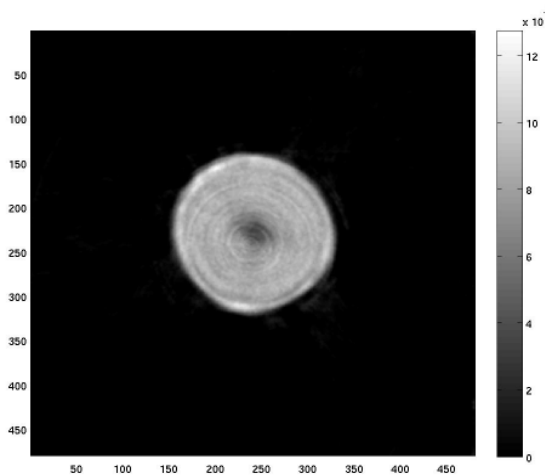


**Figure 53:** The reconstruction image (ink5) using the OS-type SART algorithm with 20 subsets and 20 iterations.

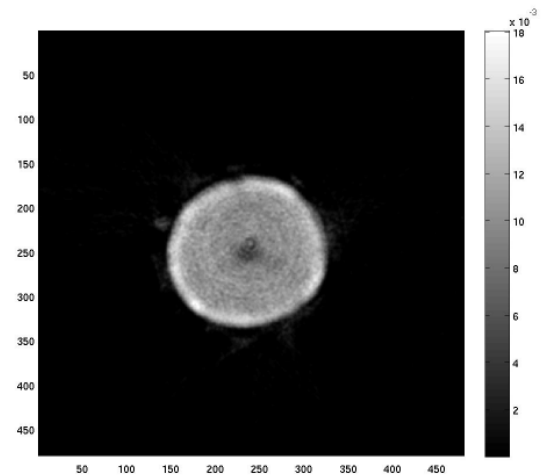


**Figure 54:** The reconstruction image (ink6) using the OS-type SART algorithm with 20 subsets and 20 iterations.

concentration of ink increases from Figure 49 (ink1) to Figure 54 (ink6). Figures 50, 51, 52 and 53 are ink2, ink3, ink4 and ink5. As can be seen, the quality of the reconstruction image degrades with the decrease of ink's concentration. Because the contrast in a low

ink concentration is poor, the reconstruction image is more easily affected by factors such as noise, micro-bubbles, dust and the mismatch of position between pre-scan and post-scan.

In addition, total attenuation coefficients in the center of the tube are underestimated by the effect we have earlier identified as a possible double-reflection between the center of the tube and the walls of the sample bath. From Figure 49 to Figure 54, the

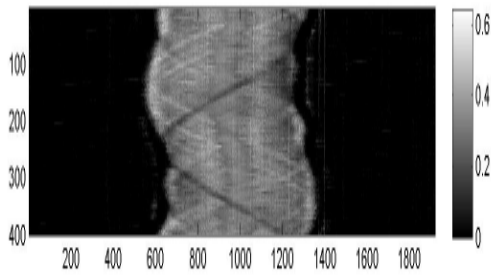


**Figure 55:** The sinogram of Figure 43.

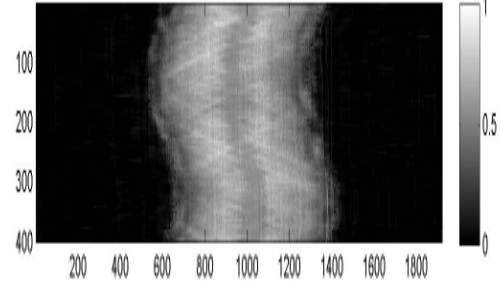


**Figure 56:** The sinogram of Figure 44.

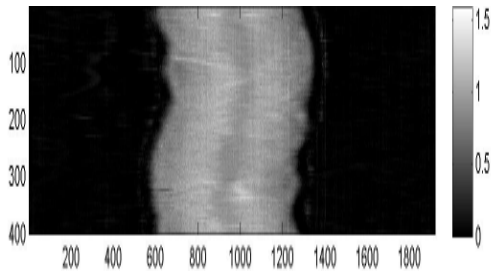


**Figure 57:** The sinogram of Figure 45.

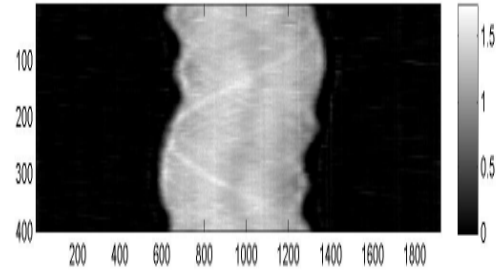


**Figure 58:** The sinogram of Figure 46.

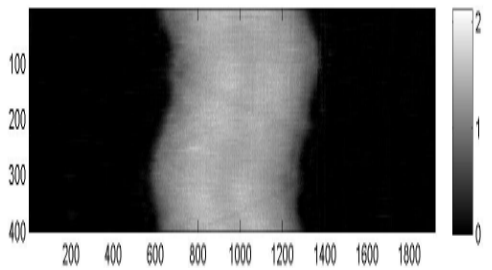


**Figure 59:** The sinogram of Figure 47.

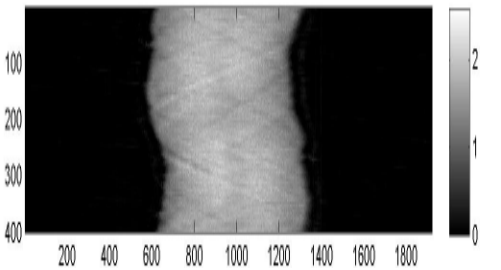


**Figure 60:** The sinogram of Figure 48.

underestimation of total attenuation coefficients is more pronounced with lower ink concentration. The other possible reason for this effect is that the mismatch of the refractive index between solution and PTFE tube causes specular reflection. When we scan the PTFE tube without ink (pre-scan), some light is reflected back to original direction. However, parts of light do not undergo specular reflection as we scan the PTFE tube with ink (post-scan). On the other hand, the light would be attenuated by ink or collected by detectors. This indicates that detectors may collect additional signal in the post-scan ( $I$ ). As a result, the attenuation coefficient is underestimated. The artifact is more obvious at lower ink concentrations since the probability of collecting extra light is higher than that of attenuating light in low ink's concentration. The artifact also can be found in the projection data ( $g_\theta$ ). For example, we can observe that lower intensity in the center of sinogram gradually becomes more apparent from Figure 55 to Figure 60.

Attenuation coefficients	Spectrophotometer	OT system	Recovery
Ink 6	0.0123	0.0104	84.55 %
Ink 5	0.0101	0.0086	85.15 %
Ink 4	0.0092	0.0072	78.26 %
Ink 3	0.0069	0.0060	86.96 %
Ink 2	0.0052	0.0038	73.08 %
Ink 1	0.0032	0.0017	53.13 %

**Table 1:** The attenuation coefficient measured from our OT system and spectrophotometer in different ink's concentrations.

To evaluate the accuracy of attenuation coefficients, we measured the attenuation

coefficient obtained from our OT system and compared with the measured attenuation coefficient obtained from a spectrophotometer. To obtain the standard attenuation coefficient, we put the solution with ink inside a transparent cuvette (optical path length: 1cm). By using the spectrometer, we can obtain the absorbance of the solution. From the known thickness and absorbance, the attenuation coefficient at different wavelengths can be calculated. In this experiment, we use the attenuation coefficient at 625nm as the standard value. Table 1 lists the attenuation coefficient obtained (unit: 1/pixel) from our OT system and spectrophotometer in different ink concentrations. Recovery is defined as

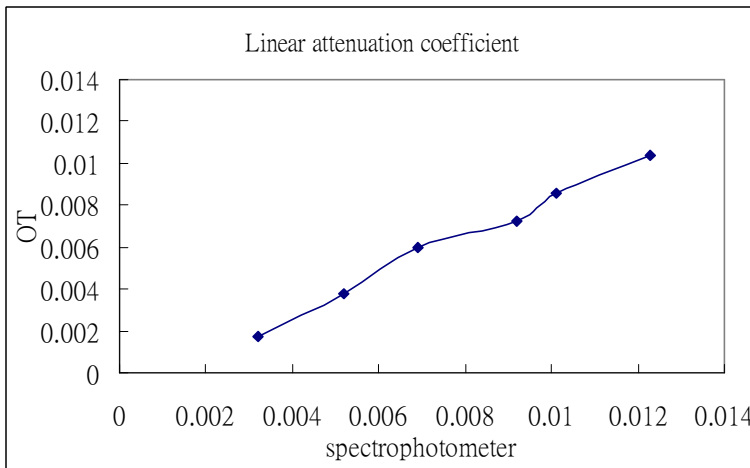


**Figure 61:** The relation of attenuation coefficients between our OT system and spectrophotometer.

the ratio of these two attenuation coefficients. In Table 1, we can see that the best recovery is about 86%.

This means that the OT

system underestimates the

attenuation coefficient. The primary reasons are specular reflection and the elimination of signal in refractive regions [Haidekker, 2005]. The recovery was even further reduced with the decrease of ink concentration, especially in the lowest concentration. Figure 61

shows the relation of attenuation coefficients between the new OT system and spectrophotometer in six different ink's concentrations. The correlation between them is very high with a R-squared value of about 0.99. The result shows that the new OT system can be applied to a wide range of absorption coefficients although there is a clear underestimation of the  $\mu$  values. Table 2 shows the measured radius in different ink concentrations. The theoretical inner radius of the PTFE tube is 84.5 pixels. To evaluate the accuracy of measured radius, we define a linearly weighted error as:

$$\text{weighted error} = \frac{|\text{measured radius} - \text{theoretical radius}|}{\text{theoretical radius}} \times 100\% \quad (14)$$

Radius (unit: pixel)	OT system	weighted error
Ink 6	87.97	0.04
Ink 5	87.12	0.03
Ink 4	86.84	0.03
Ink 3	86.29	0.02
Ink 2	99.51	0.18
Ink 1	86.09	0.02

**Table 2:** The accuracy of measured radius in different ink's concentration.

At first, we obtained a region of interest (ROI) in the reconstruction image by using image segmentation and then calculated the number of pixel inside the ROI (area). Finally, we can calculate the measured average radius ( $area = \pi r^2$ ) where the assumption that the PTFE tube is approximately a circle. The PTFE tube was distorted slightly during the process of production and is therefore not a fully circular. One alternative way is to

compare the area. The area would not be affected by the distortion since the area inside the PTFE tube is not dependent on circularity. Since the difference between two measurements is very small, we can use the measured radius to evaluate the accuracy of our OT system. In Table 2, weighted errors were less than 5% except ink 2. The result indirectly demonstrates that the new OT system can provide accurate reconstruction of the object's geometry.

#### 4.4 Basis for the Second Phantom Study

The purpose of the first phantom study was to investigate the performance of our OT system. The results show that our OT system can scan a wide range of attenuation

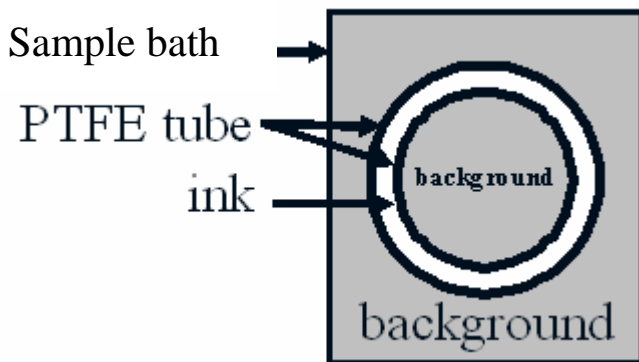


**Figure 62:** The configuration of the second phantom. The solution between the PTFE tubes is ink with water. The solution outside the outer PTFE tube and inside the inner PTFE tube is water (background).

the second phantom is designed to more accurately simulate the geometry of a blood

vessel. Figure 62 shows the configuration of the second phantom. The inner diameter of

coefficients. In addition, it can provide good spatial resolution and accurate reconstruction of the exterior shape. However, the cross-section of a true blood vessel is a ring rather than a circle. Therefore,

the inner PTFE tube is 3.38 mm and its thickness is 0.20 mm. The inner diameter of the outer PTFE tube is 4.72 mm inner diameter with 0.25 mm thickness. The solution between two PTFE tubes is ink and water with 3.8% sucrose. The solution inside the inner PTFE tube and outside the outer PTFE tube is water with sucrose (background). In the double-tube experiment, the effect of refractive index mismatch is different from the first phantom. Therefore, the determination of the optimum sucrose concentration had to be changed.

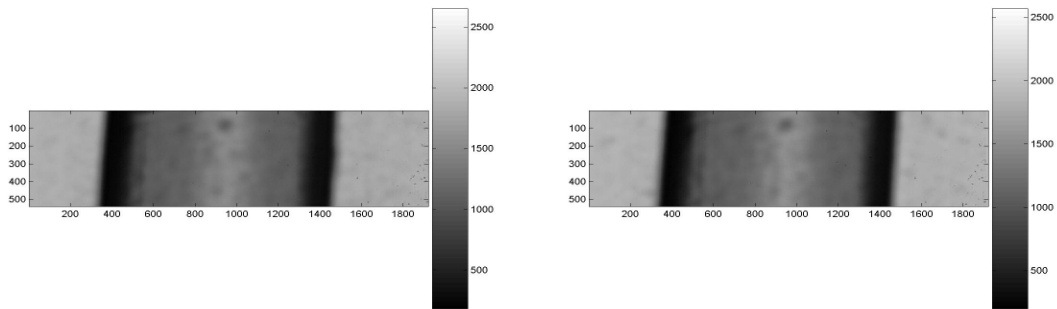


**Figure 63:** The projection of the PTFE tube with 100 mL water and 3.8 g (left) and 4.0 g sucrose (right)

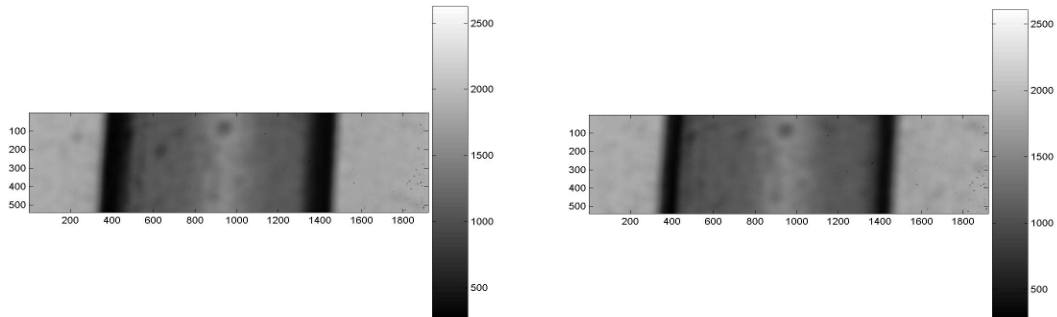


**Figure 64:** The projection of the PTFE tube with 100 mL water and 4.2 g (left) and 4.4 g sucrose (right)

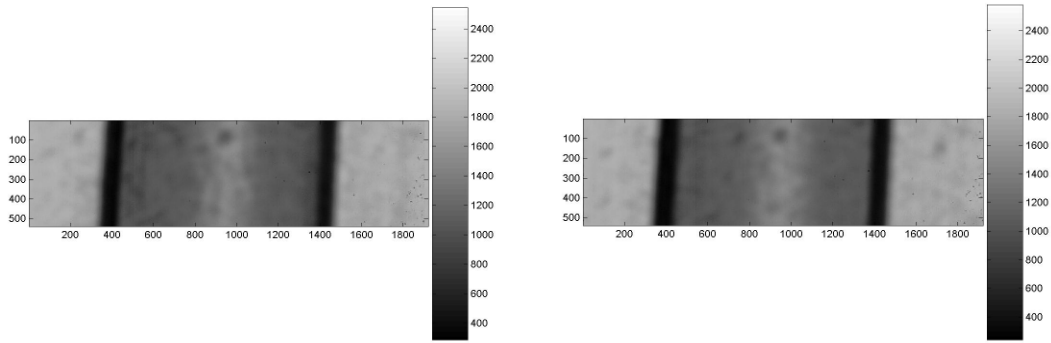


**Figure 65:** The projection of the PTFE tube with 100 mL water and 4.6 g (left) and 4.8 g sucrose (right)

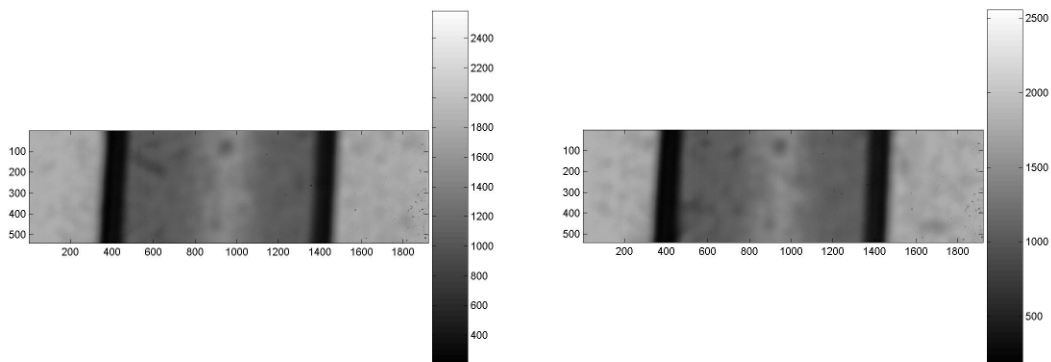


**Figure 66:** The projection of the PTFE tube with 100 mL water and 5.0 g (left) and 5.2 g sucrose (right)

To find an appropriate concentration of sucrose, we scanned the outer PTFE tube alone. The solution inside and outside the PTFE tube is water with sucrose. Figure 63 depicts the projection of the outer PTFE tube with 3.8% sucrose (left) and 4.0% sucrose (right). Figure 64 shows the projection of the outer PTFE tube with 4.2% sucrose (left) and 4.4% sucrose (right), and Figure 65 shows the projection of the outer PTFE tube with 4.6% sucrose (left) and 4.8% sucrose (right). Figure 66 shows the projection of the outer PTFE tube with 5.0% sucrose (left) and 5.2% sucrose (right). With the increase of concentration,

refractive regions are reduced gradually. Based on our evaluations, the concentration between 4.4% and 4.6% is the minimum refractive regions. However, 4.6% sucrose results in larger refractive regions for the inner PTFE tube. Therefore, we determined that 4.5% sucrose in the second experiment would lead to minimal refraction from both tubes.

### 4.5 Results of the Second Phantom Study

Like the first phantom, the registration between pre-scan and post-scan in the second phantom is important. In addition, the correction of COR is necessary. For example,

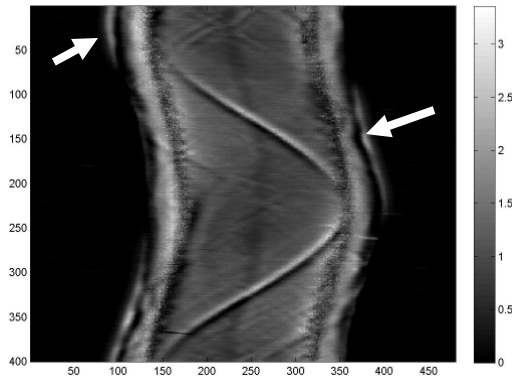


**Figure 67:** The sinogram of 270<sup>th</sup> slice without corrections of registration and COR.

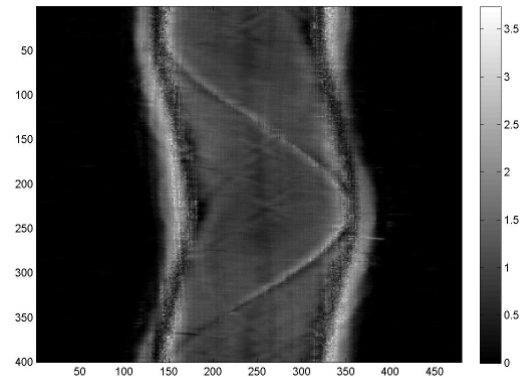


**Figure 68:** The sinogram of 270<sup>th</sup> slice with corrections of registration and COR.

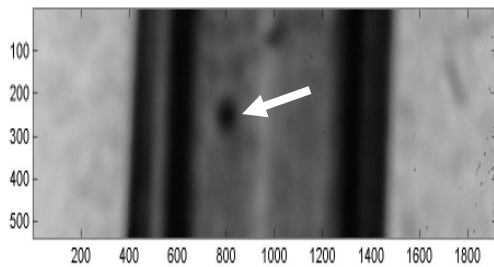


**Figure 69:** The projection of the second phantom without ink between two PTFE tubes at 100<sup>th</sup> angles.

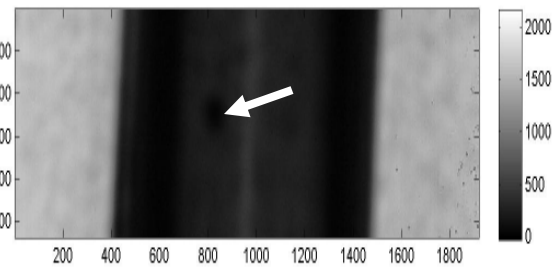


**Figure 70:** The projection of the second phantom with ink between two PTFE tubes at 100<sup>th</sup> angles.

Figure 67 shows the sinogram of 270<sup>th</sup> slice without corrections of registration and COR.

We can observe the misregistration of two scans (arrow) in the edge of the sinogram.

Figure 68 shows the sinogram after performing corrections of registration and COR. In

Figure 68, the underestimation of attenuation coefficients is still existent in the center of

sinogram. Besides, the interference of particles affects reconstruction images. For

example, Figures 69 and 70 show projection data of the second phantom without and

with the presence of ink between the two PTFE tubes at 100<sup>th</sup> angles. There is a low

intensity (arrow) in the projection between 200<sup>th</sup> slice and 300<sup>th</sup> slice. This is the

interference of an air bubble or dust. Sequentially, there is a dark and a bright curve in

Figures 67 and 68. Figure 71 shows the reconstruction image of the sinogram (Figure 67)

without corrections of registration and COR. The reconstruction algorithm was the

OS-type SART with 20 subsets and 20 iterations. For visual comparison, reconstruction

images (270<sup>th</sup> slice) were post-smoothed with a Gaussian filter (FWHM = 3 pixel and

5×5 matrix). After performing corrections of registration and COR, there is no shadow

near the boundary of the object in Figure 68. Furthermore, the blurring effect in Figure 72

is less than that in Figure 71. The bright spot (arrow) in Figures 71 and 72 is the

contamination of a bubble or dust. Figure 73 is the reconstruction image of 150<sup>th</sup> slice.

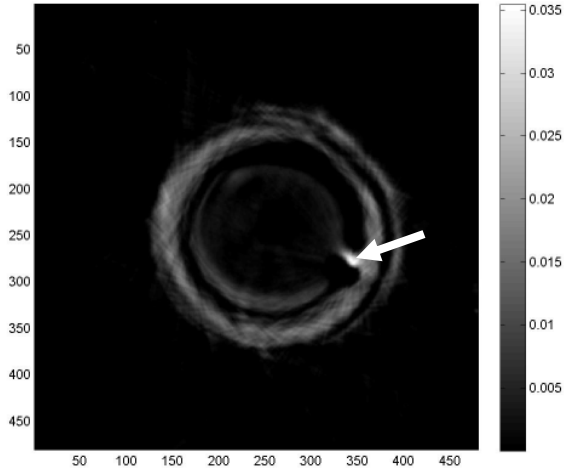


**Figure 71:** The reconstruction image of Figure 61 using the OS-type SART algorithm with 20 subsets and 20 iterations.

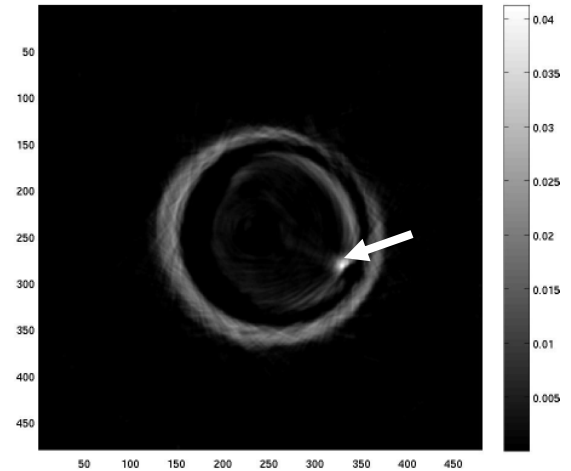


**Figure 72:** The reconstruction image of Figure 62 using the OS-type SART algorithm with 20 subsets and 20 iterations.

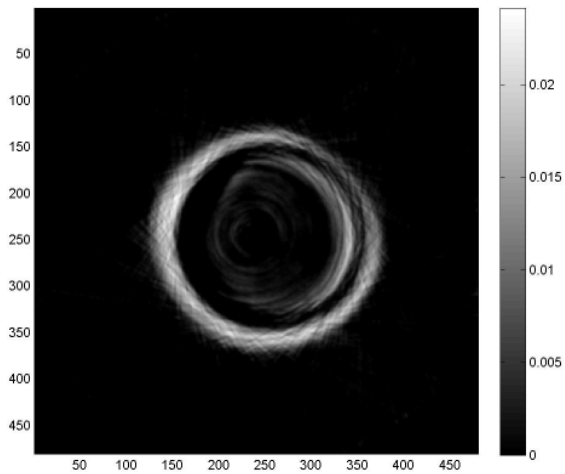


**Figure 73:** The reconstruction image of 150<sup>th</sup> slice using the OS-type SART algorithm with 20 subsets and 20 iterations.

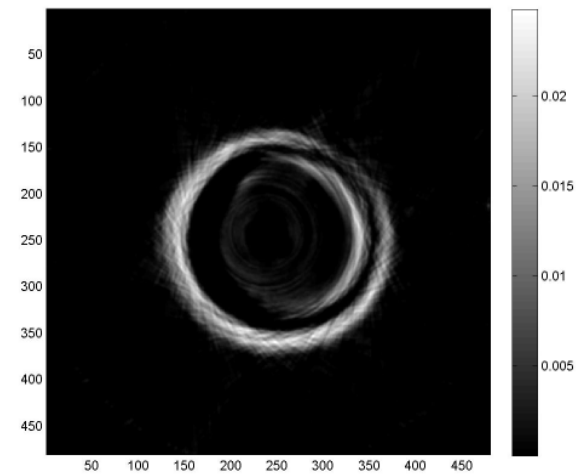


**Figure 74:** The reconstruction image of 450<sup>th</sup> slice using the OS-type SART algorithm with 20 subsets and 20 iterations.

Since there is no interference from a bubble or dust in the sinogram of Figures 73 (150<sup>th</sup> slice), no bright spot appears inside the object. From these reconstruction images, we can find that the space between two PTFE tubes (thickness) is not homogeneous. It is difficult

to obtain a precise thickness of the gap as we make the phantom. In addition, the two PTFE tubes are not completely vertical. In order to evaluate the shape of the second phantom, we measured the number of pixels (area) within two PTFE tubes by using image segmentation and then compare with the theoretical value. The weighted error for the area is less than 5%. The surface rendering in Figure 74 is a part of the second phantom (with 120 slices). As we expected, the surface rendering of the object is almost smooth. These results indirectly prove that the new OT system has the potential for imaging true blood vessel. Clearly, this approximate verification of the reconstructed shape depends on the accuracy of phantom assembly. For example, the area between two circles remains the same even if they are not exactly concentric. This is a limitation that needs to be considered in future studies.

#### **4.6 Comparison: the Reconstruction Time of Reconstruction Algorithms**

As mentioned before, the reconstruction time plays an important role if we image a true blood vessel. In previous experiments, we save the reconstruction time by reducing the number of bins from 1920 to 480. However, the reconstruction time of the SART algorithm is still much longer than that of the FBP algorithm. Table 3 lists the reconstruction time (seconds) of each algorithm for a  $480 \times 480$  image. The number of

Reconstruction algorithms	Reconstruction time (second)
Filtered backprojection (FBP)	10
SART- 100 iteration	550
OS-SART- 5 subsets with 20 iterations	320
OS-SART- 10 subsets with 10 iterations	170
OS-SART- 20 subsets with 5 iterations	90

projections is 400 over 360 degrees. The reconstruction time of the SART algorithm with 100 iterations is 55

**Table 3:** The reconstruction time of each reconstruction algorithm. For iterative algorithms, the number of iteration is the same (100 iterations).

times that of the FBP

algorithm, but the SART algorithm is more accurate than the FBP algorithm. We will compare the performance of the SART algorithm with that of the FBP algorithm in the next paragraph. One simple method to further reduce the reconstruction time is to use the OS-type SART algorithm. Table 3 also shows the reconstruction time of the OS-type SART algorithm with different subsets, but identical numbers of iterations. The total number of iterations is equal to the product of subset number and iteration number. Table 3 shows that the reconstruction time of the OS-type SART algorithm decreases with the increase of the number of subset. The reconstruction time of the OS-type SART algorithm with 20 subsets and 5 iterations is only one sixth of that of the SART algorithm. If the number of iterations for the OS-type SART algorithm with 20 subsets is insufficient, we can use the reconstruction image of the FBP algorithm as an initial condition. This

decreases both the number of iterations and reconstruction time. Figure 75 is the reconstruction image of 270<sup>th</sup> slice using the SART algorithm with 100 iterations. Figure

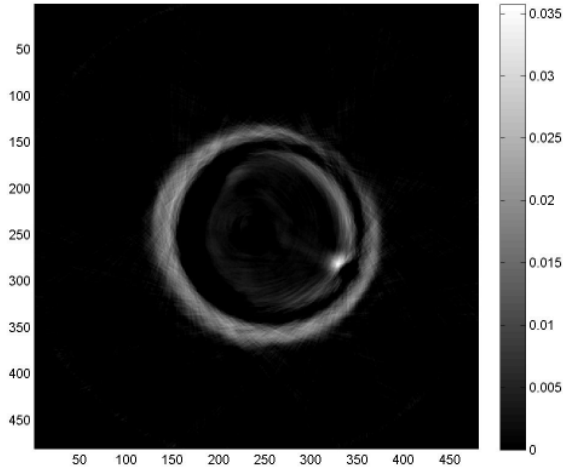


**Figure 75:** The reconstruction image of 270<sup>th</sup> slice using the OS-type SART algorithm with 1 subset and 100 iterations.

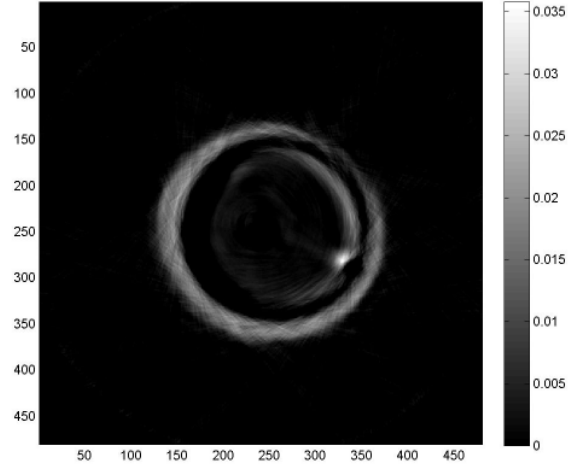


**Figure 76:** The reconstruction image of 270<sup>th</sup> slice using the OS-type SART algorithm with 5 subset and 20 iterations.

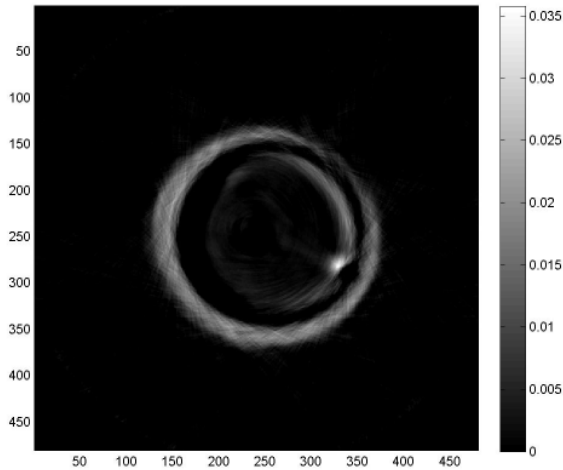


**Figure 77:** The reconstruction image of 270<sup>th</sup> slice using the OS-type SART algorithm with 10 subset and 10 iterations.

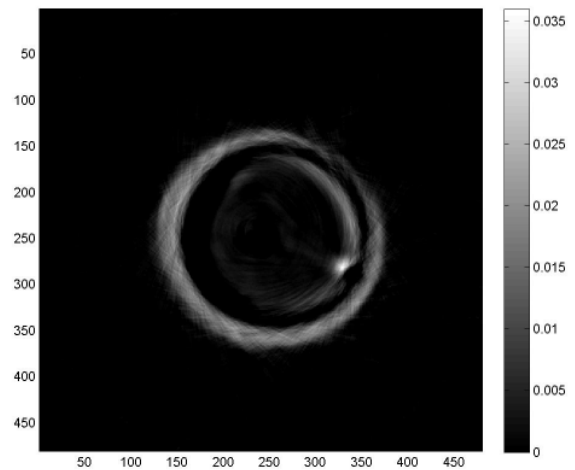


**Figure 78:** The reconstruction image of 270<sup>th</sup> slice using the OS-type SART algorithm with 20 subset and 5 iterations.

76, 77 and 78 are reconstruction images of the OS-type SART algorithm by using 5 subsets with 20 iterations, 10 subsets with 10 iterations and 20 subsets with 5 iterations.

From Figure 75 to Figure 78, the difference of reconstruction images using the OS-type SART algorithm with different subsets is almost indistinguishable.

#### 4.7 Comparison: the Number of Projections

In the OS-type SART algorithm, reconstruction time primarily is dependent on the number of iteration and subset. Furthermore, it is affected by the number of projections.

Table 4 is the reconstruction time and SNR of the OS-type SART algorithm with different project- ions over 360 degrees (ink6). The mean of the object divided by the standard deviation of the object serves as a rough approximation of SNR. The number of subset

Number of projections	Reconstruction time	SNR
400	92	13.69
200	46	10.51
100	24	8.21
50	12	7.48

**Table 4:** The reconstruction time and SNR of the OS-type SART algorithm with different angles over 360 degrees.

was 20 and the number of iteration was 5. In Table 4, the reconstruction time can be seen to decrease

proportionally with the decrease of the number of projections. By comparing Table 4 with

Table 3, it becomes evident that the reconstruction time of the OS-type SART algorithm

(20 subsets and 5 iterations) with 50 projections is very close to that of the FBP algorithm

with 400 projections. However, the image quality is degraded with the decrease of the

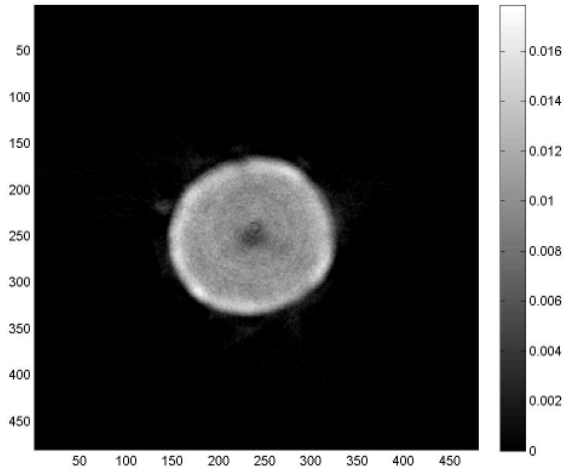


**Figure 79:** The reconstruction image of ink6's 270<sup>th</sup> slice using the OS-type SART algorithm with 400 projections.

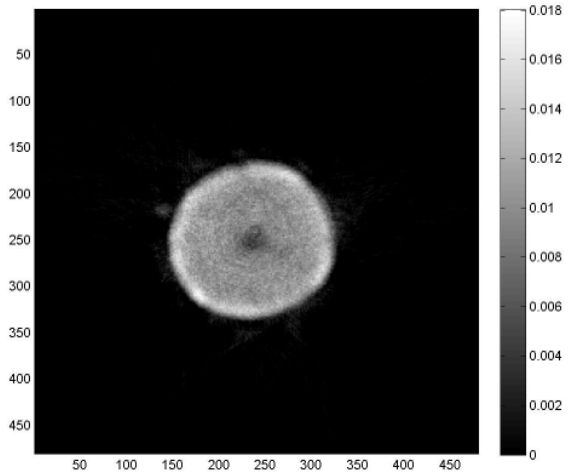


**Figure 80:** The reconstruction image of ink6's 270<sup>th</sup> slice using the OS-type SART algorithm with 200 projections.

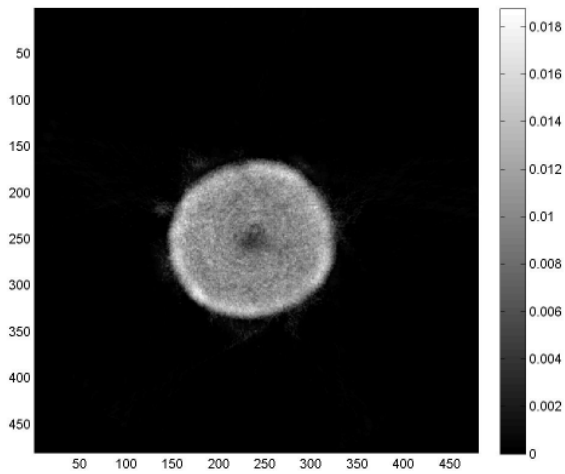


**Figure 81:** The reconstruction image of ink6's 270<sup>th</sup> slice using the OS-type SART algorithm with 100 projections.

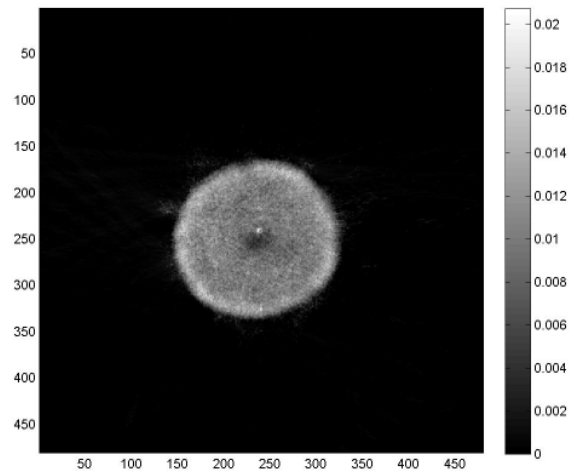


**Figure 82:** The reconstruction image of ink6's 270<sup>th</sup> slice using the OS-type SART algorithm with 50 projections.

number of projection. In Table 4, the SNR of using 400 projections is almost two times of using 50 projections, but their recoveries are almost the same. This means that the recovery is not sensitive to the number of projections. Figures 79, 80, 81 and 82 are

reconstruction images of ink6's 270<sup>th</sup> slice using the OS-type SART algorithm with 400, 200, 100 and 50 projections. For these reconstruction images, the number of subsets was 20 and the number of iterations was 5. By visual comparison from Figure 79 to Figure 82, the reconstruction image with a low number of projections was relatively noisy, but the difference of reconstruction images between 400 projections and 200 projections was relatively small. Because of this reason, we suggest that the reconstruction image of the OS-type SART algorithm with 200 projections would be good choice for reducing reconstruction time and saving scan time.

#### 4.8 Comparison: FBP Algorithm and OS-type SART Algorithm

As shown before, the two primary factors affecting the quality of reconstruction image are the number of projections and parameters of image reconstruction algorithms.

Reconstruction algorithms / Number of projections	400	200	100	50
FBP	8.18	5.92	3.99	2.97
OS-SART- 5 subsets, 20 iterations	13.82	10.80	8.51	7.18
OS-SART- 10 subsets, 10 iterations	13.75	10.72	8.36	7.04
OS-SART- 20 subsets, 5 iterations	13.69	10.51	8.21	7.48

**Table 5:** The SNR of the OS-type SART algorithm and the FBP algorithm with different projections over 360 degrees.

In addition, these parameters determine the reconstruction time. Table 5 is the

comparison of SNR with each reconstruction algorithm and different angles (ink6). From the SNR, we conclude that the OS-type SART algorithm is superior to the FBP algorithm. For the reconstruction image of the OS-type SART algorithm, using a larger number of subsets is slightly noisier (low SNR) than using a small number of subsets, but the former requires shorter reconstruction time since the number of subsets is probably proportional to the degree of reduction of the computation time. Since the difference of the SNR in different subset numbers is relatively small, we can use a larger number of subsets in order to reduce reconstruction time. As shown in Table 4, the SNR of the OS-type SART algorithm would be decreased with the decrease of the number of angle. This phenomenon can also be found in the FBP algorithm. Figure 83 is the reconstruction image of ink6's 270<sup>th</sup> slice using the FBP algorithm (Hamming filter and 0.8 cut-off frequency) with 400 projections. Figures 84, 85 and 86 are reconstruction images of ink6's 270<sup>th</sup> slice using the OS-type SART algorithm with 400 projections. The reconstruction parameters separately were 5 subsets with 20 iterations, 10 subsets with 10 iterations, and 20 subsets with 5 iterations, respectively. Visually, the reconstruction image of the FBP algorithm is more noisy than that of the OS-type SART algorithm. For the OS-type SART algorithm with different subset numbers, only small differences can

be seen. Figure 83 - Figure 86 (400 projections), Figure 87 - Figure 90 (200 projections), Figure 91 - Figure 94 (100 projections) and Figure 95 - Figure 98 (50 projections) are the comparison of each of the reconstruction algorithms. The only difference is the number of projections. As shown in Chapter 3, the FBP algorithm with an inadequate number of angles leads to spoke-like streak artifacts in the reconstruction image. These artifacts can be observed in Figure 91 (100 projections) and Figure 95 (50 projections). Unlike the FBP algorithm, the performance of the OS-type SART algorithm is acceptable when a small number of angles are used. According to these results, we succeeded in reducing the reconstruction time of the SART algorithm by applying ordered subsets of projection data and optimizing the number of projections. Although the reconstruction time of OS-type SART algorithms is still longer than that of the FBP algorithm, the computational cost of the former is acceptable because of the improvement of image quality. Furthermore, we showed that the performance of the OS-type SART algorithm with appropriate parameters is better than that of the FBP algorithm.

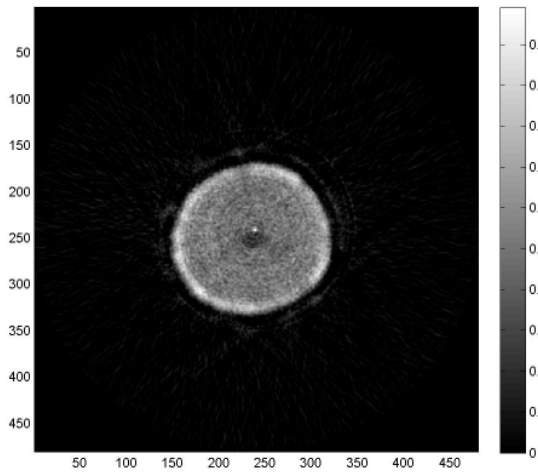


**Figure 83:** The reconstruction image of ink6's 270<sup>th</sup> slice using the FBP algorithm (Hamming filter and 0.8 cut-off frequency) with 400 projections.

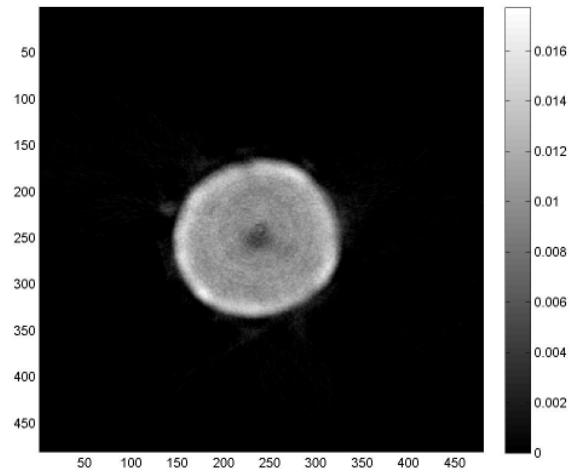


**Figure 84:** The reconstruction image of ink6's 270<sup>th</sup> slice using the OS-type SART algorithm (5 subsets and 20 iterations) with 400 projections.

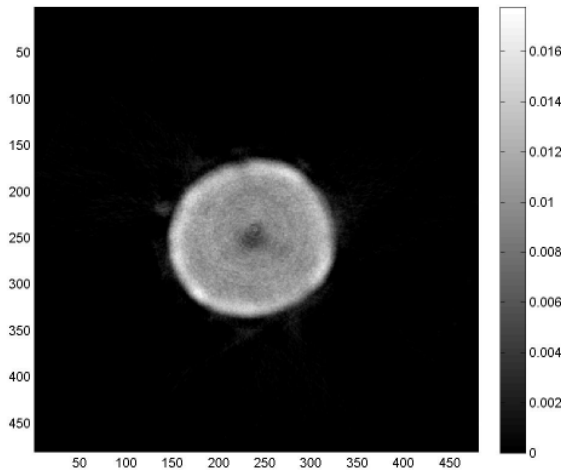


**Figure 85:** The reconstruction image of ink6's 270<sup>th</sup> slice using the OS-type SART algorithm (10 subsets and 10 iterations) with 400 projections.

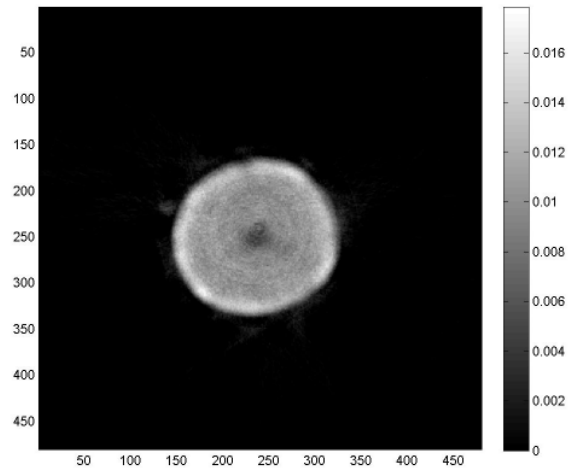


**Figure 86:** The reconstruction image of ink6's 270<sup>th</sup> slice using the OS-type SART algorithm (20 subsets and 5 iterations) with 400 projections.

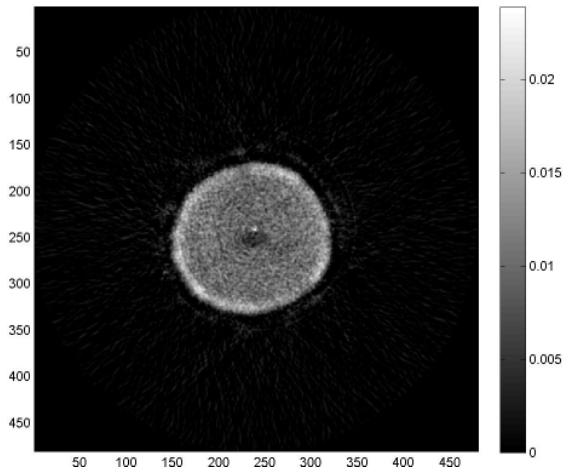


**Figure 87:** The reconstruction image of ink6's 270<sup>th</sup> slice using the FBP algorithm (Hamming filter and 0.8 cut-off frequency) with 200 projections.

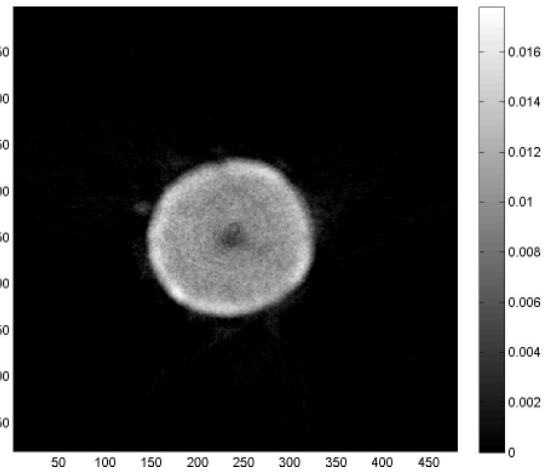


**Figure 88:** The reconstruction image of ink6's 270<sup>th</sup> slice using the OS-type SART algorithm (5 subsets and 20 iterations) with 200 projections.

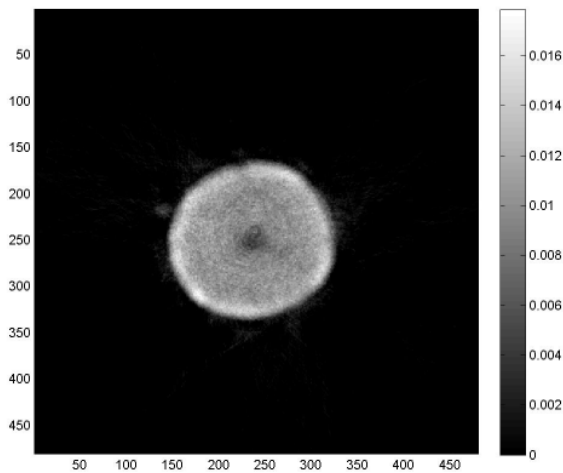


**Figure 89:** The reconstruction image of ink6's 270<sup>th</sup> slice using the OS-type SART algorithm (10 subsets and 10 iterations) with 200 projections.

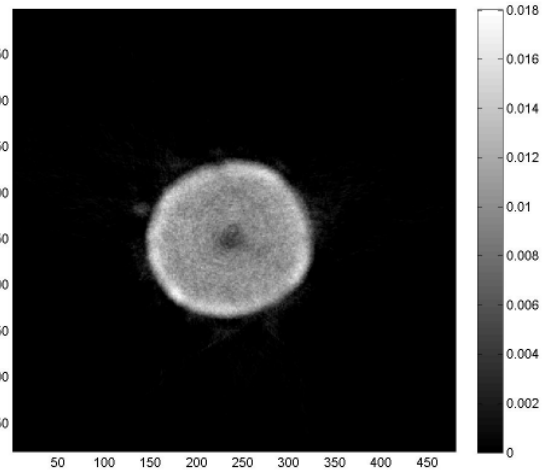


**Figure 90:** The reconstruction image of ink6's 270<sup>th</sup> slice using the OS-type SART algorithm (20 subsets and 5 iterations) with 200 projections.

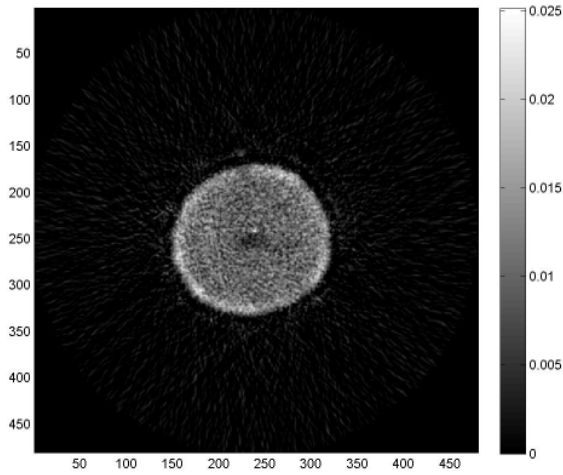


**Figure 91:** The reconstruction image of ink6's 270<sup>th</sup> slice using the FBP algorithm (Hamming filter and 0.8 cut-off frequency) with 100 projections.

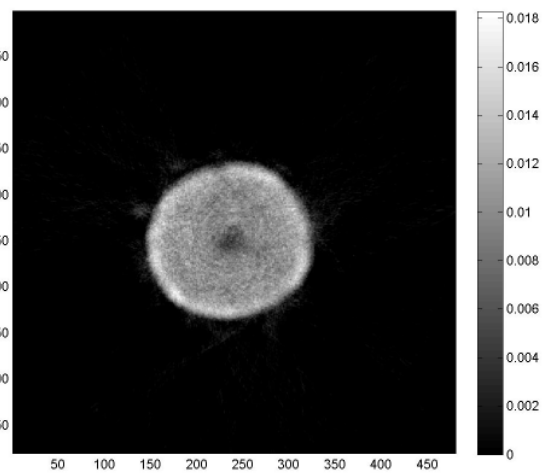


**Figure 92:** The reconstruction image of ink6's 270<sup>th</sup> slice using the OS-type SART algorithm (5 subsets and 20 iterations) with 100 projections.

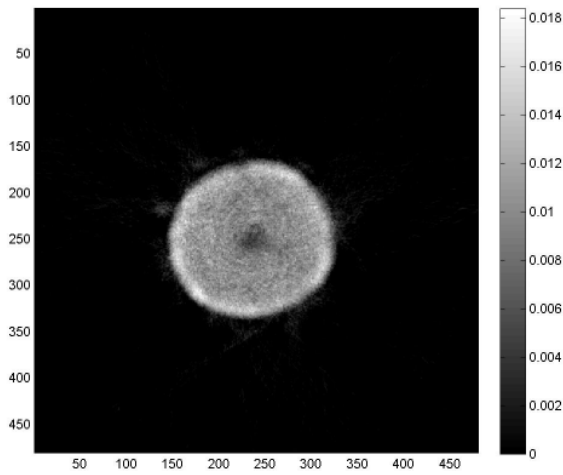


**Figure 93:** The reconstruction image of ink6's 270<sup>th</sup> slice using the OS-type SART algorithm (10 subsets and 10 iterations) with 100 projections.

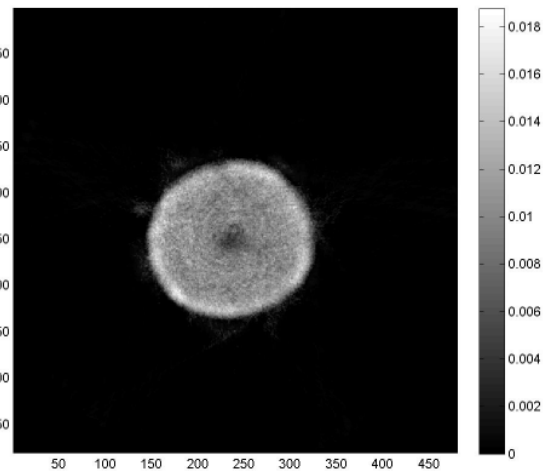


**Figure 94:** The reconstruction image of ink6's 270<sup>th</sup> slice using the OS-type SART algorithm (20 subsets and 5 iterations) with 100 projections.

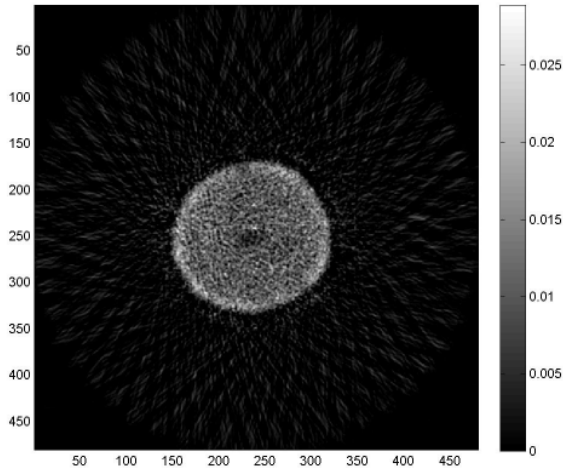


**Figure 95:** The reconstruction image of ink6's 270<sup>th</sup> slice using the FBP algorithm (Hamming filter and 0.8 cut-off frequency) with 50 projections.

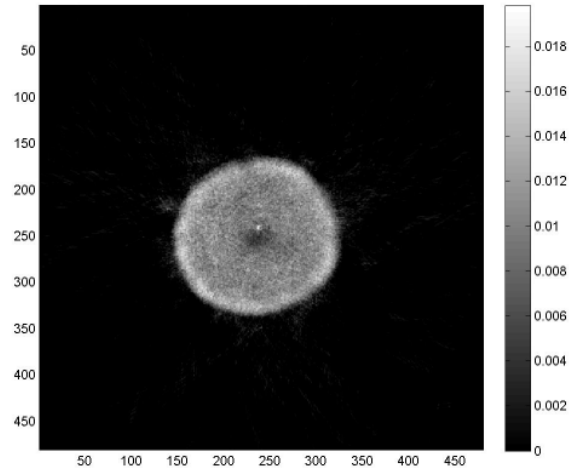


**Figure 96:** The reconstruction image of ink6's 270<sup>th</sup> slice using the OS-type SART algorithm (5 subsets and 20 iterations) with 50 projections.

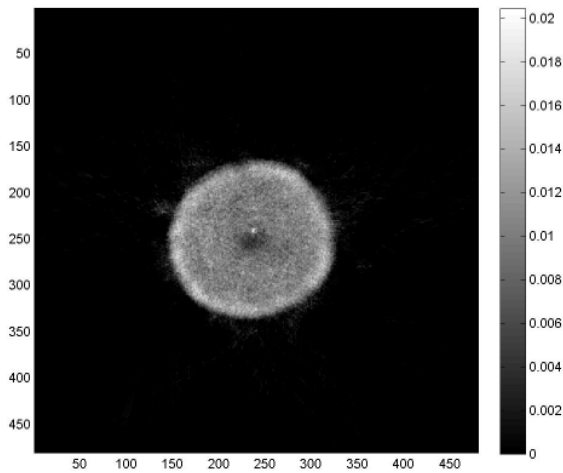


**Figure 97:** The reconstruction image of ink6's 270<sup>th</sup> slice using the OS-type SART algorithm (10 subsets and 10 iterations) with 50 projections.

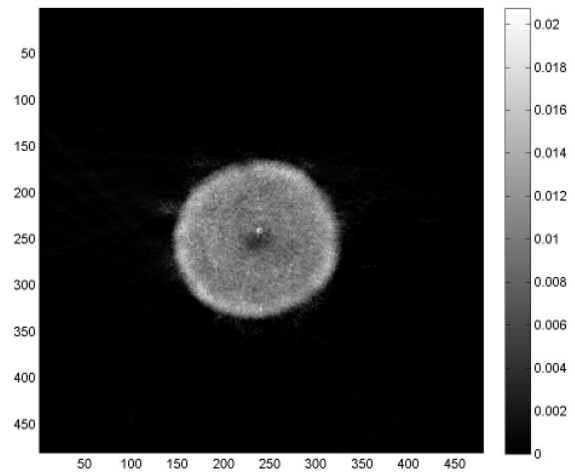


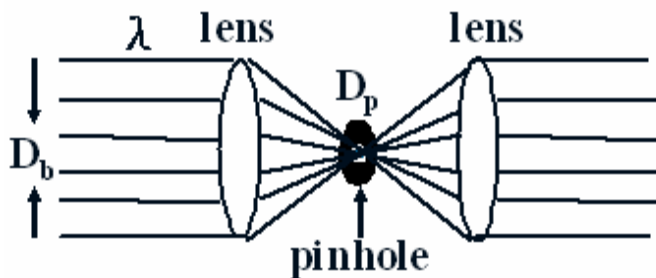
**Figure 98:** The reconstruction image of ink6's 270<sup>th</sup> slice using the OS-type SART algorithm (20 subsets and 5 iterations) with 50 projections.

## CHAPTER 5

### DISCUSSION

#### 5.1 System Design: Spatial Filter

As we described earlier, the spatial filter plays an important role in the new OT system. Its primary function is to reject scattered photons. Figure 99 is a scheme of the spatial filter consisting of two lenses that have a common focus and one pinhole located in the focal plane.  $D_b$  is the diameter of the lens,  $D_p$  is the diameter of the pinhole and  $\lambda$  is



the wavelength of incident light.

Parallel incident light is focused by

the first lens through the pinhole and

expanded by the second lens. In the

focal plane, a diffraction pattern

**Figure 99:** The diagram of the spatial filter. It consists of two lenses and one pinhole.  $D_b$  is the diameter of the lens,  $D_p$  is the diameter of the pinhole and  $\lambda$  is the wavelength of incident light.

generated by the first lens is a Fourier transform of the light distribution from the object

plane. The diffraction pattern is composed of the spatial frequency spectrum of the object.

A specific frequency can be represented by its distance from the axis of the system.

Generally, the high-frequency components indicate details of the object. If a pinhole is

inserted at the focal plane, these high-frequency components will be removed. On the other hand, the low-frequency components near the axis would pass through the pinhole without perturbation. Finally, the second lens performs the inverse Fourier transform and then projects the filtered diffraction pattern onto the image plane. So, a pinhole with a larger  $D_p$  increases resolution, but it also amplifies noise. Conversely, a smaller  $D_p$  suppresses noise and reduces resolution simultaneously. In addition, the  $D_p$  determines the rejection angle of the spatial filter. Usually, refracted photons due to the mismatch of refractive index pass toward high-frequency components. Thus, a larger  $D_p$  allows more strongly refracted photons to pass through the pinhole and a smaller  $D_p$  lowers the rejection angle.

In theory, the  $D_p$  can approximately be estimated by the following equation:

$$D_p = \frac{2F\lambda}{D_b} \quad (15)$$

where  $F$  is the focal length of the lens [Goodman, 2005]. In the new OT system, the wavelength of light is 625 nm with 20 FWHM,  $D_b$  is 25.4 mm and  $F$  is 40 mm.

According to Equation 15,  $D_p$  roughly equals to  $2 \mu m$ . In fact, the minimum diameter we ever used was  $10 \mu m$ . However, the distribution of transmitted light after the second lens is much smaller than that of incident light if  $D_p$  is  $10 \mu m$ . Furthermore, its intensity is

very weak. Based on the experimental determination of the ideal pinhole size, the distribution of transmitted light is similar to that of incident light unless the diameter is larger than  $100\ \mu\text{m}$ . Under the consideration of distribution and intensity, we used a pinhole with  $150\ \mu\text{m}$  in the new OT system, although the diameter is extremely different from the theoretical value. In the spatial filter, the incident light must be completely parallel and monochromatic. In addition, the pinhole must be in the focal plane. In the new OT system, we used a LED as the light source in order to reduce the interference effect. However, the light from the LED is divergent and not monochromatic. Although the transformation from the divergent beam to a parallel beam can be achieved by a collimated lens and a spatial filter, small errors are unavoidable. Besides, the accurate alignment of the pinhole in the focal plane is very difficult. Other possible reasons are optical aberrations such as spherical, coma, astigmatism and distortion. Sequentially, these factors directly affect the function of the spatial filter. In the new OT system, the alignment of these components was based on our experience, so the inter-experiment variations are to be expected. In the future, one of primary works is to evaluate the bias from each component and to minimize it. In addition, it would be interesting to investigate the effect of pinholes with various diameters on image quality.

## 5.2 Refractive Index

In Chapter 3, we used the solution of sucrose to reduce the mismatch of refractive index between background and the PTFE tube. In the first experiment, the smallest refractive regions can be achieved with 3.8 g sucrose in 100 mL of water. However, a complete match of refractive index was not found in this experiment. A variation of sucrose concentration from 3.8 g to 3.9 g in 100 mL of water in steps of 0.01 g did not yield any significant change of the refracting regions. Two possible reasons are the inaccurate alignment of each component and optical aberrations. In the second experiment, we used 4.6 g sucrose instead of 3.8 g sucrose. Like the first experiment, an exact match of refractive index was also infeasible. Primary reasons are the same as with the first experiment. Another reason is that the thickness of the inner PTFE tube is different from that of the outer PTFE tube. Generally, the refractive index is dependent on the composition of the material. In fact, the thickness of the material also slightly changes its refractive index. For the inner PTFE tube, 3.8 g sucrose can reduce the mismatch efficiently, but it is insufficient for the outer PTFE tube. For these two PTFE tubes, we found that total refractive regions are as small as possibly achievable if 4.6 g sucrose is

used. This is why we used 4.6 g sucrose instead of 3.8 g sucrose in the second experiment.

After the alignment of each component, one future study is to find a solution at a concentration that matches the refractive index of the blood vessel. Since the reconstruction image is affected by the mismatch of the refractive index, a tissue compatible solution is required.

### **5.3 Comparison of Reconstruction Algorithms**

Generally, iterative algorithms such as the SART algorithm require higher computational cost than analytical algorithms such as the FBP algorithm. The primary computational time of the iterative algorithm is determined by the system matrix and the forward/backward projection. In our previous studies, the SART algorithm took several hours per slice. To save reconstruction time, we used a popular ray-tracing method [Siddon, 1985] that is used in CT to calculate the system matrix. Furthermore, we used a rotated-based matrix along with symmetric properties of the system matrix for further reducing computational load and computer memory. As compared to our previous studies, the new implementation of the SART algorithm (100 iterations, image size=  $480 \times 480$  and sinogram=  $480 \text{ bins} \times 400 \text{ angles}$ ) requires about 550 seconds per slice. However, the

FBP algorithm only takes about 10 seconds per slice. In order to reduce the difference, the OS-type SART algorithm [Wang and Jiang, 2004] that applied ordered subset of projection [Hudson and Larkin, 1994] to the SART algorithm can be implemented easily with a slight modification. For the OS-type SART algorithm, the choice of the number of subsets is significant since it is proportional to the degree of reduction of the computational time. It also affects the quality of the reconstructed image but only in a minimal way. Based on our results, the OS-type SART algorithm with 20 subsets (5 iterations) requires about 90 seconds per slice. To compare with the SART algorithm, the difference of the reconstruction time between the FBP algorithm and the OS-type SART algorithm is relatively small, although the use of a large number of subsets degrades the image quality slightly. Since the difference of reconstruction images with various subset numbers is almost invisible, choosing a large number of subsets for computation reduction is acceptable.

Unfortunately, the computational time becomes a consideration if a large number of slices need to be reconstructed. For example, the number of slice per graft may be more than 2000 slices. The OS-type SART algorithm with 20 subsets and 5 iterations takes about 50 hours if there are 2000 slices. Fortunately, several potential solutions to improve

the efficiency can be found. One is to build a computer cluster with multiprocessor boards since computer hardware is relatively inexpensive. Also, it is possible to reduce the number of slices and image size if we use a larger pixel width, although the image quality would be degraded. Furthermore, the number of iteration in the OS-type SART algorithm can be decreased if we use a FBP reconstruction as an initial condition. In addition to these methods, Fourier-based forward and back-projection methods have the potential to markedly reduce the computational load largely. In the late 1980's, Crawford et al. (1986, Crawford et al., 1988) applied Fourier-based projection methods to correct beam hardening effect in X-ray CT and Stearns et al. (1987, 1990) compensated missing projections in 3D positron emission tomography (PET) reconstruction. However, these methods were limited by unacceptable image artifacts. These artifacts were caused by larger interpolation errors that related to conventional gridding methods for converting between polar and Cartesian coordinates in frequency domain. Recently, Matej et al. (2004) applied a min-max interpolation method to minimize the interpolation errors. They showed that Fourier-based projectors in parallel beam tomography can perform at least 10 times faster, and are reasonably accurate as compared to space-based methods. This indicates that reconstructing a large number of slices in a short time is possible. To

scan about one fourth of the length of the phantom, the scan time of 400 projections takes about 15 minutes. If we optimize some scanning parameters such as the number of angles and the acquisition time, it is possible to scan the full length of the phantom within one hour. In the future, the short scan time and the acceptable reconstruction time for monitoring the quality of a vessel will be possible if we apply these methods to the new OT system.

#### **5.4 Artifacts in Reconstruction Images**

In Chapter 3, we verified that artifacts from the shift of COR and the mismatch of registration could efficiently be suppressed. We also found that the reason underestimated attenuation coefficients in the center of the object is the mismatch of refractive index between the PTFE tube and ink. The mismatch causes specular reflection, which reflects light back to its original direction. In the pre-scan (the PTFE tube without ink), a part of light undergoes specular reflection. In the post-scan (the PTFE tube with ink), the proportion of light undergoing specular reflection is reduced since the refractive index of the solution inside the PTFE tube changes slightly. Thus, some light would be attenuated by the ink or detected by the CCD camera. Since we found higher intensity in the

projection, this shows that the underestimation of attenuation coefficients comes from detecting additional signal. We also found that this artifact would be relatively serious if the concentration of ink decreases (low attenuation coefficients). This is because low attenuation coefficients have higher probability to detect these additional signals than high attenuation coefficients. Since the mismatch of refractive index may be reduced or eliminated after the accurate alignment of the new OT system, this artifact would be removed. Also, this artifact would be reduced as we scan the vessel. Since the vessel has higher scattering attenuation coefficients, the probability to collect these additional signals would be decreased.

The mismatch of refractive index also causes many scattered photons. Since these scattered photons are blocked by the spatial filter, the intensity of some regions in the projection is close to background. These regions are called refractive regions. This means that there is no information in these regions. As a result, attenuation coefficients are inaccurate because we ignore these regions during image reconstruction process [Haidekker, 2005]. Again, the match of refractive index will be a simple and efficient solution.

Figure 100 is the reconstruction image of the second phantom (450<sup>th</sup> slice) using the

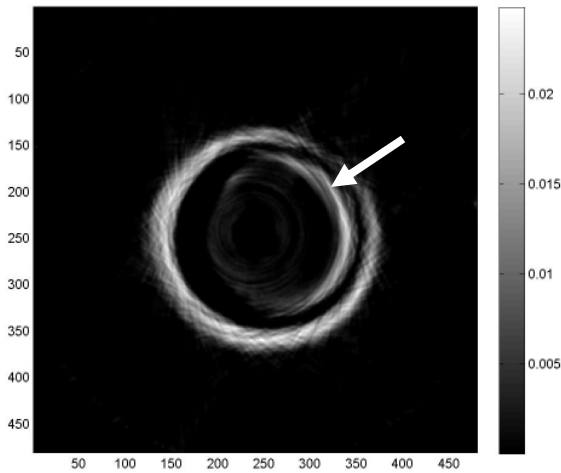


**Fig 100:** The reconstruction image of 450<sup>th</sup> slice using the OS-type SART algorithm with 20 subsets and 20 iterations.

OS-type SART algorithm with 20 subsets and 5 iterations. We can observe a shadow (arrow) inside the object. The primary reason is the mismatch of the intensity between the pre-scan and the post-scan.

Figure 101 is the profile of the projection (450<sup>th</sup> slice) at 250 angles. The

blue line is the intensity without ink ( $I_0$ : pre-scan), the red line is the intensity with ink (I:

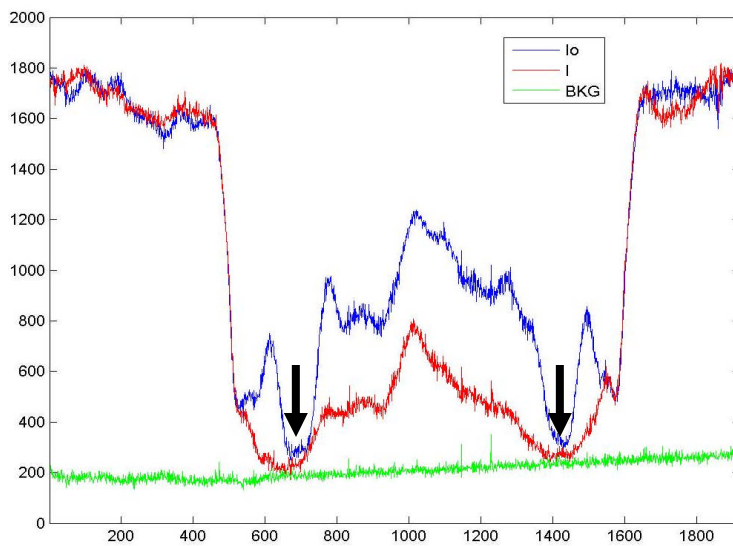


**Figure 101:** The profile of the projection (450<sup>th</sup> slice) at 250 angles. The blue line is the intensity without ink ( $I_0$ ), the red line is the intensity with ink (I) and the green line is the background

post-scan) and the green line is the background (BKG). In Figure 101, the intensity of the pre-scan ( $I_0$ ) in the second refractive regions (arrow: the inner PTFE tube) is slight higher than BKG. In theory, the intensity in these regions

should be close to that in the post-scan (or BKG.) since the scattered photons are rejected

by the spatial filter. This means that we do not have any signal in these regions. If the intensity in these regions mismatches, we would observe many unexpected signals in the sinogram. Sequentially, a shadow in the reconstruction image would be generated. One simple way to reduce this artifact is to use a threshold. Below the threshold, the intensity would be set to zero. The cause of the mismatch may be the inconsistency of two scans. Possible inconsistent conditions include a slight change of the intensity of the incident light, the sensitivity of the CCD camera and the setup of the OT system. As we mentioned before, these factors affect the accuracy of the new OT system. These factors will be an important consideration when we align the new OT system.

For the scan of a blood vessel, we expect that the pre-scan and the post-scan are necessary if the spatial filter rejects some required signals (= underestimation of intensity in the middle of the tube). Even though the spatial filter works well, we can use the pre-scan to remove the attenuation of the tube since our purpose is to monitor the vessel rather than the tube.

## 5.5 Conclusion

We have demonstrated that the new OT system can provide a very short scan time as compared to the old one. For the iterative algorithm, we also successfully reduced its reconstruction time by using several popular techniques, but the reconstruction time becomes an issue if there are a large number of slices. Fortunately, there are many methods to further reduce the total reconstruction time. One simple and efficient strategy is to build a computer cluster since the computer hardware is relatively inexpensive. The other is to use Fourier-based projectors during the forward and backward projections. In the future, a vessel could be scanned and reconstructed within one hour if we optimize the new OT system and apply these methods to iterative algorithms.

Under the mismatch of refractive index, we have shown that the new OT system can provide an accurate reconstruction image with a slight underestimation of attenuation coefficients. In addition, the attenuation coefficient measured from our OT system has a high correlation with that measured from the spectrometer. This proved that the new OT system can be used to scan an object with different attenuation coefficients. To reduce the underestimation of attenuation coefficients and remove image artifacts due to the mismatch of refractive index, we plan to perform an evaluation for the alignment of each

component and then minimize the bias. Also, we will find a solution at a concentration to eliminate the mismatch of refractive index without damaging the vessel. After these studies, we will focus on the scan of a blood vessel and the comparison between the new OT system and other modalities such as OCT.

# APPENDIX

## A. PROGRAMMING

```
/*-----sart.c-----*/  
  
#include <stdio.h>  
#include <string.h>  
#include <malloc.h>  
#include <math.h>  
#include "INCLUDE/fileio.h"  
#include "INCLUDE/project1.h"  
  
void main( void )  
{  
FILE *fp;  
int i,j,p,s,p1,a;  
int t1,t2,t3;  
int pp1,pp2,pp3;  
int num,iter;  
float lamda,max;  
short status;  
int angle;  
float *buf, *image, *temp, *temp1;  
float atnlen1,atnlen2,atnlen3;  
float max_angle;  
unsigned short x1,x2,x3;  
unsigned short y1,y2,y3;  
char fname0[50];  
char fname1[50];  
char fname2[50];  
char fname3[50];  
time_t timer1;  
struct bintbl bin;  
struct rusage rusage;  
struct data d;
```

```

memset(fname0, 0, 50);
memset(fname1, 0, 50);
memset(fname2, 0, 50);
memset(fname3, 0, 50);

/* --- Read Input Data for SART Reconstruction --- */
fp = fopen("sart.dat","r");
if( fp == NULL ) {
    printf("### Error: em.dat not found!!\n");
    exit(1);
}

fscanf(fp, "%d %d %d %f %f %f %d %s %s %s %s %d %d %d %d %f", &IMGSIZ,&ANGLES,&BINS, &COR.ratio,
&COR.i,&COR.j,&RAYS,fname0,fname1,fname2,fname3,&METHOD,&angle,&SUBSET,&num,&lamda);
fclose(fp);

//memory allocation for the data structure
status=datamemory(&d);
if(!status)
{
    printf("Problem with memory allocation for data structure!!\n");
    exit(1);
}

buf = (float *)calloc( IMGSIZ*IMGSIZ,sizeof(float) );
if( buf == NULL )
{printf("memory problem!!\n"); exit(1);}
image = (float *)calloc( IMGSIZ*IMGSIZ,sizeof(float) );
if( image == NULL )
{printf("memory problem!!\n"); exit(1);}
temp = (float *)calloc( IMGSIZ*IMGSIZ,sizeof(float) );
if( temp == NULL )
{printf("memory problem!!\n"); exit(1);}
temp1 = (float *)calloc( IMGSIZ*IMGSIZ,sizeof(float) );
if( temp1 == NULL )
{printf("memory problem!!\n"); exit(1);}

```

```

/* ----- Display Input Data ----- */
printf("\n### %dX%d SART Reconstruction ###\n",IMGSIZ,IMGSIZ);
printf("ANGLES=%d, BINS=%d\n",ANGLES,BINS);
printf("COR.ratio(bin/pixel)=%f\n",COR.ratio);
printf("Center Of Rotation (i=%f,j=%f)\n",COR.i,COR.j);
printf("Number of subbins (RAYS): %d\n",RAYS);
printf("Projection data      : %s\n",fname0);
printf("Output file name   : %s\n",fname1);
printf("Initial file name   : %s\n",fname2);
printf("Mask file name     : %s\n",fname3);
printf("Angle option       : %d\n",angle);
printf("Interpolation method : %d\n",METHOD);
printf("1: bilinear method, 2: bicubic method\n");
printf("Subset              : %d\n",SUBSET);
printf("Iteration option    : %d\n",num);
printf("Lamda                : %f\n",lamda);

/* ----- Allocate memory for LUT ----- */
printf("\nAllocating Memory.....\n");
status = alloc_binmem( &bin );
if( !status ) {
    printf("### Error: Unable to allocate bin memory!!\n");
    exit(1);
}

COR.intercept=BINS/2.;
COR.x=(float)COR.j+0.5;
COR.y= (float)(IMGSIZ-COR.i)-0.5;

/* Compute Discrete Angles */
max_angle = (float)angle*M_PI/180;
set_angles( max_angle );

/* ----- Build Look-Up Table ----- */
printf("Building LUT...\n\n");

```

```

getrusage(RUSAGE_SELF, &rusage);
timer1 = (rusage.ru_utime.tv_sec*1000+rusage.ru_utime.tv_usec/1000);

    lut( &bin, (float *)image );

getrusage(RUSAGE_SELF, &rusage);
timer1 = (rusage.ru_utime.tv_sec*1000+rusage.ru_utime.tv_usec/1000)- timer1;
printf("Computation time: %d (ms)\n",timer1);

/* ----- Precomputation of Normalization Factor ----- */
printf("Precomputing Normalization Factor...\n\n");

for(a=0; a<SUBSET; a++){ //subset

    for (s=0; s<ANGLES; s=s+SUBSET) {

        memset(buf,0,sizeof(float)*IMGSIZ*IMGSIZ);

        for(i=0; i<IMGSIZ/2; i++) {
            for(j=0; j<IMGSIZ; j++) {

                /* -- Calculate Index for LUT -- */
                p1=i*IMGSIZ+j;
                pp1=(IMGSIZ-1-i)*IMGSIZ+j;

                /* Read Attenuation Lengths 1 & 2 from LUT */
                t1 = (int)*(bin.bin1 + p1);
                t2 = (int)*(bin.bin2 + p1);
                t3 = (int)*(bin.bin3 + p1);
                atnlen1 = *(bin.atnlen1 + p1);
                atnlen2 = *(bin.atnlen2 + p1);
                atnlen3 = *(bin.atnlen3 + p1);

                /* Accumulate Normalization Factor */
                if (t1>0){

```

```

        *(buf+p1)+=atnlen1;
        *(buf+pp1)+=atnlen1;
    }
    if (t2>0){
        *(buf+p1)+=atnlen2;
        *(buf+pp1)+=atnlen2;
    }
    if (t3>0){
        *(buf+p1)+=atnlen3;
        *(buf+pp1)+=atnlen3;
    }
}
}

```

```
rotimg((float *)buf,s,(float *)image,-1,METHOD);
```

```

for(i=0; i<IMGSIZ; i++) {
    for(j=0; j<IMGSIZ; j++) {
        p=i*IMGSIZ+j;
        p1=a*IMGSIZ*IMGSIZ+i*IMGSIZ+j;
        *(d.normSubset+p1)+=*(image+p);
    }
}

```

```
//end of angles
```

```
}//end of subset
```

```

for (s=0; s<ANGLES; s++) {
    for(i=0; i<IMGSIZ; i++){
        for(j=0; j<IMGSIZ; j++){
            p1=i*IMGSIZ+j;
            *(buf+p1) =1;
        }
    }
}

```

```
rotimg((float *)buf,s,(float *)image,1,METHOD);
```



```

/* ----- Load observed projection data ----- */
status = load_data(fname0, d.g_obs,'f', ANGLES, BINS);
if( !status ) exit(1);

/* ----- */
if( fname3[0] != '0' ) status = load_data(fname3, d.mask, 'b', IMGSIz, IMGSIz);
else memset(d.mask,1,IMGSIz*IMGSIz);

if( fname2[0] != '0' ) status=load_data(fname2,d.f_est,'f',IMGSIz,IMGSIz);
else {
for(i=0; i<IMGSIz; i++)
for(j=0; j<IMGSIz; j++)
{
p1=i*IMGSIz+j;
if((d.mask+p1)>0)
*(d.f_est+p1) = 0.00001;
}
}

/* ----- Initialize Timer and Start Counting ----- */
getrusage(RUSAGE_SELF, &rusage);
timer1 = (rusage.ru_utime.tv_sec*1000+rusage.ru_utime.tv_usec/1000);
iter = 0; //--> Initialize Iteration Counter
status = 1; //--> Set status=1

/* ----- SART Iteration Loop ----- */
printf("Starting SART Loop...\n\n");
do {
memset(temp1,0,sizeof(float)*IMGSIz*IMGSIz);
memcpy(temp1,d.f_est,sizeof(float)*IMGSIz*IMGSIz);
for(a=0; a<SUBSET; a++){

fwdprj1OS((float *)d.f_est,(float *)d.g_est,(byte *)d.mask,&bin,a);

```

```

/* ----- Compute d.g_rat = [d.g_obs-d.g_est]/norm ----- */
for(i=a; i<ANGLES; i=i+SUBSET) {
    for(j=0; j<BINS; j++) {
        p=i*BINS+j;
        /*---approach one:omit zero prj--- */
        if (*(d.norm+p)>0) *(d.g_rat+p)=(*(d.g_obs+p)-*(d.g_est+p))/ *(d.norm+p);
    }
}

/* ----- Update Pixels ----- */
memset(temp,0,sizeof(float)*IMGSIZ*IMGSIZ);

for (s=a; s<ANGLES; s=s+SUBSET) {

    memset(buf,0,sizeof(float)*IMGSIZ*IMGSIZ);

    for(i=0; i<IMGSIZ/2; i++) {
        for(j=0; j<IMGSIZ; j++) {
            p = i*IMGSIZ+j;
            pp1=(IMGSIZ-1-i)*IMGSIZ+j;
            if( *(d.mask+p) == 0 )
                continue;

            /* ----- Backprojection ----- */
            t1 = (int)*(bin.bin1 + p);
            t2 = (int)*(bin.bin2 + p);
            t3 = (int)*(bin.bin3 + p);
            atlen1 = *(bin.atlen1 + p);
            atlen2 = *(bin.atlen2 + p);
            atlen3 = *(bin.atlen3 + p);
            if (t1!=0){
                *(buf+p)+= atlen1 * *(d.g_rat+s*BINS+t1);
                x1=floor(t1/BINS); y1=BINS-1-(t1-x1*BINS);
                *(buf+pp1)+=*(d.g_rat+BINS*s+y1)*atlen1;
            }
        }
    }
}

```

```

        if (t2!=0){
            *(buf+p)+= atnlen2 * *(d.g_rat+s*BINS+t2);
            x2=floor(t2/BINS); y2=BINS-1-(t2-x2*BINS);
            *(buf+pp1)+=*(d.g_rat+BINS*s+y2)*atnlen2;
        }
        if (t3!=0){
            *(buf+p)+= atnlen3 * *(d.g_rat+s*BINS+t3);
            x3=floor(t3/BINS); y3=BINS-1-(t3-x3*BINS);
            *(buf+pp1)+=*(d.g_rat+BINS*s+y3)*atnlen3;
        }
    }
}
rotimg((float *)buf,s,(float *)image,-1,METHOD);

    for(i=0; i<IMGSIZ; i++) {
        for(j=0; j<IMGSIZ; j++) {
            p=i*IMGSIZ+j;
            *(temp+p)+=(image+p);
        }
    }
} //end of angles

    for(i=0; i<IMGSIZ; i++) {
        for(j=0; j<IMGSIZ; j++) {
            p=i*IMGSIZ+j;
            p1=a*IMGSIZ*IMGSIZ+i*IMGSIZ+j;
            if (*(d.normSubset+p1)>0) *(d.f_est+p)+=lamda* *(temp+p)/ *(d.normSubset+p1);
            if (*(d.f_est+p)<0) *(d.f_est+p)=0;
        }
    }

} //end of subset

printf("Iteration # %d\n", iter+1);

if( iter > 0 ) {
    if( num > 0 && iter+1 < num ) status = 1;
}

```

```

        else status = 0;
    }
    if( num == 1 ) status = 0;

    iter++;

} while ( status );

getrusage(RUSAGE_SELF, &rusage);
timer1 = (rusage.ru_utime.tv_sec*1000+rusage.ru_utime.tv_usec/1000)- timer1;
printf("Computation time: %d (ms)\n",timer1);

    save_data(fname1,d.f_est,f,IMGSIZ,IMGSIZ);
}

/*-----fileio.h-----*/
#define    SUCCESS    1

int    load_data(char *fname, void *buf, char type, int col, int row);
void    save_data(char *fname, void *buf, char type, int col, int row);

/*-----fileio.c-----*/
#include    <stdio.h>
typedef unsigned char    byte;
FILE    *fp;

int    load_data(char *fname, void *buf, char type, int col, int row)
{
    if ((fp = fopen(fname, "rb"))==NULL) {
        printf("Unable to open file %s\n", fname);
        return(0);
    }

    switch( type )
    {

```

```

        case 'i' : fread((char*)buf, sizeof(int)*col, row, fp);
                break;
        case 's' : fread((char*)buf, sizeof(short)*col, row, fp);
                break;
        case 'b' : fread((char*)buf, col, row, fp);
                break;
        default      : fread((char*)buf, sizeof(float)*col, row, fp);
    }
    fclose(fp);
    return(1);
}

```

```

void save_data(char *fname, void *buf, char type, int col, int row)
{
    fp = fopen(fname, "wb");
    switch( type )
    {
        case 'i' : fwrite((char*)buf, sizeof(int)*col, row, fp);
                break;
        case 's' : fwrite((char*)buf, sizeof(short)*col, row, fp);
                break;
        case 'b' : fwrite((char*)buf, col, row, fp);
                break;
        default      : fwrite((char*)buf, sizeof(float)*col, row, fp);
    }
    fclose(fp);
}

```

```

/*-----project1.h-----*/

```

```

#ifndef _PROJECT1_H
#define _PROJECT1_H
#include <sys/time.h>
#include <sys/resource.h>
#include <stdlib.h>

```

```

#include <stddef.h>
#include <stdio.h>
#include <malloc.h>

int    IMGSIZ;      /* width or height of square image */
int    ANGLES;     /* number of discrete angles */
int    BINS;       /* number of detector bins */
int    RAYS;
int    METHOD;
int    SUBSET;

#ifndef byte
typedef unsigned char    byte;
#endif
#ifndef u_short
typedef unsigned short   ushort;
#endif

struct data {

    byte    *mask; // [IMGSIZ][IMGSIZ];
    float   *f_est; // reconstructed image
    float   *g_obs; // observed projection
    float   *g_est; // estimated projection
    float   *g_rat; // ratio
    float   *normSubset; // normalization factors out
    float   *norm;

};

/* - structure to store the information obtained from Siddon's method - */
struct raytbl {
    ushort  *x;      //x[IMGSIZ*2];      /* pixel index for i of f[i][j] */
    ushort  *y;      //y[IMGSIZ*2];      /* pixel index for j of f[i][j] */
    float   *length; //length[IMGSIZ*2]; /* chord length */
    short   size;    /* number of pixels along a ray */
};

```

```

struct cor {
    float i;
    float j;
    float x;
    float y;
    float intercept;
    float pixel_size;
    float bin_size;
    float ratio;
}

COR;

/* structure for look-up table */
struct bintbl {
    ushort *bin1;
    ushort *bin2;
    ushort *bin3;
    float *atnlen1;
    float *atnlen2;
    float *atnlen3;
};

/* definition of structure type for discrete angles and sin, cos, tan */
typedef struct {
    float rad;
    float sin;
    float cos;
    float tan;
} setang;

extern setang ang[500]; /* global array for discrete angles */
extern float ax[5]; /* angles for 90, 180, 270, 360 */

/* ----- definitions of function types ----- */
int merge(int m, int n, float *Ax, float *Ay, float *alpha);

```

```

void    ray_trace( int theta, float x1, float y1, float x2, float y2,struct raytbl *ray );
void    intersect1( int i, float j, float *x1, float *y1, float *x2, float *y2 );
void    set_angles( float max_angle );
short   alloc_binmem( struct bintbl *bin );
void    free_binmem( struct bintbl *bin );
void    fwdprjIOS( float *, float *, byte *, struct bintbl *bin,int);
void    lut( struct bintbl *bin, float *);
short   datamemory(struct data *d);
#endif  //end of PROJECT_H

```

```

/*-----datamemory.c-----*/

```

```

#include    <malloc.h>
#include    <string.h>
#include    "INCLUDE/project1.h"
short   datamemory(struct data *d)
{
    d->mask = (byte *)calloc( IMGSI*Z*IMGSI*Z,sizeof(byte) );
    if( d->mask == NULL ) return(0);
    d->f_est = (float *)calloc( IMGSI*Z*IMGSI*Z,sizeof(float) );
    if( d->f_est == NULL ) return(0);
    d->g_obs = (float *)calloc( ANGLES*BINS,sizeof(float) );
    if( d->g_obs == NULL ) return(0);
    d->g_est = (float *)calloc( ANGLES*BINS,sizeof(float) );
    if( d->g_est == NULL ) return(0);
    d->g_rat = (float *)calloc( ANGLES*BINS,sizeof(float) );
    if( d->g_rat == NULL ) return(0);
    d->normSubset = (float *)calloc(SUBSET*IMGSI*Z*IMGSI*Z,sizeof(float) );
    if( d->normSubset == NULL ) return(0);
    d->norm = (float *)calloc(BINS*ANGLES,sizeof(float) );
    if( d->norm == NULL ) return(0);
    return(1);
}

```

```

/*-----memory1.c-----*/

#include <malloc.h>
#include <string.h>
#include <stdlib.h>
#include "INCLUDE/project1.h"

short alloc_binmem(struct bintbl *bin)
{
    bin->bin1 = (ushort *)malloc( (size_t)(sizeof(ushort)*IMGSIZ*IMGSIZ) );
    if( bin->bin1 == NULL )
        return(0);
    bin->bin2 = (ushort *)malloc( (size_t)(sizeof(ushort)*IMGSIZ*IMGSIZ) );
    if( bin->bin2 == NULL )
        return(0);
    bin->bin3 = (ushort *)malloc( (size_t)(sizeof(ushort)*IMGSIZ*IMGSIZ) );
    if( bin->bin3 == NULL )
        return(0);
    bin->atnlen1 = (float *)malloc( (size_t)(sizeof(float)*IMGSIZ*IMGSIZ) );
    if( bin->atnlen1 == NULL )
        return(0);
    bin->atnlen2 = (float *)malloc( (size_t)(sizeof(float)*IMGSIZ*IMGSIZ) );
    if( bin->atnlen2 == NULL )
        return(0);
    bin->atnlen3 = (float *)malloc( (size_t)(sizeof(float)*IMGSIZ*IMGSIZ) );
    if( bin->atnlen3 == NULL )
        return(0);
    memset(bin->bin1,0,sizeof(ushort)*IMGSIZ*IMGSIZ);
    memset(bin->bin2,0,sizeof(ushort)*IMGSIZ*IMGSIZ);
    memset(bin->bin3,0,sizeof(ushort)*IMGSIZ*IMGSIZ);
    memset(bin->atnlen1,0,sizeof(float)*IMGSIZ*IMGSIZ);
    memset(bin->atnlen2,0,sizeof(float)*IMGSIZ*IMGSIZ);
    memset(bin->atnlen3,0,sizeof(float)*IMGSIZ*IMGSIZ);

    return(1);
}

```

```

void free_binmem(struct bintbl *bin)
{
    free( (void *)bin->bin1 );
    free( (void *)bin->bin2 );
    free( (void *)bin->bin3 );
    free( (void *)bin->atnlen1 );
    free( (void *)bin->atnlen2 );
    free( (void *)bin->atnlen3 );
}

/*-----memory1.c-----*/
#include <math.h>
#include "INCLUDE/project1.h"

setang ang[500];
float ax[5];

void set_angles( float max_angle )
{
    int i;
    float rotate;

    /* Rotate by 1/20 of one discrete angle */
    rotate = max_angle/((float)ANGLES*2.*10.);

    /* ----- Precompute sin, cos, tan ----- */
    for(i=0; i<ANGLES; i++) {
        ang[i].rad = max_angle * (float)i / ANGLES + rotate;
        ang[i].sin = sin(ang[i].rad);
        ang[i].cos = cos(ang[i].rad);
        ang[i].tan = tan(ang[i].rad);
    }

    ax[0] = 0;
    ax[1] = M_PI/2.;
}

```

```

    ax[2] = M_PI;
    ax[3] = 3.*M_PI/2.;
    ax[4] = 2.*M_PI;
}

/*-----lut.c-----*/
#include <math.h>
#include <string.h>
#include "INCLUDE/project1.h"

void lut( struct bintbl *bin, float *mask)

{
int   s;           /* indices for angle and bin, respectively */
int   i,j,l,r;    /* indices for pixel (i,j) */
int   k;          /* index for pixel along a ray */
int   p;          /* temporary index */
float x1,x2,y1,y2; /* starting and ending points of a ray */
float atten;      /* temporary buffer for attenuating length (atlen) */
float atlen;      /* attenuating length */
float length;     /* chord length */
float temp;       /* temporary variable */
struct raytbl ray; /* structure for Siddon's ray tracing method */
float  bb;
ushort b;

    COR.intercept=BINS/2.;
    COR.x=(float)COR.j+0.5;
    COR.y= (float)(IMGSIZ-COR.i)-0.5;
    ray.x=(ushort *)malloc( (size_t)(sizeof(ushort)*IMGSIZ*2) );
    memset(ray.x,0,sizeof(ushort)*2*IMGSIZ);
    ray.y=(ushort *)malloc( (size_t)(sizeof(ushort)*IMGSIZ*2) );
    memset(ray.y,0,sizeof(ushort)*2*IMGSIZ);
    ray.length=(float *)malloc( (size_t)(sizeof(float)*IMGSIZ*2) );
    memset(ray.length,0,sizeof(float)*2*IMGSIZ);

```

```

for(s=0; s<1; s++) {
  for (b=BINS-1; b>=BINS/2; b--){
    for(l=0; l<RAYS; l++) {
      r=(int) RAYS/2;

      if((RAYS-2*r)==0) bb=b+(float)(l-r+0.5)/(float)RAYS;
      else bb=b+(float)(l-r)/(float)RAYS;

      /* Find intersecting points for given angle and bin */
      intersect1( s, (float)(bb), &x1, &y1, &x2, &y2 );

      /* Skip the procedure if the ray is outside the image region */
      if( x1 < 0 || y1 < 0 || x2 < 0 || y2 < 0 ) continue;

      /* Compute Siddon's quantities */
      ray_trace( s, x1, y1, x2, y2, &ray );

      atten = 0;
      for(k=0; k<ray.size; k++) {

        j = *(ray.x+k);      /* pixel index j */
        i = *(ray.y+k);      /* pixel index i */
        length = *(ray.length+k);  /* chord length */

        /* Skip if pixel indices are out of image region */
        if( i >= IMGSIZ || i < 0 || j >= IMGSIZ || j < 0 ) continue;

        atnlen = exp(-atten)*length/(float)RAYS;

        /* ----- Fill in LUT ----- */
        p = i*IMGSIZ+j;
        if(( *(bin->bin1+p) == 0 )((ushort)*(bin->bin1+p) == b)) {
          *(bin->bin1 + p) = (ushort)b;    /* 1st bin (t1) */
          *(bin->atnlen1 + p) += atnlen;  /* 1st atnlen */
        }
      }
    }
  }
}

```

```

else if(( *(bin->bin2+p)==0)||((ushort)*(bin->bin2+p)==b)){
    *(bin->bin2 + p) = (ushort)b;    /* 2nd bin (t2) */
    *(bin->atnlen2 + p) += atnlen;    /* 2nd atnlen */
}
else if(( *(bin->bin3+p)==0)||((ushort)*(bin->bin3+p)==b)){
    *(bin->bin3 + p) = (ushort)b;    /* 3nd bin (t3) */
    *(bin->atnlen3 + p) += atnlen;    /* 3nd atnlen */
}
}
} //end of l
} //end of b
} //end of s

free( (void *)ray.x );
free( (void *)ray.y );
free( (void *)ray.length );

```

} //end of subroutine

/\*-----**intersect1.c**-----\*/

#include <stdio.h>

#include <math.h>

#include <string.h>

#include "INCLUDE/project1.h"

void intersect1( int i, float jj, float \*x1, float \*y1, float \*x2, float \*y2)

{

float theta;

float M, LL, j;

j = jj \* COR.ratio; //ratio = bin\_size/pixel\_size

LL = COR.intercept \* COR.ratio;

theta = ang[i].rad;

M = (float)IMGSIZ;

```

/* ----- 1st quadrant ----- */
if( theta >= ax[0] && theta < ax[1] ) {

    *y1 = M;
    *x1 = (*y1-COR.y)/ang[i].tan + COR.x -
        ((float)j-LL)/ang[i].sin;
    if( *x1 >= 0 && *x1 <= M )
        goto next1;

    *x1 = M;
    *y1 = ang[i].tan*(*x1-COR.x) + COR.y +
        ((float)j-LL)/ang[i].cos;
    if( *y1 >= 0 && *y1 <= M )
        goto next1;

    *x1 = *x2 = *y1 = *y2 = -1;

next1:

    *y2 = 0;
    *x2 = (*y2-COR.y)/ang[i].tan + COR.x -
        ((float)j-LL)/ang[i].sin;
    if( *x2 >= 0 && *x2 <= M )
        return;

    *x2 = 0;
    *y2 = ang[i].tan*(*x2-COR.x) + COR.y +
        ((float)j-LL)/ang[i].cos;
    if( *y2 >= 0 && *y2 <= M )
        return;

    *x1 = *x2 = *y1 = *y2 = -1;
    return;
}

```

```

/* ----- 2nd quadrant ----- */
else if( theta >= ax[1] && theta < ax[2] ) {
    *y1 = M;
    *x1 = (*y1-COR.y)/ang[i].tan + COR.x -
        ((float)j-LL)/ang[i].sin;
    if( *x1 >= 0 && *x1 <= M )
        goto next2;

    *x1 = 0;
    *y1 = ang[i].tan>(*x1-COR.x) + COR.y +
        ((float)j-LL)/ang[i].cos;
    if( *y1 >= 0 && *y1 <= M )
        goto next2;

    *x1 = *x2 = *y1 = *y2 = -1;

next2:
    *y2 = 0;
    *x2 = (*y2-COR.y)/ang[i].tan + COR.x -
        ((float)j-LL)/ang[i].sin;
    if( *x2 >= 0 && *x2 <= M )
        return;

    *x2 = M;
    *y2 = ang[i].tan>(*x2-COR.x) + COR.y +
        ((float)j-LL)/ang[i].cos;
    if( *y2 >= 0 && *y2 <= M )
        return;

    *x1 = *x2 = *y1 = *y2 = -1;
    return;
}

```

```

/* ----- 3rd quadrant ----- */
else if( theta >= ax[2] && theta < ax[3] ) {

    *y1 = 0;
    *x1 = (*y1-COR.y)/ang[i].tan + COR.x -
        ((float)j-LL)/ang[i].sin;
    if( *x1 >= 0 && *x1 <= M )
        goto next3;

    *x1 = 0;
    *y1 = ang[i].tan>(*x1-COR.x) + COR.y +
        ((float)j-LL)/ang[i].cos;
    if( *y1 >= 0 && *y1 <= M )
        goto next3;

    *x1 = *x2 = *y1 = *y2 = -1;

next3:

    *y2 = M;
    *x2 = (*y2-COR.y)/ang[i].tan + COR.x -
        ((float)j-LL)/ang[i].sin;
    if( *x2 >= 0 && *x2 <= M )
        return;

    *x2 = M;
    *y2 = ang[i].tan>(*x2-COR.x) + COR.y +
        ((float)j-LL)/ang[i].cos;
    if( *y2 >= 0 && *y2 <= M )
        return;

    *x1 = *x2 = *y1 = *y2 = -1;
    return;
}

```

```

/* ----- 4th quadrant ----- */
else if( theta >= ax[3] && theta < ax[4] ) {

    *y1 = 0;
    *x1 = (*y1-COR.y)/ang[i].tan + COR.x -
        ((float)j-LL)/ang[i].sin;
    if( *x1 >= 0 && *x1 <= M )
        goto next4;

    *x1 = M;
    *y1 = ang[i].tan*( *x1-COR.x ) + COR.y +
        ((float)j-LL)/ang[i].cos;
    if( *y1 >= 0 && *y1 <= M )
        goto next4;

    *x1 = *x2 = *y1 = *y2 = -1;

next4:

    *y2 = M;
    *x2 = (*y2-COR.y)/ang[i].tan + COR.x -
        ((float)j-LL)/ang[i].sin;
    if( *x2 >= 0 && *x2 <= M )
        return;

    *x2 = 0;
    *y2 = ang[i].tan*( *x2-COR.x ) + COR.y +
        ((float)j-LL)/ang[i].cos;
    if( *y2 >= 0 && *y2 <= M )
        return;

    *x1 = *x2 = *y1 = *y2 = -1;
    return;
}
}

```

```

/*-----raytrace.c-----*/

#include <stdio.h>
#include <string.h>
#include <math.h>
#include "INCLUDE/project1.h"

void ray_trace( int angle, float x1, float y1, float x2, float y2, struct raytbl *ray )
{
int Nx,Ny,X_Nx,Y_Ny;
int i,j,k,l;
int imin,imax;
int jmin,jmax;
int m,n;
float X1,X2,Y1,Y2;
float temp, p, q, theta;
float dX,dY,dX1,dY1;
float *Ax,*Ay;//Ax[IMGSIZ+2],Ay[IMGSIZ+2];
float *alpha;//alpha[2*IMGSIZ+4];

Ax = (float *)malloc( (IMGSIZ+2)*sizeof(float) );
if( Ax == NULL ) {printf("memory problem!!\n"); exit(1);}
Ay = (float *)malloc( (IMGSIZ+2)*sizeof(float) );
if( Ay == NULL ) {printf("memory problem!!\n"); exit(1);}
alpha= (float *)malloc( (2*IMGSIZ+4)*sizeof(float) );
if( alpha == NULL ) {printf("memory problem!!\n"); exit(1);}

Nx=IMGSIZ + 1; /* The following constans are used */
Ny=IMGSIZ + 1; /* for Siddon's ray tracing method. */
X_Nx=IMGSIZ ;
Y_Ny=IMGSIZ ;
theta = ang[angle].rad;
X1 = x1;
Y1 = y1;
X2 = x2;
Y2 = y2;

```

```

dX = X2 - X1;
dY = Y2 - Y1;
dX1 = 1./dX;
dY1 = 1./dY;

memset(alpha,0,sizeof(float)*(2*IMGSIZ+4));
memset(Ax,0,sizeof(float)*(IMGSIZ+2));
memset(Ay,0,sizeof(float)*(IMGSIZ+2));

if( theta > ax[0] && theta < ax[1] ) {

    imin = Nx - (int)(X_Nx-X2);
    imax = 1 + (int)X1;
    jmin = Ny - (int)(Y_Ny-Y2);
    jmax = 1 + (int)Y1;

    m = imax - imin + 1;
    temp = ((float)imax - X1)*dX1;

    for(i=1; i<=m; i++)
        Ax[i] = temp - (float)i*dX1;

    n = jmax - jmin + 1;
    temp = ((float)jmax - Y1)*dY1;

    for(j=1; j<=n; j++)
        Ay[j] = temp - (float)j*dY1;
}
else if( theta > ax[1] && theta < ax[2] ) {

    imin = Nx - (int)(X_Nx-X1);
    imax = 1 + (int)X2;
    jmin = Ny - (int)(Y_Ny-Y2);
    jmax = 1 + (int)Y1;

```

```

m = imax - imin + 1;
temp = ((float)(imin - 2) - X1)*dX1;

for(i=1; i<=m; i++)
    Ax[i] = temp + (float)i*dX1;

n = jmax - jmin + 1;
temp = ((float)jmax - Y1)*dY1;

for(j=1; j<=n; j++)
    Ay[j] = temp - (float)j*dY1;
}

else if( theta > ax[2] && theta < ax[3] ) {

    imin = Nx - (int)(X_Nx-X1);
    imax = 1 + (int)X2;
    jmin = Ny - (int)(Y_Ny-Y1);
    jmax = 1 + (int)Y2;

    m = imax - imin + 1;
    temp = ((float)(imin - 2) - X1)*dX1;

    for(i=1; i<=m; i++)
        Ax[i] = temp + (float)i*dX1;

    n = jmax - jmin + 1;
    temp = ((float)(jmin - 2) - Y1)*dY1;

    for(j=1; j<=n; j++)
        Ay[j] = temp + (float)j*dY1;
}

else if( theta > ax[3] && theta < ax[4] ) {

```

```

imin = Nx - (int)(X_Nx-X2);
imax = 1 + (int)X1;
jmin = Ny - (int)(Y_Ny-Y1);
jmax = 1 + (int)Y2;

m = imax - imin + 1;
temp = ((float)imax - X1)*dX1;

for(i=1; i<=m; i++)
    Ax[i] = temp - (float)i*dX1;

n = jmax - jmin + 1;
temp = ((float)(jmin - 2) - Y1)*dY1;

for(j=1; j<=n; j++)
    Ay[j] = temp + (float)j*dY1;
}

temp = sqrt(dX*dX + dY*dY);
l = merge(m, n, Ax, Ay, alpha);

if( alpha[l-1] != alpha[l] )
    n = l - 1;
else
    n = l - 2;

if( alpha[l] != alpha[l+1] )
    m = l;
else
    m = l + 1;

i = 0;
for(k=m; k<=n; k++) {
    p = temp*(alpha[k+1] - alpha[k]);
    if( p <= 0 )

```

```

        continue;
    q = 0.5*(alpha[k+1] + alpha[k]);
    //changed to a dynamic memory link, 07/07/98
    *(ray->length+i) = p;
    *(ray->x+i) = (int) (X1+q*dX);
    *(ray->y+i) = IMGSIZ-1 -(int)(Y1 + q*dY);
    i++;
}

ray->size = i;

free(Ax);free(Ay);free(alpha);
}

int merge(int m, int n, float *Ax, float *Ay, float *alpha)
{
int i,j,k,l;

i = j = 1;
k = 0;

while ( i<=m && j<=n ) {
    k++;
    if( *(Ax+i) < *(Ay+j) ) {
        *(alpha + k) = *(Ax + i);
        i++;
    }
    else {
        *(alpha + k) = *(Ay + j);
        j++;
    }
}

if(i <= m) {
    for(l=i; l<=m; l++) {

```

```

        k++;
        *(alpha + k) = *(Ax+l);
    }
}
else {
    for(l=j; l<=n; l++) {
        k++;
        *(alpha + k) = *(Ay+l);
    }
}
return(k);
}

/*-----fwdprj1OS.c-----*/
#include <math.h>
#include <string.h>
#include "INCLUDE/project1.h"

void fwdprj1OS(float *imgbuf, float *prjbuf, byte *mask, struct bintbl *bin, int a)
{
int i,j,p,s;
int t1,t2,t3;
float atnlen1,atnlen2,atnlen3;
float temp[ANGLES][BINS];
float *new;
unsigned short x1,x2,x3;
unsigned short y1,y2,y3;

new = (float *)calloc( IMGSIZ*IMGSIZ,sizeof(float) );
if( new == NULL )
{printf("memory problem!\n"); exit(1);}

memset(temp,0,sizeof(float)*ANGLES*BINS);

for (s=a; s<ANGLES; s=s+SUBSET) {

```

```

rotimg((float *)imgbuf,s,(float *)new,1,METHOD);

for(i=0; i<IMGSIZ/2; i++) {
    for(j=0; j<IMGSIZ; j++) {
        /* Skip outside the mask region */
        if( *(mask+IMGSIZ*i+j) == 0 )
            continue;

        /* Convert 3-D indices to 1-D index */
        p = i*IMGSIZ+j;

        /* Read data from LUT */
        t1 = (int)*(bin->bin1 + p);
        t2 = (int)*(bin->bin2 + p);
        t3 = (int)*(bin->bin3 + p);

        atnlen1 = *(bin->atnlen1 + p);
        atnlen2 = *(bin->atnlen2 + p);
        atnlen3 = *(bin->atnlen3 + p);

        /* Accumulate projection counts along the two rays */
        if(t1>0)
        {
            temp[s][t1] += *(new+IMGSIZ*i+j)*atnlen1;
            x1=floor(t1/BINS);
            y1=BINS-1-(t1-x1*BINS);
            temp[s][y1] += *(new+IMGSIZ*(IMGSIZ-1-i)+j)*atnlen1;
        }
        if(t2>0)
        {
            temp[s][t2] += *(new+IMGSIZ*i+j)*atnlen2;
            x2=floor(t2/BINS);
            y2=BINS-1-(t2-x2*BINS);
            temp[s][y2] += *(new+IMGSIZ*(IMGSIZ-1-i)+j)*atnlen2;
        }
    }
}

```

```

        if(t3>0)
        {
            temp[s][t3] += (*(new+IMGSIZ*i+j))*atnlen3;
            x3=floor(t3/BINS);
            y3=BINS-1-(t3-x3*BINS);
            temp[s][y3] += (*(new+IMGSIZ*(IMGSIZ-1-i)+j))*atnlen3;
        }

    }//end of j
} //end of i
} //end of s

for (s=a; s<ANGLES; s=s+SUBSET) {
    for (t3=0;t3<BINS;t3++)
        *(prjbuf+BINS*s+t3)=temp[s][t3];
}
free(new);
}

/*-----rotimg.c-----*/
#include <math.h>
#include <stdio.h>
#include <string.h>
#include "INCLUDE/project1.h"
#include <stdlib.h>

void rotimg(float *imgbuf,int angle,float *new,int t,int interpolation)
{
    int xs,ys,i,j,m,n,k,p1,ii,jj;
    float x,y,p,q,c,s,d,h1,h2,max;
    double r;
    max=0;
    xs=COR.j;
    ys=COR.i-1;

```

```
memset(new,0,sizeof(float)*IMGSIZ*IMGSIZ);
```

```
if (angle!=0){ // if angle !=0, we need to rotate images for each slice along x-y plane.
```

```
    if (t==1) r=M_PI/2+ang[angle].rad; // t==1 means that roate images clockwise.
```

```
    else r=M_PI/2-ang[angle].rad; // t== -1 means that rotate images anti-clockwise.
```

```
    c=cos(r);s=sin(r);
```

```
if (interpolation==1){/*  bilinear interpolation  */
```

```
    for (i=0;i<IMGSIZ;i++){//y
```

```
        for (j=0;j<IMGSIZ;j++){//x
```

```
            /* + and - control the direction of rotation */
```

```
            x=(j-xs)*s-(i-ys)*c;
```

```
            y=(j-xs)*c+(i-ys)*s;
```

```
            d=0.0;
```

```
            if (y>=0) m=(y);
```

```
            else m=(y-1);
```

```
            if (x>=0) n=(x);
```

```
            else n=(x-1);
```

```
            q=y-m;p=x-n;
```

```
            /*  bilinear interpolation  */
```

```
            if (m>=-ys && m<ys && n>=-xs && n<xs)
```

```
                d=(1-q)*((1-p)* (*(imgbuf+(m+ys)*IMGSIZ+n+xs))+p* (*(imgbuf+(m+ys)*IMGSIZ+n+xs+1)))+q* ((1-p)*
```

```
                (*(imgbuf+(m+ys+1)*IMGSIZ+n+xs))+p* (*(imgbuf+(m+ys+1)*IMGSIZ+n+xs+1)));
```

```
            else d=0;
```

```
            *(new+i*IMGSIZ+j)=d;
```

```
        }
```

```
    }
```

```

} //end of if
else { /* bicubic interpolation */

    for (i=0;i<IMGSIZ;i++){ //y
        for (j=0;j<IMGSIZ;j++){ //x

            /* + and - control the direction of rotation */
            x=(j-xs)*s-(i-ys)*c;
            y=(j-xs)*c+(i-ys)*s;
            d=0.0;
            if (y>0) m=(y);
            else m=(y-1);
            if (x>0) n=(x);
            else n=(x-1);

            q=y-m;p=x-n;

            /* bicubic interpolation */
            if (m>=-ys+2 && m<ys-2 && n>=-xs+2 && n<xs-2){
                for (ii=-1;ii<=2;ii++){
                    for (jj=-1;jj<=2;jj++){

                        if (fabs(ii-q)>=0 && fabs(ii-q)<1) h1=1-2*(fabs(ii-q)*fabs(ii-q))+
                            (fabs(ii-q)*fabs(ii-q)*fabs(ii-q));
                        else if (fabs(ii-q)>=1 && fabs(ii-q)<2) h1=4-8*fabs(ii-q)+5*(fabs(ii-q)*fabs(ii-q))-
                            (fabs(ii-q)*fabs(ii-q)*fabs(ii-q));
                        else h1=0;

                        if (fabs(p-jj)>=0 && fabs(p-jj)<1) h2=1-2*(fabs(p-jj)*fabs(p-jj))+
                            (fabs(p-jj)*fabs(p-jj)*fabs(p-jj));
                        else if (fabs(p-jj)>=1 && fabs(p-jj)<2) h2=4-8*fabs(p-jj)+5*(fabs(p-jj)*fabs(p-jj))-
                            (fabs(p-jj)*fabs(p-jj)*fabs(p-jj));
                        else h2=0;

                        d+=h1*h2*(imgbuf+(m+ys+ii)*IMGSIZ+n+xs+jj);

                    } //end of ii
                } //end of jj
            }
        }
    }
}
else d=0;

```

```

        *(new+i*IMGSIZ+j)=d;

    }
}

} //end of else
} //end of angle!=0

// if angle==0, we do not rotate image. We just copy original images to new.
else memcpy(new, imgbuf, sizeof(float)*IMGSIZ*IMGSIZ);

}

/*-----makesart-----*/
CC=gcc -g -O

sart: sart.o mipltool1 tool1 INCLUDE/project1.h
    gcc -g -O -o sart sart.o mipltool1 tool1 -lm
mipltool1:mipltool1(intersect1.o) mipltool1(memory1.o) mipltool1(lut.o) mipltool1(raytrace.o) mipltool1(setangles.o)
mipltool1(convolve.o) mipltool1(fwdprj1OS.o) mipltool1(datamemory.o) mipltool1(rotimg.o)
    @echo "updating the mipltool1 library"
    ranlib mipltool1

tool1:tool1(fileio.o) tool1(rng.o)
    @echo "updtng the tool1s library"
    ranlib tool1

```

## BIBLIOGRAPHY

Ahn S, Fessler JA. Globally convergent image reconstruction for emission tomography using relaxed ordered subsets algorithms. *IEEE Trans. Med. Imaging.* 2003; 22(5):616-619.

Allaire E, Guettier C, Bruneval P, Plissonnier D, Michel JB. Cell-free arterial grafts: morphologic characteristics of aortic isografts, allografts, and xenografts in rats. *J Vasc Surg* 1994; 19(3):446-456.

Anderson AH, Kak AC. Simultaneous algebraic reconstruction technique (SART): A superior implementation of the ART algorithm. *Ultrason Imaging.* 1984; 6(1):81-94.

Anderson JM, Ziats NP. Human blood protein and cellular interactions in the healing responses of vascular prosthesis. *J Vasc Surg* 1991; 13(5):750-751.

Auger FA, Berthod F, Moulin V, Pouliot R, Germain L. Tissue-engineered skin substitutes: from in vitro constructs to in vivo applications. *Biotechnol Appl Biochem* 2004; 39(3):263-275.

Bartrum RJ, Crow HC. Transillumination light scanning to diagnose breast cancer: a feasibility study. *AJR Am J Roentgenol* 1984; 142(2):409-414.

Bellemann ME, Baier T, Seitz B, Walther HG. Development of a laser-optical tomograph for demonstration of CT imaging without ionizing radiation. *Biomed Tech* 2002; 47 (1): 467-469.

Bergamini TM, Bandyk DF, Govostis D, Kaebnick HW, Towne JB. Infection of vascular prostheses caused by bacterial biofilms. *J Vasc Surg* 1988; 7(1):21-30.

Bergan JJ, Veith FJ, Bernhard VM, Yao JS, Flinn WR, Gupta SK, Scher LA, Samson RH, Towne JB. Randomization of autogenous vein and polytetrafluorethylene grafts in femoral-distal reconstruction. *Surgery* 1982; 92(6):921-930.

Bushberg J, Seibert J, Leidholdt E, Boone J. *The Essential Physics of Medical Imaging* 2nd Edition. 2002. Philadelphia, PA, Lippincott Williams and Wilkins. 933 Pages.

Charlesworth PM, Brewster DC, Darling RC, Robison JG, Hallet JW. The fate of polytetrafluoroethylene grafts in lower limb bypass surgery: a six year follow-up. *Br J Surg* 1985; 72(11):896-899.

Chen K, Perelman LT, Zhang Q, Dasari RR, Feld MS. Optical computed tomography in a turbid medium using early arriving photons. *J Biomed Opt* 2000; 5(2):144-154.

Cho ZH, Jones JP, Singh M. *Foundations of Medical Imaging*. 1993. New York, John Wiley & Sons. 600 Pages.

Colak SB, Papaioannou DG, tHooft GW, vanderMark MB, Schomberg H, Paasschens JCJ, Messlissen JBM, vanAsten NAAJ. Tomographic image reconstruction from optical projection in light-diffusing media. *Appl Opt* 1997; 36(1):180-213.

Crawford CR. System for reprojecting images using transform techniques. 1986, US Patent 4,616,318. Filed 1983-6-7. Elscint.

Crawford CR, Colsher JG, Pelc NJ, Lonn AHR. High speed reprojection and its applications. *SPIE. Med. Im. II: Im. Formation, Detection, Processing, and Interpretation*, 1988; 914:311-318.

Cutler M. Transillumination as an aid in the diagnosis of breast lesions. *Surg Gynecol Obstet* 1929; 48:721-728.

Dardik H, Miller N, Dardik A, Ibrahim I, Sussman B, Berry SM, Wologiger F, Kahn M, Dardik, I. A decade of experience with the glutaraldehyde-tanned human umbilical cord vein graft for revascularization of the lower limb. *J Vasc Surg* 1988; 7(2):336-346.

Di Bella EVR, Barclay AB, Eisner RL, Schafer RW. A comparison of rotation-based methods for iterative reconstruction algorithms. *IEEE Trans Nucl Trans* 1996; 43(6):3370-3376.

Doran SJ, Koerkamp KK, Bero MA, Jenneson P, Morton EJ, Gilboy WB. A CCD-based optical CT scanner for high-resolution 3D imaging of radiation dose distributions: Equipment specifications, optical simulations and preliminary results. *Phys Med Biol* 2001; 46(12):3191-3213.

Drexler B, Davis JL, Schofield G. Diaphanography in the diagnosis of breast cancer. *Radiology* 1985; 157(1):41-44.

Gayen SK, Zevallos ME, Alrubaiee M, Evans JM, Alfano RR. Two-dimensional near-infrared transillumination imaging of biomedical media with a chromium-doped forsterite laser. *Appl Opt* 1998; 37(22):5327-5336.

Gladish JC, Yao G, Heureux NL, Haidekker MA. Optical transillumination tomography for imaging of tissue-engineered tissue blood vessels. *ABME* 2005; 33(3):323-327.

Gordon R, Bender R, Herman GT. Algebraic reconstruction techniques (ART) for three-dimensional electron microscopy and x-ray photography. *J Theor Biol* 1970; 29(3):471-481.

Gore JC, Ranade M, Maryanski MJ, Schulz RJ. Radiation dose distributions in three dimensions from tomographic optical density scanning of polymer gels. I. Development of an optical scanner. *Phys Med Biol* 1996; 41(12):2695-2704.

Greisler HP. Interactions at the blood/material interfact. *Ann Vasc Surg* 1990; 4(1):98-103.

Griffith M, Hakim M, Shimmura S, Watsky MA, Li F, Carlsson D, Doillon CJ, Nakamura M, Suuronen E, Shinozaki N, Nakata K, Sheardown H. Artificial human corneas: scaffolds for transplantation and host regeneration. *Cornea* 2002; 21(7):S54-S61.

Guidoin R, Noel HP, Marois M, Martin L, Laroche F, Beland L, Cote R, Gosselin C, Descotes J, Chiquier E, Blais P. Another look at the Sparks-Mandril arterial graft precursor for vascular repair. Pathology by scanning electron microscopy. *Biomater Med Devices Artif Organs* 1980; 8(2):145-167.

Haidekker MA. Optical Transillumination Tomography with tolerance against refraction mismatch. *Comput Programs Biomed* 2005; 80(3): 225-235.

Hebden JC, Arridge SR, Delpy DT. Optical imaging in medicine: I. Experimental techniques. *Phys Med Biol* 1997; 42(5):825-840.

Hsiao IT, Rangarajan A, Gindi GR. A new convergent MAP reconstruction algorithm for emission tomography using ordered subsets and separable surrogates. *Proceedings of IEEE International Symposium on Biomedical Imaging*. 2002; 409-412.

Huang D, Swanson EA, Lin CP, Schuman JS, Stinson WG, Chang W, Hee MR, Flotte T, Gregory K, Puliafito CA, Fujimoto JG. Optical coherence tomography. *Science* 1991; 254(5035):1178-1181.

- Hudson H, Larkin R. Accelerated image reconstruction using ordered subsets of projection data. *IEEE Trans Med Imaging* 1994; 13(4):601-609.
- Islam KTS, Dempsey JF, Ranade MK, Maryanski MJ, Low DA. Initial evaluation of commercial optical CT-based 3D gel dosimeter. *Med Phys* 2003; 30(8):2159-2168.
- Internet Health Library: Arteriosclerosis, 2006.  
<http://www.internethealthlibrary.com/Health-problems/Arteriosclerosis.htm>
- Kelly BG, Jordan KJ, Battista JJ. Optical CT reconstruction of 3D dose distributions using the ferrous-benzoic-xyleneol (FBX) gel dosimeter. *Med Phys* 1998; 25(9):1741-1750.
- Lee SJ. MIPL Reconstruction Software Package: Background Description and Source Listing. Depts. of Radiology and Electrical Engineering, State University of New York at Stony Brook, 1996; Technical Report MIPL-96-2.
- L'Heureux N, Germain L, Labbe R, Auger FA. In vitro construction of a human blood vessel from cultured vascular cells: a morphologic study. *J Vasc Surg* 1993; 17(3):499-509.
- L'Heureux N, Paquet S, Labbe R, Germain L, Auger FA. A completely biological tissue-engineered human blood vessel. *FASEB J* 1998; 12(1):47-56.
- L'Heureux N, Stoclet JC, Auger FA, Lagaud GJ, Germain L, Andriantsitohaina R. A human tissue-engineered vascular media: a new model for pharmacological studies of contractile responses. *FASEB* 2001; 15(2):515-524.
- Mannick A, Whittemore D, Couch N. *Vascular surgery: A comprehensive review*. 1986. New York, Grune & Stratton. 1245 Pages.
- Marshall V, Williams DC, Smith KD. Diaphanography as a means of detecting breast cancer. *Radiology* 1984; 150(2):339-343.
- Maryanski MJ, Zastavker YZ, Gore JC. Radiation dose distributions in three dimensions from tomographic optical density scanning of polymer gels. II. Optical properties of the BANG polymer gel. *Phys Med Biol* 1996; 41(12):2705-2717.
- Matej S, Fessler JA, Kazantsev IG. Iterative tomographic image reconstruction using Fourier-based forward and back-projectors. *IEEE Trans Med Imag* 2004; 23(4):401-412.

Mertens RA, O'Hara PJ, Hertzner NR, Krajewski LP, Beven EG. Surgical management of infrainguinal arterial prosthetic graft infections: review of a thirty-five-year experience. *J Vasc Surg* 1995; 21(5):782-790.

Neuenschwander S, Hoerstrup SP. Heat valve tissue engineering. *Transpl Immunol* 2004; 12(3-4):359-365.

Oldham M, Siewerdsen JH, Shetty A, Jaffray DA. High resolution gel-dosimetry by optical-CT and MR scanning. *Med Phys* 2001; 28(7):1436-1445.

Oldham M, Siewerdsen JH, Kumar S, Wong J, Jaffray DA. Optical-CT gel-dosimetry I. Basic investigations. *Med Phys* 2003; 30(4):623-634.

Oldham M, Kim L. Optical-CT gel-dosimetry II. Optical artifacts and geometrical distortion. *Med Phys* 2004; 31(5):1093-1104.

Oldham M, Sakhalkar H, Oliver T, Wang YM, Kirpatrick J, Cao Y, Badea C, Johnson GA, Dewhurst M. Three-dimensional imaging of xenograft tumors using optical computed and emission tomography. *Med Phys* 2006; 33(9):3193-3202.

Oppenheim AV, Schafer RW. *Discrete-Time Signal Processing*. 1989. Prentice Hall. 879 Pages.

Parsson H, Jundzill W, Jonung T, Thorne J, Norgren L. The adhesion of labeled neutrophils on synthetic vascular grafts. An experimental porcine study. *Eur J Vasc Surg* 1993; 7(3):257-262.

Roberts PN, Hopkinson BR. The Sparks mandril in femoropopliteal bypass. *Br Med J* 1977; 2(6096):1190-1191.

Rosenfeld A, Kak AC. *Digital Picture Processing*, volume 1. 1982. New York, Academic Press. 435 Pages.

Sapsford RN, Oakley GD, Talbot S. Early and late patency of expanded polytetrafluoroethylene vascular grafts in aorta-coronary bypass. *J Thorac Cardiovasc Surg* 1981; 81(6):860-864.

Siddon R. Fast calculation of the exact radiological path length for a three-dimensional CT array. *Med Phys* 1985; 12(2):252-255.

- Stearns CW, Chesler DA, Brownell GL. Three-dimensional image reconstruction in the Fourier domain. *IEEE Trans Nuc Sci* 1987; 34(1):374-378.
- Stearns CW, Chesler DA, Brownell GL. Accelerated image reconstruction for a cylindrical positron tomograph using Fourier domain methods. *IEEE Trans Nuc Sci* 1990; 37(2):773-777.
- Suh H, Han DW, Park JC, Lee DH, Lee WS, Han CD. A bone replaceable artificial bone substitute: osteoinduction by combining with bone inducing agent. *Artificial Organs* 2001; 25(6): 459-466.
- Van de Pavoordt HD, Eikelboom BC, De Geest R, Vermeulen FE. Results of prosthetic grafts in femoro-crural bypass operations as compared to autogenous saphenous vein grafts. *Neth J Surg* 1986; 38(6):177-179.
- Wang G, Jiang M. Ordered-subset simultaneous algebraic reconstruction techniques (OS-SART). *Journal of X-Ray Science and Technology* 2004; 12(3):169-177.
- Weinberg CB, Bell E. A blood vessel model constructed from collagen and cultured vascular cells. *Science* 1986; 231(4736):397-400.
- Wolodzko JG, Marsden C, Appleby A. CCD imaging for optical tomography of gel radiation dosimeters. *Med Phys* 1999; 26(11):2508-2513.
- Yeager RA, Hobson RW, Jamil Z, Lynch TG, Lee BC, Jain K. Differential patency and limb salvage for polytetrafluoroethylene and autoenous saphenous vein in severe lower extremity ischemia. *Surgery* 1982; 91(1):99-103.
- Yuasa T, Tanosaki S, Tagaki M, Sasaki Y, Taniguchi H, Devaraj B, Akatsuka T. Transillumination optical sensing for biomedicine and diagnosis: feasibility of early diagnosis for rheumatoid arthritis. *Anal Sci* 2001; 17(4):515-518.